



**HAL**  
open science

# Electrical contact material arc erosion : experiments and modeling towards the design of an AgCdO substitute

Frédéric Pons

► **To cite this version:**

Frédéric Pons. Electrical contact material arc erosion : experiments and modeling towards the design of an AgCdO substitute. Other. Université Paul Verlaine - Metz, 2010. English. NNT : 2010METZ039S . tel-01750549

**HAL Id: tel-01750549**

**<https://hal.univ-lorraine.fr/tel-01750549>**

Submitted on 29 Mar 2018

**HAL** is a multi-disciplinary open access archive for the deposit and dissemination of scientific research documents, whether they are published or not. The documents may come from teaching and research institutions in France or abroad, or from public or private research centers.

L'archive ouverte pluridisciplinaire **HAL**, est destinée au dépôt et à la diffusion de documents scientifiques de niveau recherche, publiés ou non, émanant des établissements d'enseignement et de recherche français ou étrangers, des laboratoires publics ou privés.



**Erosion suite à l'impact d'un arc électrique:  
Modélisation & Campagnes expérimentales en vue du  
développement d'un matériau de substitution à l'alliage  
AgCdO**

**THESE**

présentée et soutenue publiquement le 07 mai 2010

pour l'obtention du grade de

**Docteur de l'Université Paul Verlaine de Metz**

**Spécialité : Sciences des Matériaux**

par

**Frédéric PONS**

**Composition du jury**

<i>Rapporteurs :</i>	Prof. Nouredine BEN JEMAA	Université de Rennes, France
	Prof. John W. MCBRIDE	Université de Southampton, UK
<i>Examineurs :</i>	Prof. Abdallah OUGAZZADEN	Georgia Institute of Technology, USA
	Dr. Jean-Marc RAULOT	Université de Metz, France
	Dr. Idriss ILALI	Université de Rabat, Maroc
<i>Directeur :</i>	Prof. Mohammed CHERKAOUI	Georgia Institute of Technology, USA

*To my parents, Nicole and Henri Pons*

*To my brother, Xavier Pons*

*To my grandfather, Claude Hermelin*

*Thanks for all your love and support through the years*

## ACKNOWLEDGEMENTS

First and foremost, I would like to thank my advisor, Prof. Mohammed Cherkaoui. He has given me an outstanding chance to pursue my education and have always been a great source of motivation and inspiration. I would like to express my deepest gratitude for his guidance and for his passion for research, and science in general, which he has kindly shared with me.

Second, I would like to thank Adeline Aubouin and Idriss Ilali for the numerous discussions we have had over the past years. Their advice, support and trust have undoubtedly added to the quality of this research and to my personal experience.

This thesis has been the chance for me to initiate a superb collaboration with Dr. Jean Marc Raulot who has kindly accepted to contribute to this research by performing ab initio calculations and by sharing his experience, knowledge and passion with me.

I express my deepest gratitude to Prof. John W. McBride and Prof. Nouredine Ben Jemaa who have kindly accepted to review my dissertation and to be part of this thesis committee. I perceive their presence as a great honor.

Merci to Prof. Abdallah Ougazzaden, Alain Boyer and Dr. Yves Berthelot for their help, their support and their precious advice over the past years.

I would also like to thank Serge Dominiak and Jean Sébastien Lecomte for their help and support during experiments, Mickaël Febvre and Emmanuel Paris for their help and support with white light interferometry measurements, Jean Jacques Michel for his

help and support while coding, and Jeffrey A. Donnell who helped me to improve the quality of my dissertation.

I would like to say “Merci” to Glenda Johnson, Florence Stoia and Josyane Roschitz for all their help, support and advice throughout all the administrative procedures.

My experience in graduate school would not have been so pleasant without my colleagues and friends at Georgia Tech Atlanta, at Paul Verlaine University, and at Georgia Tech Lorraine: Audric Saillard, Mohamed & Hager Abid, Vinod Ravindran, Alexandre & Sandrine Locquet, Laurent & Fanny Capolungo, K, Simon, Tarik, John & etc..

Finally, I would like to thank my parents Nicole and Henri Pons, and my brother Xavier Pons who have been there to support me and to encourage me to perform the best that I could. I hope one day to merit the sacrifices they have made for me. This thesis is dedicated to them.

# TABLE OF CONTENTS

ACKNOWLEDGEMENTS .....	iii
LIST OF TABLES .....	viii
LIST OF FIGURES .....	ix
SUMMARY .....	xiv
CHAPTER 1 .....	1
INTRODUCTION .....	1
1.1.    Arc erosion: breaking arc and material transfer.....	2
1.1.1.    Metallic phase .....	4
1.1.2.    Gaseous phase .....	6
1.2.    Silver Metal Oxide based contact materials.....	8
1.2.1.    AgCdO issue .....	8
1.2.2.    On the way to AgCdO substitution.....	10
1.3.    Methodology & outline.....	11
CHAPTER 2 .....	15
AgCdO ARC EROSION BEHAVIOR.....	15
2.1.    Arc erosion experiments .....	16
2.1.1.    Sample Definition .....	17
2.1.2.    Test Condition and Testing Procedure.....	18
2.1.3.    Experimental Set Up.....	19
2.1.4.    Experimental apparatus .....	20
2.2.    AgCdO Surface Dynamics.....	20

2.2.1.	Experimental results.....	20
2.2.2.	Discussion.....	30
2.3.	AgCdO Layer Dynamics.....	34
2.3.1.	Experimental results.....	34
2.3.2.	Discussion.....	41
CHAPTER 3	.....	43
AgSnO <sub>2</sub> ARC EROSION BEHAVIOR	.....	43
3.1.	AgSnO <sub>2</sub> Surface Dynamics.....	44
3.1.1.	Experimental results.....	44
3.1.2.	Discussion.....	51
3.2.	AgSnO <sub>2</sub> Layer Dynamics.....	52
3.2.1.	Experimental results.....	53
3.2.2.	Discussion.....	56
3.3.	Conclusion and comparison with AgCdO .....	57
CHAPTER 4	.....	61
COMPLETE MACROSCOPIC ARC EROSION MODEL AND EXPERIMENTAL VALIDATION.....	.....	61
4.1.	Arc erosion model architecture.....	63
4.1.1.	Arc Energy Transport Model .....	65
4.1.2.	Thermal Model.....	67
4.1.3.	Magneto-hydrodynamic Model .....	79
4.2.	Arc erosion experiments .....	90
4.2.1.	Sample Definition .....	91

4.2.2.	Test Condition and Testing Procedure.....	91
4.2.3.	White Light Interferometry.....	92
4.2.4.	Comparison between model and experimental results.....	94
4.3.	Conclusion .....	96
CHAPTER 5 .....		97
MODELING OF THE CONTACT MATERIAL PROPERTIES & COMPOSITION INFLUENCES ON THE ELECTRICAL ARC EROSION PHENOMENON.....		97
5.1.	Contact material properties influence .....	98
5.1.1.	Force contributions .....	98
5.1.2.	Ab initio .....	100
5.1.3.	Contact material properties study .....	106
5.2.	Tin oxide composition influence .....	109
5.2.1.	Methodology.....	110
5.2.2.	Results.....	111
5.3.	Conclusion .....	112
CHAPTER 6 .....		114
CONCLUSION.....		114
REFERENCES .....		119



## LIST OF TABLES

Table 2.2-1: Chemical composition of the different zones relative to Figure 2.2-2.....	22
Table 2.2-2: Chemical composition of the different zones relative to Figure 2.2-4 & Figure 2.2-5.....	24
Table 2.2-3: Chemical composition of the different zones relative to Figure 2.2-6 & Figure 2.2-7.....	26
Table 2.2-4: Chemical composition of the different zones relative to Figure 2.2-8.....	28
Table 2.2-5: Chemical composition of the different zones relative to Figure 2.2-9.....	30
Table 2.3-1: Chemical composition of the different zones relative to Figure 2.3-3.....	37
Table 3.1-1: Chemical composition of the different zones relative to Figure 3.1-2 & Figure 3.1-3.....	46
Table 3.1-2: Chemical composition of the different zones relative to Figure 3.1-4.....	48
Table 3.1-3: Chemical composition of the different zones relative to Figure 3.1-5.....	49
Table 3.1-4: Chemical composition of the different zones relative to Figure 3.1-6.....	50
Table 3.1-5: Chemical composition of the different zones relative to Figure 3.1-7.....	51
Table 3.3-1: Thermal properties of the major constituents in AgCdO and AgSnO <sub>2</sub> .....	59
Table 5.1-1: Evolution of the lattice parameter (no rescale and rescale with the static data), the density and the thermal expansion coefficient of silver with temperature .....	104

## LIST OF FIGURES

Figure 1.1-1: Schematic representation of a static contact and of a molten bridge formation.....	3
Figure 1.1-2: Schematic diagram of PSD model: Metallic phase.....	5
Figure 1.1-3: Schematic diagram of PSD model: Gaseous phase .....	6
Figure 1.3-1: Schematic representation of the research action plan .....	12
Figure 2.1-1: Pictures of the static and the moving contacts used in this experiment .....	17
Figure 2.1-2: Cut of the moving electrode.....	17
Figure 2.1-3: Experimental set up.....	19
Figure 2.1-4: Experimental system.....	19
Figure 2.2-1: EDS mapping of one part of the crater after one electrical arc (x800) - Anode.....	21
Figure 2.2-2: SEM picture of a characteristic part of the crater after one electrical arc - Anode.....	21
Figure 2.2-3: Chemical composition spectrum relative to zone 1 (Figure 2.2-2).....	22
Figure 2.2-4: SEM picture of the crater after two electrical arcs – Anode.....	23
Figure 2.2-5: Close-up of the blue frame (Figure 2.2-4) – Anode.....	24
Figure 2.2-6: SEM picture of the impacted area after three electrical arcs – Anode.....	25
Figure 2.2-7: Close-up of the blue frame (Figure 2.2-6) - Anode .....	27
Figure 2.2-8: SEM picture of the impacted area after ten electrical arcs – Anode.....	28
Figure 2.2-9: SEM picture of the impacted area after one hundred electrical arcs – Anode .....	29

Figure 2.2-10: Evolution of the AgCdO contact resistance with the number of arc (Data shown is the average of 5 sets of experiments).....	32
Figure 2.2-11: SEM picture of a cavity full of granules - Anode.....	33
Figure 2.3-1: Binocular view of a section of the moving electrode before arcing (25x)..	35
Figure 2.3-2: Section of the anode after one electrical arc (25x).....	35
Figure 2.3-3: SEM picture of the section of the anode after one electrical arc .....	36
Figure 2.3-4: Chemical composition spectrum relative to zone 7 (Figure 2.3-3).....	37
Figure 2.3-5: Close-up of the cavity enclosing zone 1 (Figure 2.3-3).....	38
Figure 2.3-6: Impacted surface layer after two electrical arcs (25x) .....	39
Figure 2.3-7: Impacted surface layer after three electrical arcs (25x) .....	39
Figure 2.3-8: Impacted surface layer after ten electrical arcs (25x) .....	40
Figure 2.3-9: Impacted surface layer after one hundred electrical arcs (25x) .....	40
Figure 3.1-1: EDS mapping of the crater after one electrical arc (x80) – Anode.....	45
Figure 3.1-2: Close-up of the red frame (Figure 3.1-1) (x200) – Anode.....	45
Figure 3.1-3: Close-up of the red frame (Figure 3.1-2) (x1000) – Anode.....	46
Figure 3.1-4: SEM picture of the impacted area after two electrical arcs (x200) – Anode .....	47
Figure 3.1-5: SEM picture of the impacted area after three electrical arcs (x200) – Anode .....	48
Figure 3.1-6: SEM picture of the impacted area after ten electrical arcs (x200) – Anode	49
Figure 3.1-7: SEM picture of the impacted area after one hundred electrical arcs (x400) – Anode.....	50

Figure 3.1-8: Evolution of the $\text{AgSnO}_2$ contact resistance with the number of arc (Data shown is the average of 5 sets of experiments).....	52
Figure 3.2-1: Grading of $\text{AgSnO}_2$ 88/12.....	53
Figure 3.2-2: Section of the anode after one electrical arc (x200).....	53
Figure 3.2-3: Impacted surface layer after two electrical arcs (x100) .....	54
Figure 3.2-4: Impacted surface layer after three electrical arcs (x200) .....	54
Figure 3.2-5: Impacted surface layer after ten electrical arcs (x500) .....	55
Figure 3.2-6: Impacted surface layer after one hundred electrical arcs (x500) .....	55
Figure 3.3-1: Evolution of the $\text{AgCdO}$ and $\text{AgSnO}_2$ contact resistances with the number of arc .....	58
Figure 4.1-1: Diagram of the models outputs and their coupling .....	64
Figure 4.1-2: Power dissipation through plasma region .....	65
Figure 4.1-3: Arc power output for $I=9\text{A}$ .....	67
Figure 4.1-4: Meshing scheme.....	68
Figure 4.1-5: Heat transfer scheme for interior nodes .....	69
Figure 4.1-6: Heat transfer scheme for the impacted element .....	71
Figure 4.1-7: Heat transfer scheme for bottom layer nodes.....	72
Figure 4.1-8: Heat transfer scheme for top layer nodes.....	73
Figure 4.1-9: Heat transfer scheme for left side nodes .....	73
Figure 4.1-10: Heat transfer scheme for right side nodes .....	74
Figure 4.1-11: Heat transfer scheme for the first element .....	75
Figure 4.1-12: Heat transfer scheme for the last element .....	76

Figure 4.1-13: Flowchart describing the procedure to get the temperature from the thermal state where $L_m$ & $L_v$ are respectively the latent heat of fusion and vaporization and $c$ the specific heat. ....	77
Figure 4.1-14: Temperature distribution at the arc extinction ( $I = 9$ A, $V = 64$ VDC, $S = 1$ m/s) .....	78
Figure 4.1-15: Scheme of the molten metal jet.....	79
Figure 4.1-16: Differential element of the molten metal jet .....	82
Figure 4.1-17: Cylindrical molten metal jet with axial disturbance .....	88
Figure 4.2-1: Pictures of the static and the moving contacts used in this experiment.....	91
Figure 4.2-2: WLI picture of an arc impact after one breaking operation (600 A, 28 VDC) .....	92
Figure 4.2-3: 3D view of Figure 4.2-2.....	93
Figure 4.2-4: High current experimental data and model results of AgCdO arc erosion .	94
Figure 4.2-5: Low current experimental data [44] and model results of AgCdO arc erosion.....	95
Figure 5.1-1: Forces contribution on Ag arc erosion process .....	99
Figure 5.1-2: Supercell of FCC Ag pure compound.....	100
Figure 5.1-3: Pressure evolution with the lattice parameter and the temperature. The points represent the atomic positions during a few steps of the simulation.....	102
Figure 5.1-4: Variation of the external pressure with the number of dynamic steps (black line) and the average calculated with the last 200 steps (red dashed line) where the temperature is fixed and the lattice parameter is fixed .....	102

Figure 5.1-5: Variation of the pressure with the lattice parameter when the temperature is equal to 600K (points) and data fitting with a polynomial form .....	103
Figure 5.1-6: Variation of the Ag density with temperature.....	104
Figure 5.1-7: Variation of the Ag linear thermal expansion coefficient with temperature .....	105
Figure 5.1-8: Arc erosion model results for a low and a high surface tension coefficient of Ag.....	106
Figure 5.1-9: Arc erosion model results for a low and a high density of Ag.....	107
Figure 5.1-10: Arc erosion model results for a low and a high thermal expansion coefficient of Ag .....	108
Figure 5.1-11: Contact material properties influence on Ag arc erosion process.....	109
Figure 5.2-1: Schematic representation of the AgSnO <sub>2</sub> matrix for a tin oxide composition of 9 % (267 atoms).....	110
Figure 5.2-2: Schematic representation of the AgSnO <sub>2</sub> matrix for a tin oxide composition of 22 % (291 atoms).....	111
Figure 5.2-3: Relative variations of the AgSnO <sub>2</sub> density with respect to its value for pure Ag for two different tin oxide compositions (9 & 22 %) and for three temperatures (800, 1000, & 1200 K) .....	112

## SUMMARY

AgCdO is one of the most widely used contact materials in the world because of its outstanding performance. Nevertheless, due to environmental considerations, it will soon be completely forbidden by European environmental directives. Therefore, finding a good substitute is of crucial importance.

Electrical arc erosion plays a crucial role in the reliability and life of power switching devices. Depending on the contact material's behavior in response to an electrical arc, surface damage can induce severe changes in contact material properties that will impact the power switching device's functioning. Consequently, electrical arc effects and consequences on the contact material surface are of first importance.

In this context, we have focused our research activities on the following axes.

First of all, in order to better understand AgCdO (Current contact material in aerospace industry) and AgSnO<sub>2</sub> (Potential candidate to AgCdO substitution) arc erosion behaviors, arc erosion experiments, where the power switching devices have been subjected to different numbers of arc discharges, have been realized.

Further, a general macroscopic electrical contact arc erosion model valid for low and high currents was developed. To compare model results to experimental data, this model describes the complete breaking process of electrical contacts and gives the total amount of material removed after one breaking operation. In parallel, arc erosion experiments on AgCdO power switching devices have been conducted at high currents (0 -> 1000 A) in order to validate the arc erosion model.

Next, using the general arc erosion model, the properties having the greatest influence on the electrical arc erosion process have been determined through simulations on silver contact material. At this stage, *ab initio* calculations were needed to obtain ranges of variation of certain silver contact material properties.

Finally, an investigation of the trends of changing local contact material composition of  $\text{AgSnO}_2$  on these identified material properties was performed. This study was based on *ab initio* calculations for two different oxide compositions of  $\text{AgSnO}_2$ .

These will allow us to give directions to aid the design of a good substitute for  $\text{AgCdO}$ , and therefore, to complete the main objective of this research work.



# CHAPTER 1

## INTRODUCTION

Since the early 1800's, electrical contacts have been used as mechanical switching devices in electrical devices. Nowadays, they are everywhere and equip power switching devices aimed at all kinds of industrial applications: space shuttle, airplane, automobile, modern electric apparatuses, etc... As an example, automobiles are made of dozens of electrical contacts whereas the last military airbus A 400 M is made of thousands.

AgCdO is one of the most widely used contact materials in the world because of its outstanding performance in power switching devices. However, recent European environmental directives tend to forbid its use in order to reduce pollution and human health risk. For these reasons, AgCdO is being replaced by some environmentally friendly contact materials such as AgSnO<sub>2</sub> in the automotive industry. Nevertheless, none of those replacement contact materials does meet the requirements relative to the aerospace industry where constraints related to a harsh environment are much more demanding. Moreover, major evolutions in embedded electrical systems, such as the replacement of hydraulic and pneumatic systems by electrical systems in aerospace industry (flight-by-wire), and the increased emphasis on safety for passengers, require the

development of a new generation of contact materials. Therefore, despite exemptions in the aerospace industry allowing it to keep using AgCdO for a limited amount of time, finding a good AgCdO substitute is becoming a pressing issue. In this context, this research project, whose main objective is to give directions to aid the design of a good substitute for AgCdO, is born from a strong partnership between Esterline Power Systems (ex Leach International) and Georgia Tech. Esterline is a specialized manufacturing company principally serving aerospace and defense markets where Esterline Power Systems is the world leader and largest manufacturer of relays and contactors.

Because serious accidents have been caused by contact failures, contact reliability is one of the most important factors for the design of such apparatuses. Arc erosion induced by the electrical arc at each contact opening and contact closing plays a major role in reliability (life of power switching devices) and safety (failure modes and effects). Indeed, surface damages resulting from arcing can lead under a certain number of operations to contact failure, i.e. the power switching device can not fulfill anymore one of the functions it has been designed to due to contacts welding, contacts destruction, etc.. Therefore, a better understanding of the different erosion mechanisms involved with arcing is a key factor in the process of designing an AgCdO substitute.

### **1.1. Arc erosion: breaking arc and material transfer**

This section aims at describing, based on the Particle Sputtering and Deposition model (PSD) developed in a review of arcing effects [1], the electrical arc formation and

its related material transfer during the breaking process of electrical contacts. Only contact opening is considered in this research project, especially in order to disregard bouncing effects while contacts close, as these can create an uncontrollable number of arc discharges.

Whenever contacts start separating, because of electrode surface roughness, the current carrying points of contact are reduced to a few points (See Figure 1.1-1). This kind of current constriction results in ohmic heating which melts the contact material in the vicinity of these constriction points.

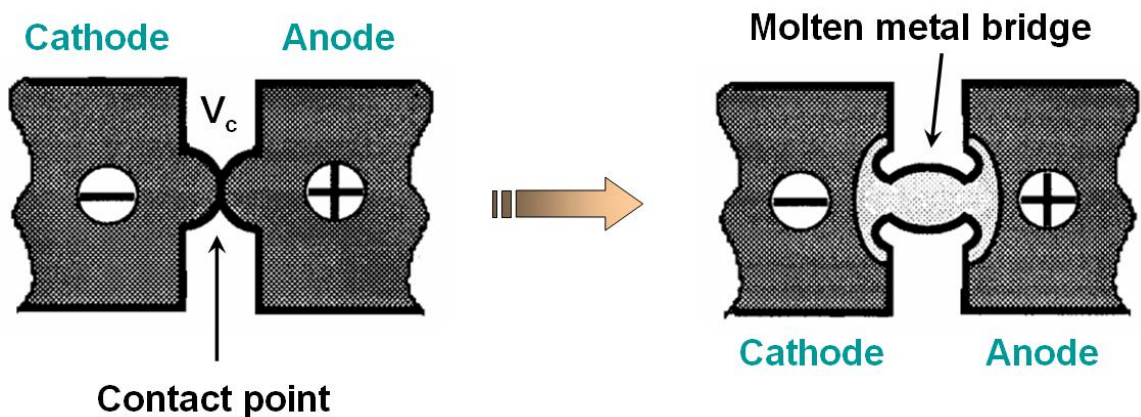


Figure 1.1-1: Schematic representation of a static contact and of a molten bridge formation

On further separation of the electrodes, this molten metal is pulled into a bridge, called the molten bridge (See Figure 1.1-1). As the electrode gap increases, the diameter of the molten bridge decreases, and, as can be seen with the following equations from [2], the voltage drop across the contacts rises due to the increase of the contact resistance.

The voltage drop across the contacts can be written as:

$$V_c = iR_c \quad (1.1)$$

Where the contact resistance  $R_c$  is given by:

$$R_c = \frac{\rho}{2} \sqrt{\frac{\pi H}{F}} \quad (1.2)$$

Where  $\rho$  is the resistivity

$H$  is the material hardness

$F$  is the holding force

Then, this molten bridge will be drawn out until it boils at its hottest part at contact voltage value corresponding approximately to the boiling points of electrode metals. This temperature growth at the contact spot  $T_c$  as a function of the contact voltage can be seen through the following equation from [2]:

$$T_c^2 = T_0^2 + V_c^2 \times 10^7 K \quad (1.3)$$

Where  $T_0$  is the ambient temperature.

### 1.1.1. Metallic phase

Soon after the rupture of the molten bridge, the gap between the electrodes is filled by metal vapour coming from the explosion of the molten bridge. Since the gap between the electrodes is then so small that the electrical field can reach over about  $10^7$  V/cm, the hot tip on the cathode acts as a source of thermal electron and field electron emissions. Consequently, the tip is a thermal-field (T-F) electron emission source, and then it takes as an arc root. The electrons emitted from this tip, while accelerating by the electrical field, move toward the anode. And because of inelastic collisions between metallic vapour and these electrons, the ionization of metal vapor and the generation of many

more electrons can be observed at this stage, i.e., electron avalanches. As a result, the metallic phase arc is ignited.

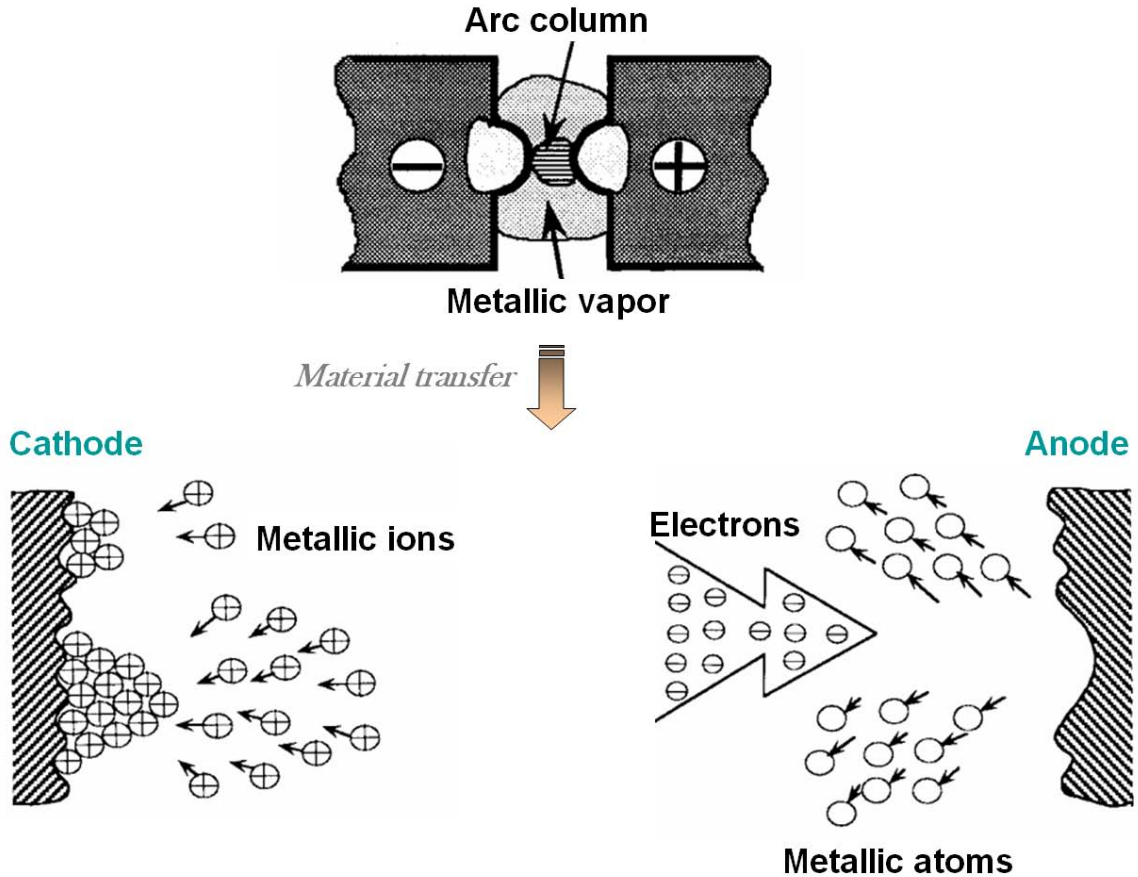


**Figure 1.1-2: Schematic diagram of PSD model: Metallic phase**

In the metallic phase, the arc takes place in the metal vapor, and the charged particles are mainly electrons (emitted from the cathode tip and reproduced by inelastic collisions with metallic atoms), metallic ions, and metallic atoms. Electrons, having obtained energy from the electrical field, move from the cathode to the anode and will impact in the anode: electron sputtering (See Figure 1.1-2). The metallic ions affected by electrical field impact in the cathode, which in turn results in the deposition of metallic ions on the cathode. As a result, during this metallic phase, the material transfer is from the anode to the cathode.

### 1.1.2. Gaseous phase

On further separation of the electrodes, higher ionization potential atmospheric ions play a larger part in arc conduction mechanisms, which lengthens the arc duration and changes its nature. Then, with time, the deposition of metal ions on the cathode and the deletion of metal ions through interdiffusion between metal vapour and the surrounding gas causes a reduction in the density of metal vapour between the electrodes, even though the electron sputtering on the anode surface can compensate for metal vapour loss. As the atmosphere gas becomes the main medium between the contacts, it will be ionized if the applied power voltage is high enough. As a result the gaseous ions will become dominant. The arc, now, begins to transfer from the metallic phase to the gaseous phase (See Figure 1.1-3).

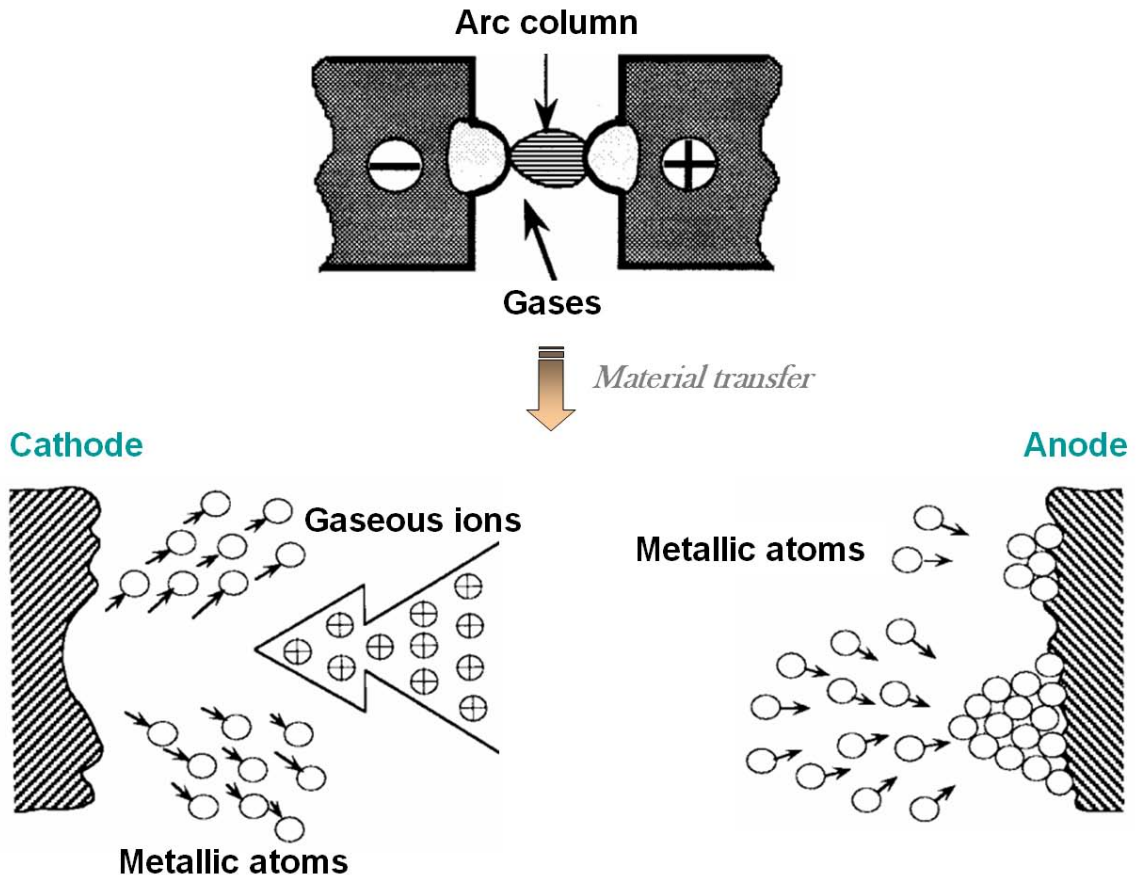


Figure 1.1-3: Schematic diagram of PSD model: Gaseous phase

In the gaseous phase, as can be seen on Figure 1.1-3, the dominant particles are gaseous ions, gaseous molecules/atoms and metallic atoms. During this phase, gaseous ions sputtering takes place; this phenomenon is equivalent to that which took place with electrons during the metallic phase when the gaseous ions bombarded the cathode. The sputtered particles (Metallic atoms) have then enough energy to shift to the anode and redeposit on it due to higher cohesive ability between the same particles. As a result, during this gaseous phase, the material transfer is from the cathode to the anode.

Therefore, based on the PSD model, in a breaking arc, the material is first transferred from the anode to the cathode (Metallic phase arc), and then, if the necessary conditions to have a gaseous phase are satisfied, from the cathode to the anode (Gaseous phase arc). As a result, the net transfer corresponds to the balance of these two opposite processes where both gain and loss happen either in the cathode or in the anode for each breaking operation.

Further separation of the contacts results in arc extinction, since it causes the circuit parameters to drive the arc below its minimum sustaining current. As time passes, the gap between electrodes increases to the point where it is so long that, because of the shortage of either electron emission or power supply, the discharge process can not produce enough positive and negative ions. As a result, the arc terminates.

Therefore, if the necessary conditions are satisfied, the breaking arc is first ignited in the metal vapor, then transfers from the metallic phase to the gaseous phase, and finally terminates. It has to be noticed that the arc won't occur or will immediately terminate if,

in the initial stage or during arcing, either the power supply or the electron emission is insufficient.

To conclude, during one breaking operation of electrical contacts, arc erosion results from the combination of:

- material removal due to vaporization of the electrode's contact material (mainly during the metallic phase arc)
- material removal because of the ejection of contact material particles from the electrode
- redeposition of vaporized or ejected electrode's contact material

## **1.2. Silver Metal Oxide based contact materials**

Silver metal oxide based contact materials (AgMeO) have been used as electrical contacts in a variety of switching applications, because they have been long recognized for their outstanding performance in make and break electrical contact applications and their good resistance to arc erosion.

### **1.2.1. AgCdO issue**

Silver cadmium oxide is the silver metal compound that is most widely used as electrical contact material as a result of its good arc erosion behaviour over a wide current range. Furthermore, its low erosion rate, good weld resistance and low interface resistance make it very effective in devices requiring many repetitive operations, like



relays and contactors. Consequently, silver cadmium oxide materials are the first choice in many contact applications.

Cadmium, as a heavy metal, has long been known to be very toxic, causing softening of bones, growth inhibition, malfunction of kidneys, and infertility. It and its compounds are extremely toxic even in low concentrations, and will bio-accumulate in organisms and ecosystems. It is carcinogenic, and it has high mobility in the environment. Due to its toxic nature and an increasing environmental awareness, the AgCdO should be replaced by a more environmentally friendly material. In order to reduce pollution and human health risk, the European Union (EU) has restricted the use of cadmium since 1967 and issued new European environmental legislation in 2003.

After almost twenty years of discussion in the electrical contact industry, the European Union has finalized several Directives (The End of Live Vehicles (ELV) Directive, The Waste Electrical and Electronic Equipment (WEEE) Directive and the Restriction of Hazardous Substances (RoHS) Directive) to restrict the use of cadmium in new electrical and electronic equipment by July 2006 [3], [4]. These directives provided a temporary exemption for Cd in electrical contacts used in the aeronautic industry. The ELV directive concerns equipment in automobiles below 3.5 t. With the RoHS directive, the EU covers consumer electrical and electronic devices and restricts the use of mercury (Hg), lead (Pb), hexavalent chrome (Cr VI), Cd and some plastic flame retardants. Clearly there is a need to replace the existing AgCdO contact materials with Cd-free materials having comparable contact properties. Thus there is a need to find contact materials that allow one-to-one substitution, without lowering performance.

### **1.2.2. On the way to AgCdO substitution**

A large number of researchers have been studying over the years in order to find out the specific material compositions that will produce a contact material having optimal performance. Nowadays, following the trend in the European market place to manufacture 'green' devices, another constraint that makes the problem even more complex is to develop contact materials that are Cadmium free. Years of development by contact manufacturers have produced many suitable replacement combinations of silver tin oxide, zinc oxide, indium oxide and mixtures of oxide. A large part of this effort has focused on materials based on silver tin oxide in the belief that the semi-refractory tin oxide particles would provide performance properties, especially resistance to contact welding and arc erosion, comparable to those of cadmium oxide; comparable but not the same and not as good in terms of overall behaviour.

Differences in erosion mechanisms and contact properties are mainly due to the considerably higher thermal stability of tin oxide and to the fact that CdO is wetted more easily by the silver melt than is SnO<sub>2</sub>. As a consequence, Silver/Cadmium oxide materials exhibit a somewhat more favorable overtemperature behavior than Silver/Tin oxide materials. Furthermore, many alternative CdO free contacts, particularly silver tin oxide (Ag/SnO<sub>2</sub>), are much more difficult to fabricate because of poor metallurgical properties. An earlier review by Shen [5] about the manufacturing difficulties and higher cost of CdO free contacts is still true today. Silver cadmium oxide with up to 15 % CdO can be made very efficiently by internal oxidation or powder metallurgy to include a range of physical, mechanical, metallurgical and electrical properties. However, both internal oxidation and powder metallurgy processes are complicated by the brittleness of many

non-CdO compositions. The most successful CdO substitution has been based on silver tin oxide with various additives [6]. It has been also found that the contact resistance and the temperature rise of Ag/SnO<sub>2</sub> are higher than those of Ag/CdO in the same conditions, so its applications have been limited [7]. But AgSnO<sub>2</sub>, with different additives to make up for its weaknesses, remains the best applicant to substitute AgCdO [8], [6]. Consequently, although silver/cadmium oxide (Ag/CdO) has been the preferred material for contacts due to its excellent performance properties and ease of manufacture into many configurations, silver/tin oxide contact materials have begun to replace silver/cadmium oxide materials in switching devices such as contactors, circuit breakers or relays. But power switching device manufacturers are still waiting for a better substitute. So, to end up with directions to design a good AgCdO substitute constitutes one of the main challenges of this research work

### **1.3. Methodology & outline**

The following action plan (See Figure 1.3-1) has been drawn up in order to identify the different research objectives that will lead to reach the main objective: to come up with directions to design a good AgCdO substitute. This methodology is based on experiments and modeling the electrical arc erosion phenomenon that takes place during one breaking operation of electrical contacts, since electrical arc erosion is the main source of power switching device failure.

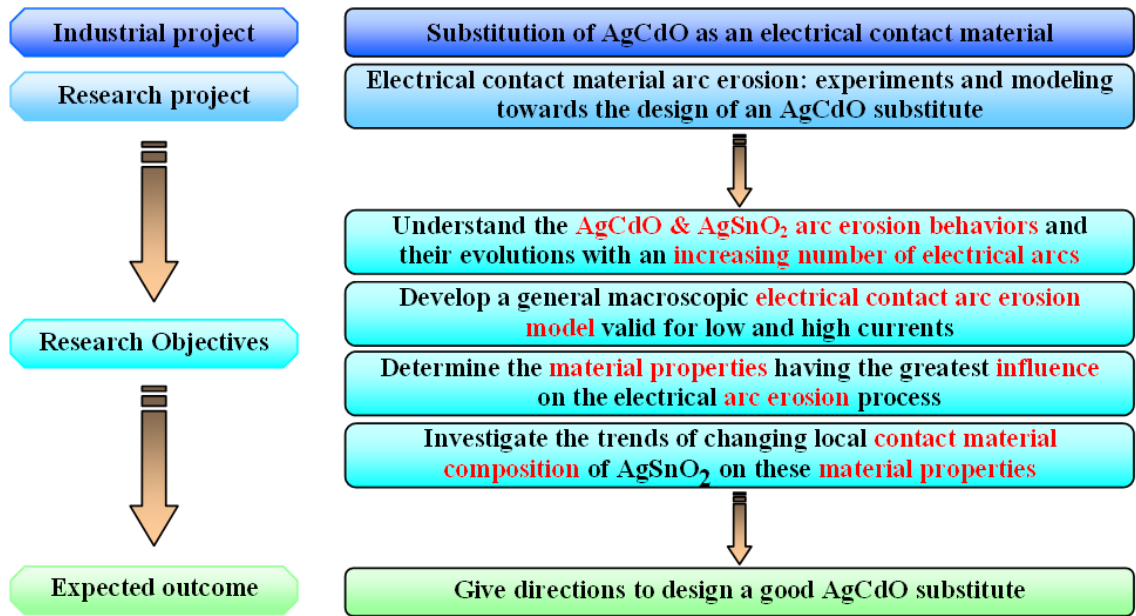


Figure 1.3-1: Schematic representation of the research action plan

Arcing changes the contact surface and layer local compositions, which in turn affects local contact material properties and thus impacts the contact material response to arcing. The contact material response to arcing will therefore evolve as a function of the number of arcs the electrical contacts will have been subjected to, and so, as a function of the number of breaking operations. Consequently, the first research objective will be to better understand AgCdO (the current contact material in the aerospace industry) and AgSnO<sub>2</sub> (a candidate to AgCdO substitution) arc erosion behaviors whenever those two contact materials are used in the same power switching devices as those operating in airplanes. And more specifically, through arc erosion experiments where the power switching devices will be subjected to different numbers of arc discharges, it will be to understand how local composition changes induced by arcing influence material properties such as the contact resistance. Those arc erosion experiments will be covered in Chapter 2 & 3.

The second research objective will then be to develop a general macroscopic electrical contact arc erosion model, valid for low and high currents, that will describe the whole breaking process of electrical contacts. To compare model results to experimental data, this model will have to describe the complete breaking process of electrical contacts and will have to give the total amount of material removed after one breaking operation. In parallel, arc erosion experiments on AgCdO power switching devices will be conducted at high currents (0 -> 1000 A) in order to validate the arc erosion model. The development and validation of this general arc erosion model will be detailed in Chapter 4.

The material response to arc erosion mainly depends on its properties. Therefore, the third research objective will be, using the general arc erosion model, to determine through simulations on silver contact material the properties having the greatest influence on the electrical arc erosion process. At this stage, *ab initio* calculations will be needed to obtain ranges of variation of certain silver contact material properties. This will be discussed in Chapter 5.

Once these important contact material properties in the arc erosion process have been identified, one question arises: how will a change in AgSnO<sub>2</sub> composition impact these identified contact material properties, and therefore, how will it affect its arc erosion behavior? Thus, the fourth and last research objective will consist in investigating the trends of changing local contact material composition of AgSnO<sub>2</sub> on these identified material properties. This study will be based on *ab initio* calculations for two different oxide compositions of AgSnO<sub>2</sub>. Chapter 5 will deal with this investigation.

Finally, Chapter 6 will give the conclusions and perspectives of this research work.

## CHAPTER 2

### AgCdO ARC EROSION BEHAVIOR

The formation of an electrical arc while contacts are opening results in changes of local surface and layer compositions and morphologies. These surface and layer dynamics play a crucial role in the contact material behavior in response to multiple electrical arcs. Indeed, the way the surface and the layer change after a certain number of arcs will directly impact the contact material properties and will consequently influence its response and performance.

Many studies have been undertaken in order to investigate AgCdO arc erosion behavior and to understand what makes AgCdO an outstanding contact material under exposure to increasing numbers of arcs. Most of these studies are based on comparison of arc erosion behaviors and contact material properties between AgCdO and some potential candidates for different applications: AgSnO<sub>2</sub> [3, 4, 6, 8-18], AgSnO<sub>2</sub>In<sub>2</sub>O<sub>3</sub> [11, 15, 19, 20], AgZnO [11, 14], AgNi [11, 12, 16-18], AgW [11, 16], AgCu [12, 16]. A few deal with X-ray study of AgCdO [21, 22], with metallurgical study of AgCdO [23], with the effects of additives on the microstructure and properties of AgCdO [24], with the thermophysical properties of AgCdO [25] and with the effect of arcing on the microstructure and

morphology of AgCdO [26-29]. But none of them relates the surface and layer dynamics of the AgCdO contact material to its properties of good resistance to arc erosion, whereas defining what makes AgCdO a good contact material is the first and a crucial step in the process of designing a good substitute. Therefore, experimental investigations were conducted in order to identify and to better characterize the surface and layer microstructure changes induced by an electrical arc and how surface and layer dynamics work as the number of arcs increases.

The main purpose of these arc erosion experiments is to better understand how the AgCdO contact material surface and layer change with an increasing number of arcs, when operated in the same conditions as they are utilized in airplanes, and those, from a local composition and a morphological point of view. Effects related to these changes on the evolution with the number of arcs of the contact material properties such as the contact resistance will also be in the scope of this study. Furthermore, AgCdO arc erosion behavior will be described through the two stage model defined by Wan in [14] with new definitions of the adjustment and of the quasi-steady states.

## **2.1. Arc erosion experiments**

In cooperation with our industrial partner Esterline Power Systems, arc erosion experiments have been conducted on AgCdO power switching devices in conditions similar to operating conditions in airplanes. Five AgCdO electrical contacts have then been tested under the exposure to different numbers of arcs: 1, 2, 3, 10, and 100 electrical arcs.



### 2.1.1. Sample Definition

The electrical contacts are all composed of a moving electrode and a static one, as presented on Figure 2.1-1.

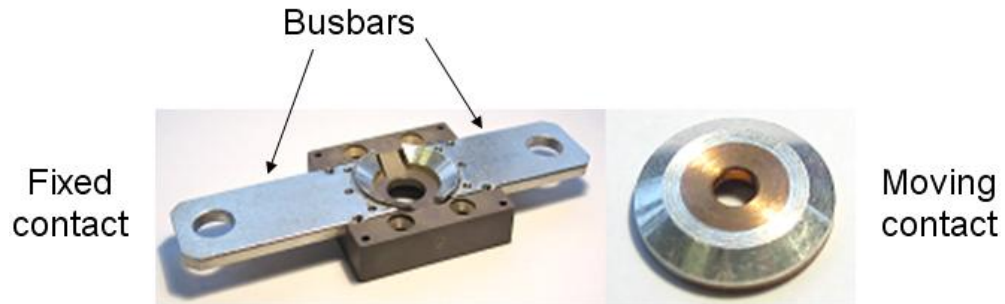


**Figure 2.1-1: Pictures of the static and the moving contacts used in this experiment**

As can be seen on Figure 2.1-2 below, the particularity of this kind of electrical contact is that they have, from their design, two contact interfaces.

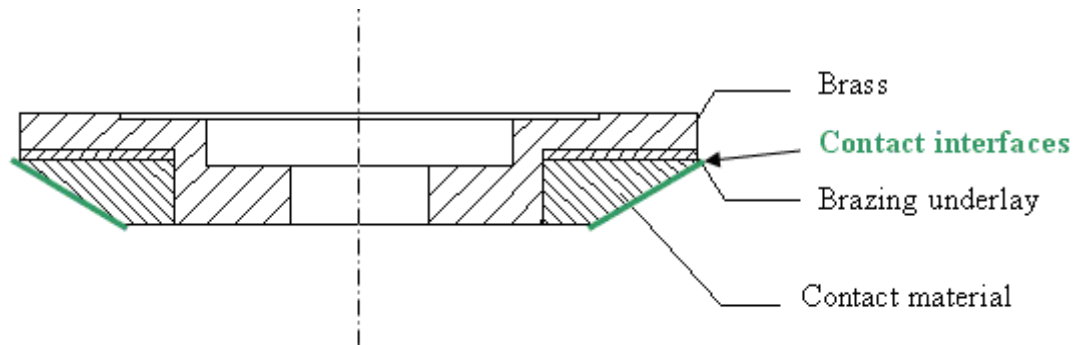


**Figure 2.1-2: Cut of the moving electrode**

Actually, the current being carried by the first busbar is passing through the moving electrode, whenever this one is in a closed position, to finally leave carried by the second busbar (See Figure 2.1-1). This is very interesting since the moving electrode then plays both anode and cathode roles, and we will be able to observe the two kinds of behaviour on the same electrode. That is very convenient for the analysis part because it is easy to manipulate a small piece such as the moving electrode. Consequently, we will mainly focus our work on the moving electrode.

From a composition point of view, we are using five test contacts of 90%Ag-10%CdO (by weight) that were all prepared by powder metallurgical techniques. The process used is sintering. These contacts with silver backings were brazed to copper cylindrical pieces so that they could be positioned in the power switching device. The moving electrodes were all 22 mm in outer diameter and 3.5 mm in height.

### **2.1.2. Test Condition and Testing Procedure**

The five contacts have all been tested under the same operating conditions: Supply current of 400 A, Circuit voltage of 28 V DC, Ambient: air, room temperature.

The only difference between these contacts lies in the number of breaking operations they have been subjected to. The purpose being to study and understand the effects of an increasing number of electric arcs on the contact material, we decided to make the first AgCdO sample undergo one “half-cycle” (only one break operation); the second one, two; the third one, three; the fourth one, ten and finally the fifth one, a hundred half-cycles. For every arc discharge, the contact resistance was measured.

Several reasons can explain the decision to work with half-cycles. The most important one is that we want to control the number of electric arcs that hit the contact material, and operating the contact only during the opening cycle allows us not to deal with the bounces of contacts induced while closing. An uncontrolled number of very destructive short arc discharges depending on the number of bounces is then one of the main effects of these contact bounces while closing, and we want to avoid these because they are unpredictable. Another reason for using this “half cycle” testing procedure is to eliminate mechanical erosion that may occur during the closing of contacts. Indeed, this

study intends to study only the contact material erosion due to the arcing phenomenon.

### 2.1.3. Experimental Set Up

The experiments were realized at Esterline Power Systems in Niort (France). Pictures of the experimental set up can be seen in Figure 2.1-3.



Figure 2.1-3: Experimental set up

The supply current is 400 A and the circuit voltage is 28 V DC. The tests have only been conducted under resistive load.

Here is the scheme of the circuit:

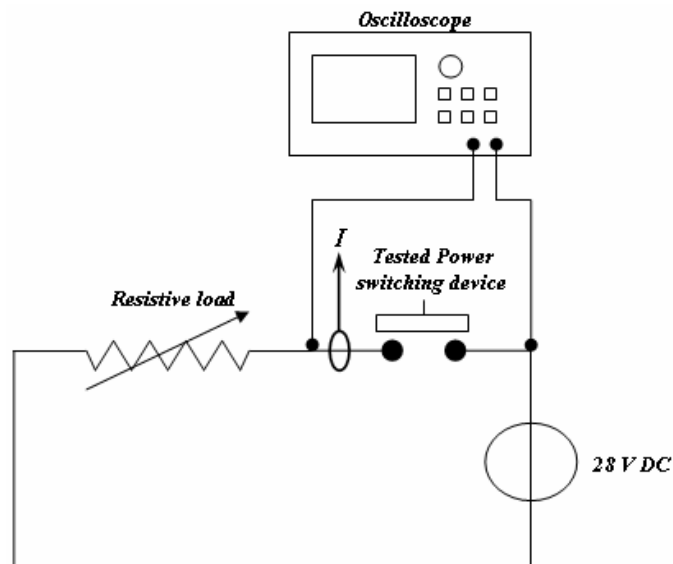


Figure 2.1-4: Experimental system

Instantaneous arc current and voltage drops have been reported for each cycle, and the average contact resistance over the cycle was calculated.

#### **2.1.4. Experimental apparatus**

Initial observations were made using a binocular microscope with high magnification to identify interesting zones to scan. Then, to be more accurate in our analysis, we used a Scanning Electron Microscope with an energy-dispersive x-ray spectrometer (EDS) to get the chemical composition of areas of interest.

## **2.2. AgCdO Surface Dynamics**

This section is focused on the study of the evolution of the contact surface with the number of electrical arcs under the operating conditions above mentioned. The following pictures correspond to the anode behavior on the moving electrode after a certain number of electrical arcs.

#### **2.2.1. Experimental results**

Each sample has been studied using the same methodology. The following pictures represent arc impacted areas, which have been selected after observations with a high magnification microscope and after an EDS mapping of certain parts of the crater (Figure 2.2-1) in order to identify representative and characteristic microstructures and chemical compositions.

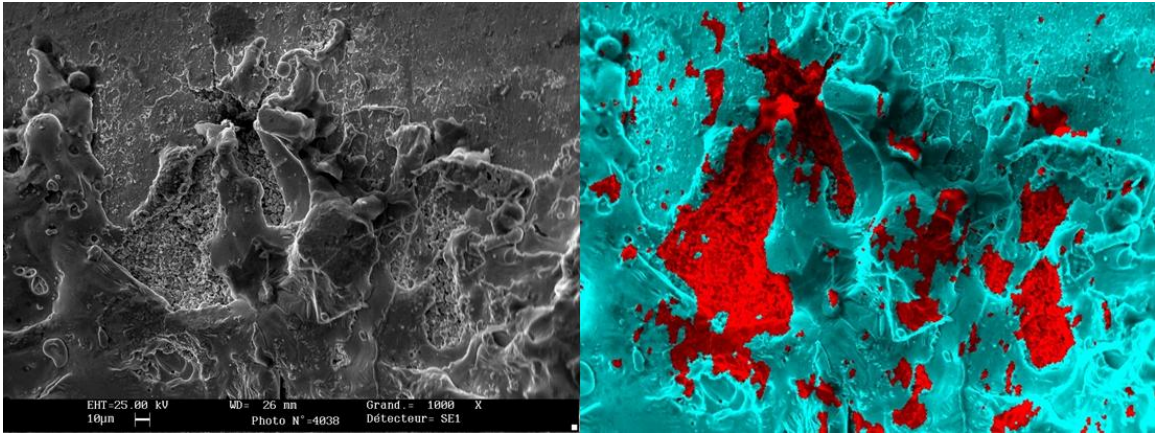


**Figure 2.2-1: EDS mapping of one part of the crater after one electrical arc (x800) - Anode**

The rectangles in Figure 2.2-2 correspond to zones, having some noticeable differences from a morphology point of view, which we scanned to get their chemical compositions.

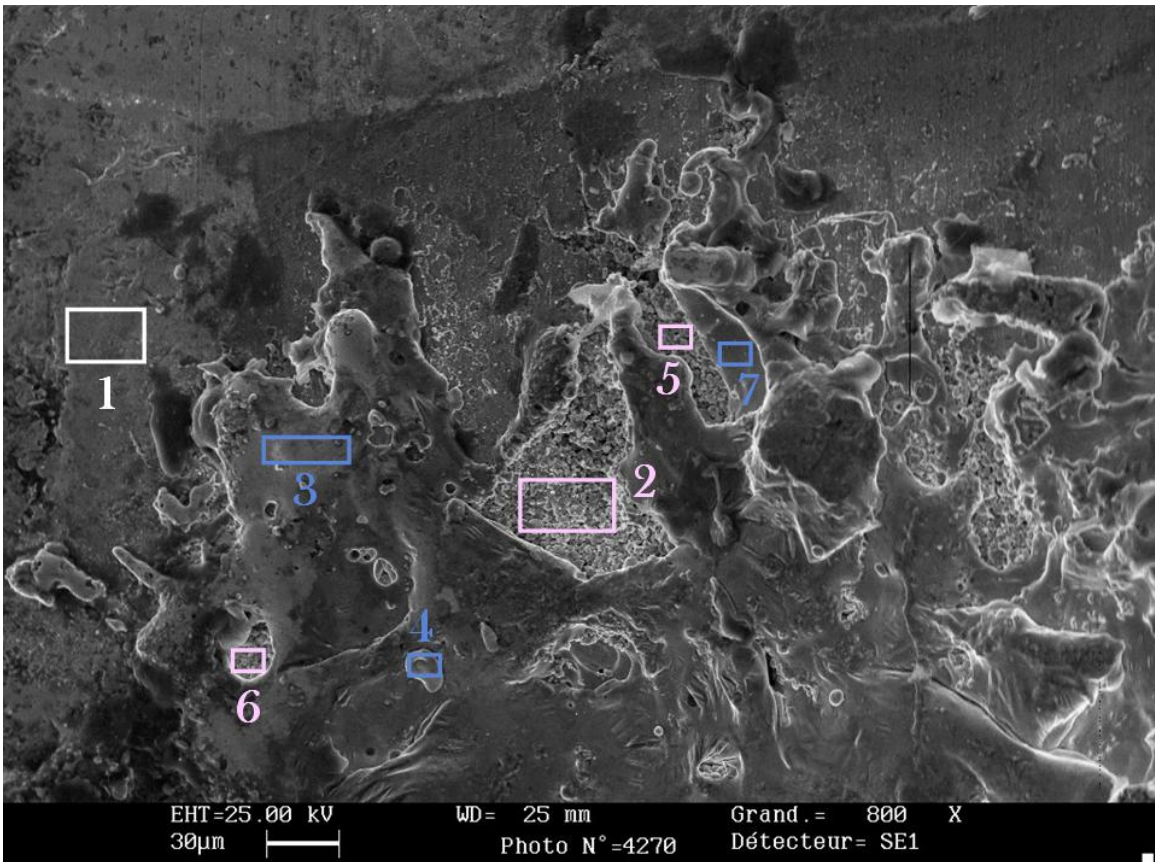


**Figure 2.2-2: SEM picture of a characteristic part of the crater after one electrical arc - Anode**

For each zone, we get as results of the scan the following spectrum (Figure 2.2-3) allowing us to identify the composition in elements:

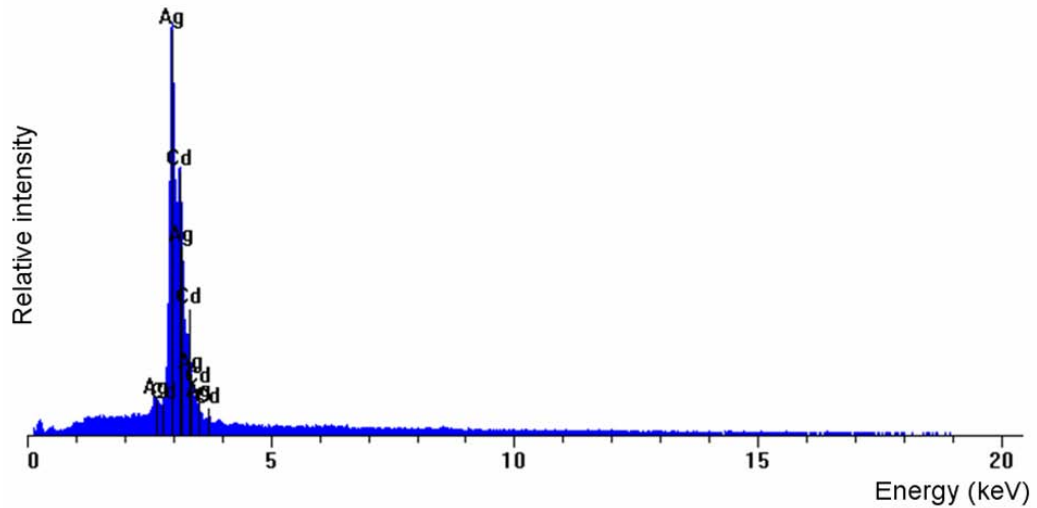


Figure 2.2-3: Chemical composition spectrum relative to zone 1 (Figure 2.2-2)

The element compositions of the different zones are summarized in the following table.

Table 2.2-1: Chemical composition of the different zones relative to Figure 2.2-2

	Composition (% weight)	
Zone	Ag	Cd
1	88	12
2	41	59
3	93	7
4	96	4
5	18	82
6	17	83
7	92	8

From Figure 2.2-2 and Table 2.2-1, we can group zones by similarities in morphology and in chemical composition. They can be sorted into 3 groups:

- Group I: Zones 2, 5, 6, corresponding to zones where we can observe cavities full of spherules whose chemical composition is mainly cadmium oxide.



- Group II: Zones 3, 4, 7, corresponding to parts of the surfaces surrounding the holes with spherules, to solidified parts of the melting bath and also to deposited droplets. They have high silver ratio in composition (above 90%).

- Group III: Zone 1, corresponding to solidified parts of the melting bath and also to areas that have not been impacted by the electrical arc. Their compositions in silver are below 90% but they are still close to the original chemical composition of the contact material.

What will change with the number of arcs is the proportion of impacted areas belonging to each of these three groups, directly depending on surface dynamics.

The impacted anode surface after two electrical arcs is shown in Figure 2.2-4. The eroded area is approximately 2.2 mm in diameter.

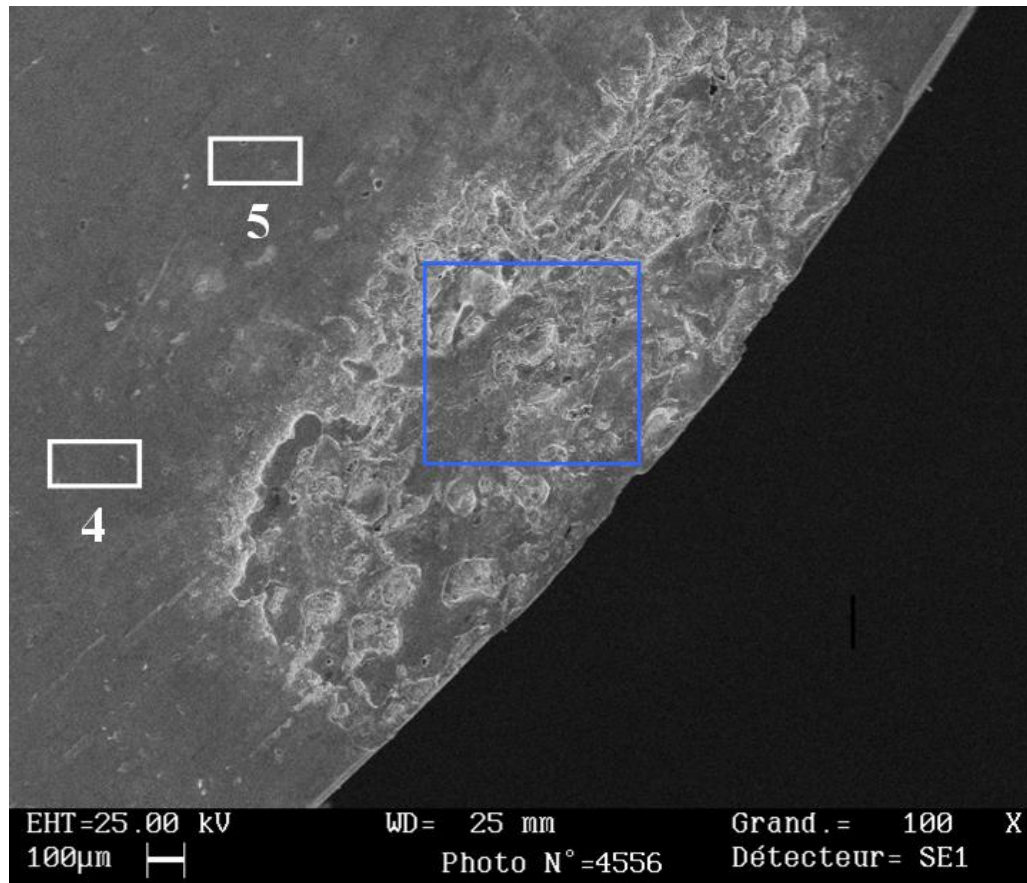


Figure 2.2-4: SEM picture of the crater after two electrical arcs – Anode

The same lunar surface we have noticed earlier after one electrical arc can be observed on the close-up of the area limited by the blue frame (Figure 2.2-5).

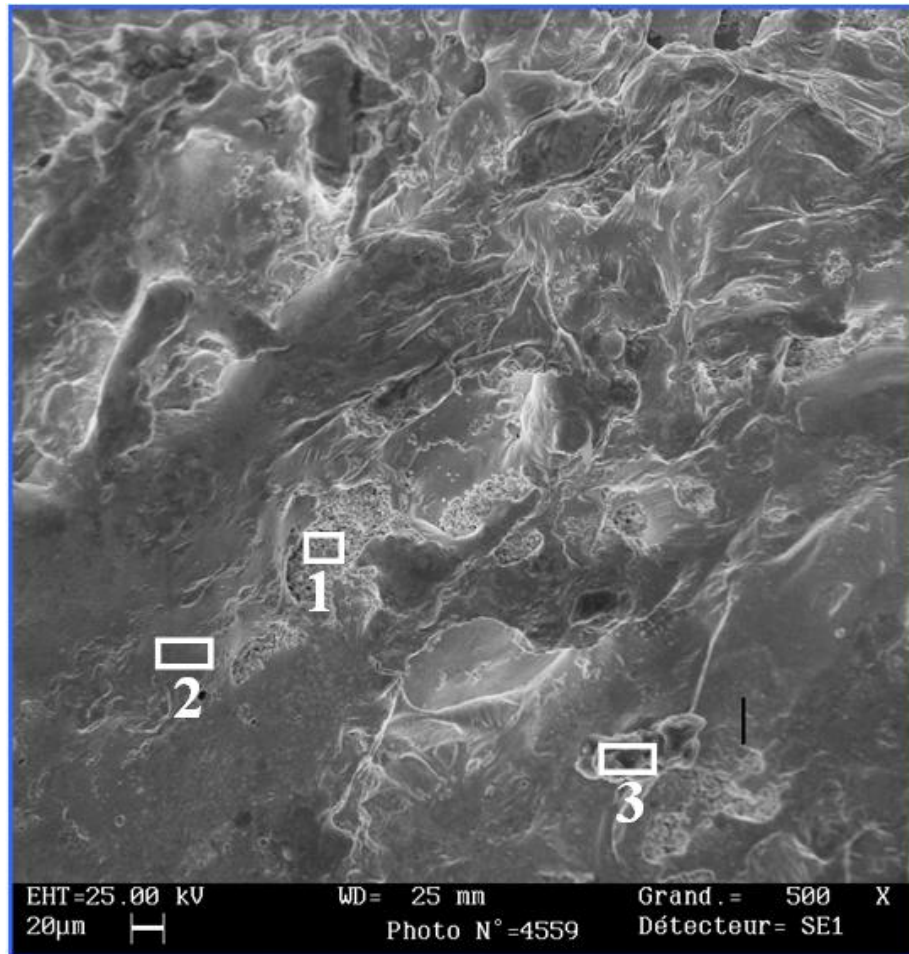


Figure 2.2-5: Close-up of the blue frame (Figure 2.2-4) – Anode

Table 2.2-2: Chemical composition of the different zones relative to Figure 2.2-4 & Figure 2.2-5

	Composition (% weight)	
Zone	Ag	Cd
1	44	56
2	42	58
3	12	88
4	95	5
5	90	10



Surfaces can be remarked as belonging to the three groups we defined earlier in the case of one electrical arc. One big difference here, after two arcs in comparison to one, is the trend of an increase in the cadmium ratio of the solidified molten bath (Zone 2).

Furthermore, zone 3 is the perfect illustration of this trend of an increase in cadmium ratio close to the contact surface, and that results in minute molten-droplet splash erosion with more cadmium particles in composition. We could have guessed this high cadmium ratio in zone 3 by simply looking at the morphology of this deposited droplet where we can see granules.

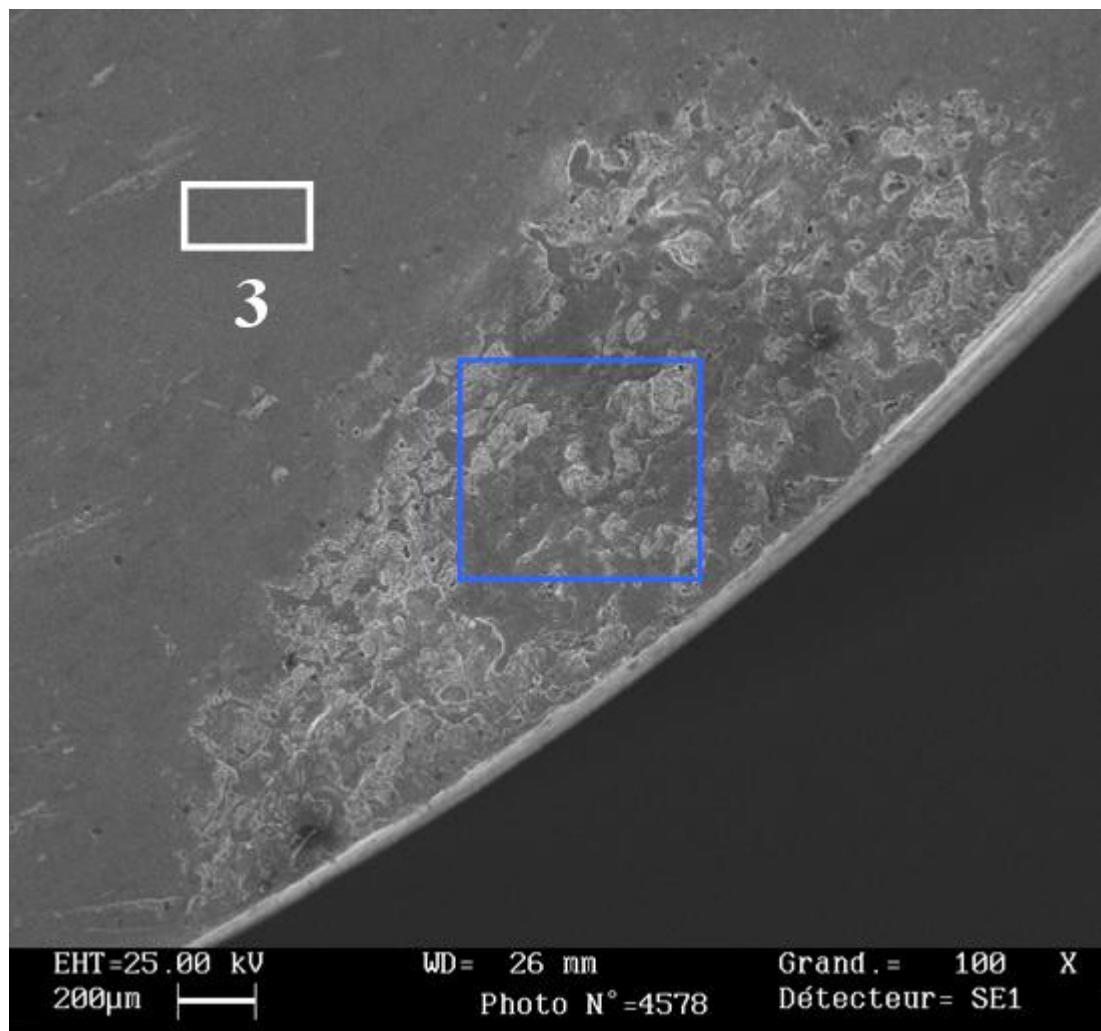
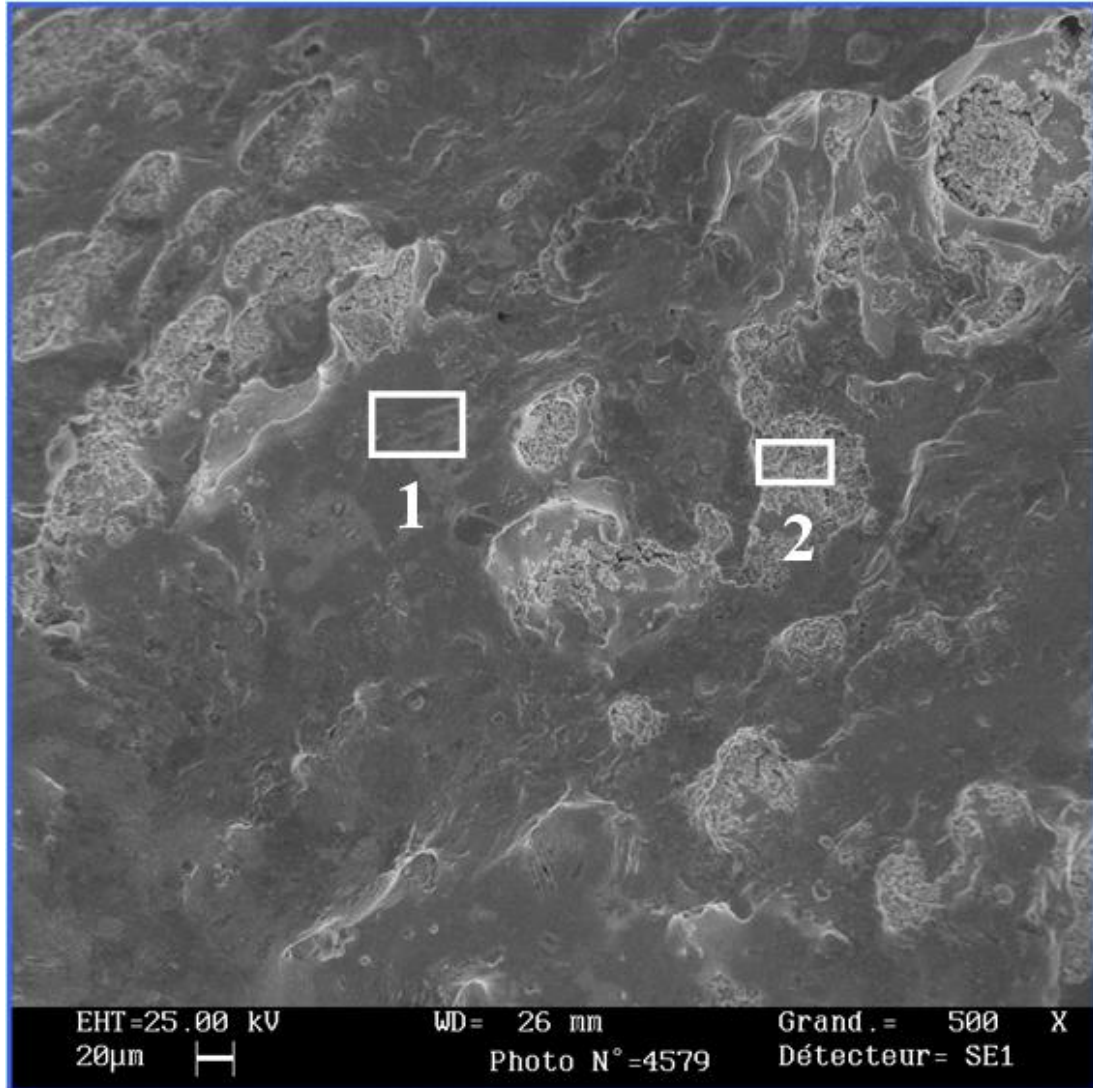


Figure 2.2-6: SEM picture of the impacted area after three electrical arcs – Anode

The 2.75 mm long impact, which can be seen in Figure 2.2-6, corresponds to an overview of the anodic behavior after three electrical arcs. Figure 2.2-6 demonstrates that the size of the cavities evolves with the number of arcs; from one to three electrical arcs, the number and mainly the size of the cavities keeps growing. This could be explained by a transient state, corresponding to the first few electrical arcs the contact material is subjected to, while cadmium oxide particles, under electromagnetic forces induced by the electrical arc, agglomerate to form bigger clusters. Within the molten bath, these clusters, under gravity effects, rise to the contact surface since silver density is about  $10.49 \text{ g/cm}^3$  and cadmium oxide density is about  $7.28 \text{ g/cm}^3$ .

**Table 2.2-3: Chemical composition of the different zones relative to Figure 2.2-6 & Figure 2.2-7**

	Composition (% weight)	
Zone	Ag	Cd
1	90	10
2	29	71
3	93	7



**Figure 2.2-7: Close-up of the blue frame (Figure 2.2-6) - Anode**

The chemical composition of the solidified molten bath gradually oscillates from rich-cadmium oxide areas close to cavities of granules to rich-silver areas in comparison to the original composition in between. The composition of Zone 1, located in between two cavities in Figure 2.2-7, is close to that of the original one (see Table 2.2-3).

The morphology after ten electrical arcs, as can be seen in Figure 2.2-8, looks different. A few cavities can be observed, and their size has stopped growing. Most of them have been filled up or covered by the molten metal during solidification.

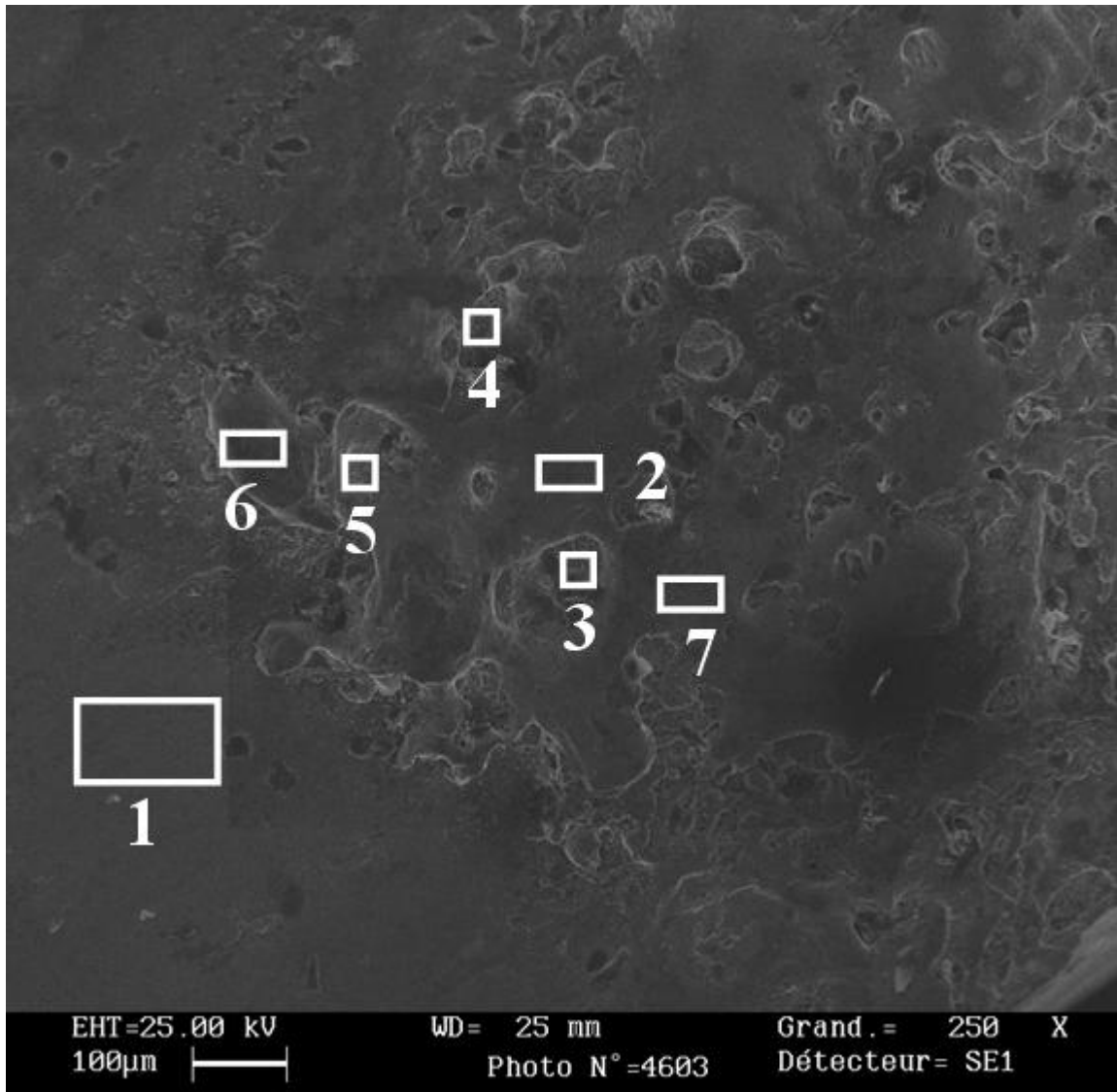


Figure 2.2-8: SEM picture of the impacted area after ten electrical arcs – Anode

Table 2.2-4: Chemical composition of the different zones relative to Figure 2.2-8

Zone	Composition (% weight)	
	Ag	Cd
1	95	5
2	79	21
3	73	27
4	61	39
5	64	36
6	93	7
7	77	23

Consequently, the cadmium ratio of the solidified molten bath remains high. This is confirmed by Table 2.2-4, since zones including cavities with granules (Zones 3, 4 & 5) have, as expected, high ratios of cadmium, but also zones surrounding these cavities (Zones 2 & 7) get important cadmium ratios in comparison to the original composition. In addition we still observe a few low mounds (Zone 6) whose composition is mainly oxide-depleted metal. This can be explained by the phenomenon of agglomeration of cadmium particles that we mentioned earlier that creates deprived cadmium oxide areas. Splash erosion and material deposition from the other electrode can be another way to explain it.

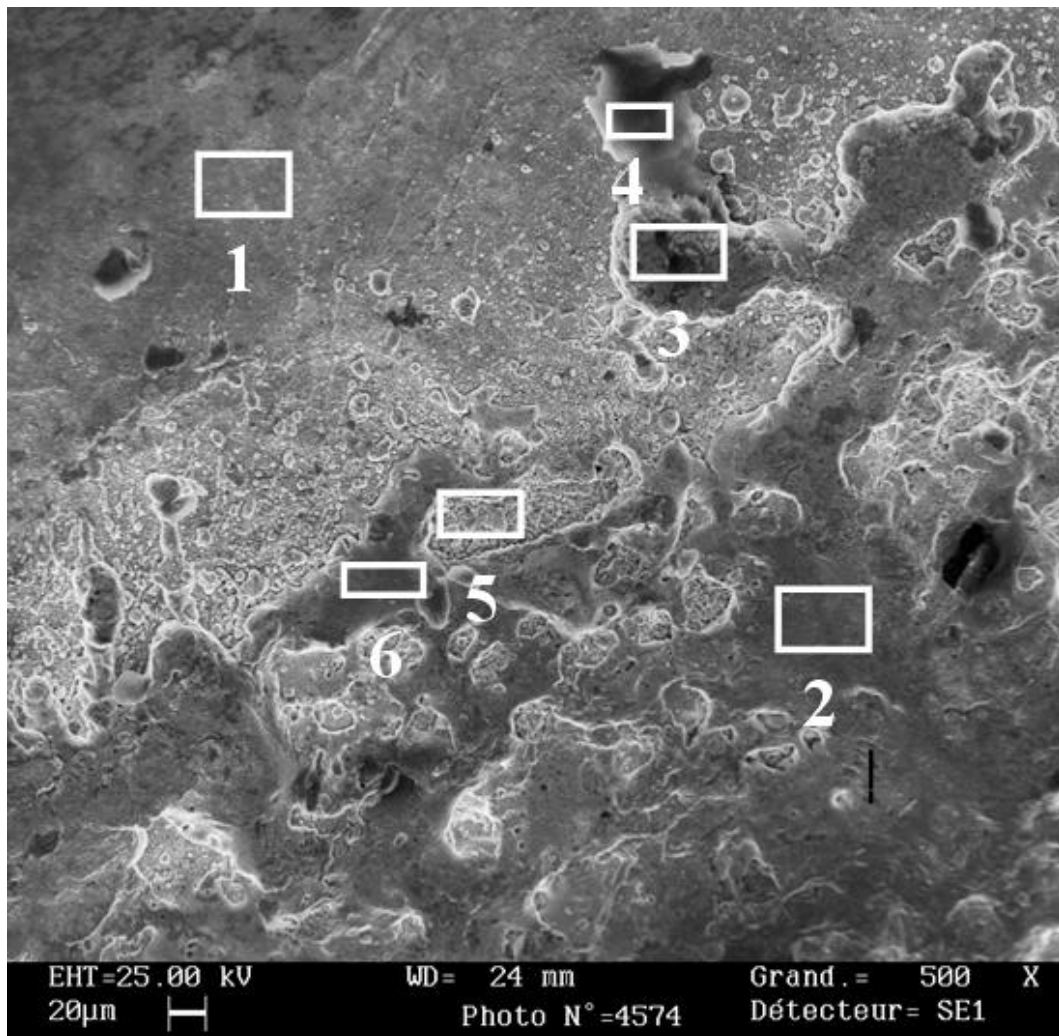


Figure 2.2-9: SEM picture of the impacted area after one hundred electrical arcs – Anode

**Table 2.2-5: Chemical composition of the different zones relative to Figure 2.2-9**

	<b>Composition (% weight)</b>	
<b>Zone</b>	<b>Ag</b>	<b>Cd</b>
<b>1</b>	87	13
<b>2</b>	86	14
<b>3</b>	41	59
<b>4</b>	53	47
<b>5</b>	55	45
<b>6</b>	84	16

The appearance of the impacted surface after one hundred electrical arcs (Figure 2.2-9) highlights some changes in surface dynamics. Indeed, we can first notice that the size of the cavities has decreased, which goes with the size of the cadmium oxide clusters. In addition, Table 2.2-5 corroborates the fact of a high cadmium oxide ratio at the contact material surface. This can be explained by the distribution and the size of the cadmium oxide clusters, since they are smaller and finely and homogeneously dispersed within the impacted layer. So oxide-depleted areas are rare, as can be seen in Table 2.2-5. Furthermore, we can observe many particles that look like droplets coming from splash erosion.

### **2.2.2. Discussion**

The way surface dynamics of AgCdO works contributes to good arc erosion properties. The contact surface renews itself at each electrical arc, like the skin but not with the same features and consequently not with the same properties. As mentioned in [14], we can define two states to describe these changes.

The first few electrical arcs would correspond to a transient state where we can observe agglomeration of cadmium particles in bigger clusters and around the same number of impacted surface areas belonging to the three groups defined earlier. This implies decreasing viscosity, thermal conductivity and electrical conductivity and increasing contact resistance during this phase.

With increasing numbers of electrical arcs, we reach a quasi-steady state where properties oscillate around an average value. During this phase, the size and distribution of cadmium oxide clusters change. These clusters become smaller and are homogeneously and finely dispersed. This gives good contact erosion properties: higher viscosity preventing contact material from splash erosion, higher thermal conductivity allowing heat to go through the contact layer faster and so, to reduce the temperature elevation, higher electrical conductivity giving better electrical features to the contact and lower contact resistance preventing the contact from heating up. Furthermore, the high cadmium oxide ratio during this phase gives good anti-welding properties. A perfect illustration of these two states we just defined can be seen in Figure 2.2-10 where we reported the evolution of one property, the contact resistance in this case, as a function of the number of electrical arcs.



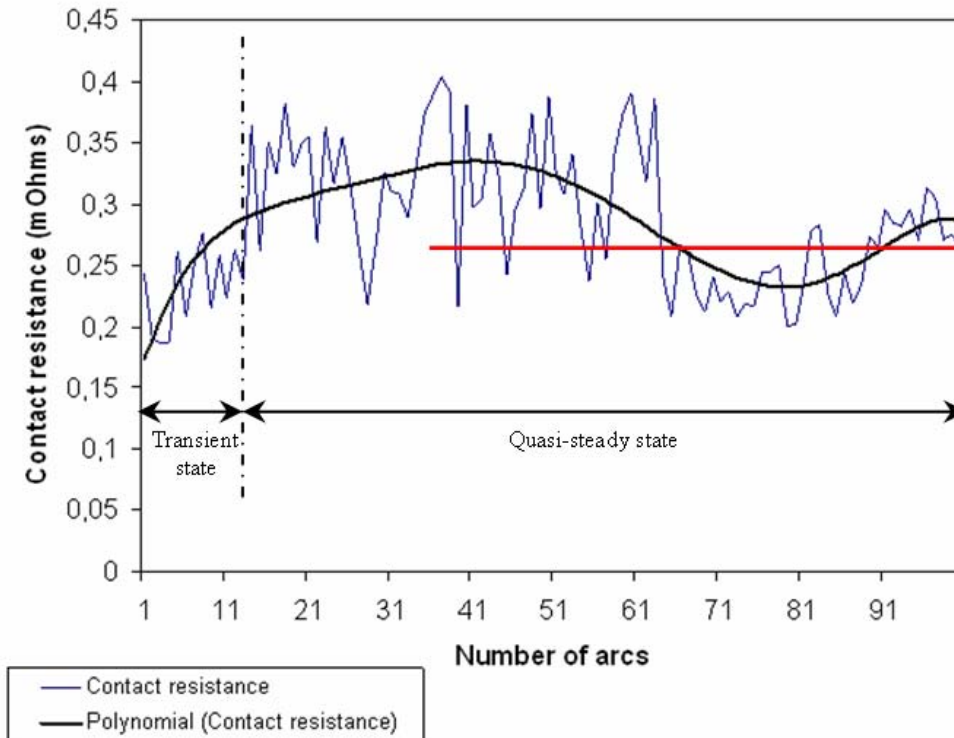


**Figure 2.2-10: Evolution of the AgCdO contact resistance with the number of arc (Data shown is the average of 5 sets of experiments)**

This shows that surface dynamics impact the contact material properties. The growing cadmium oxide clusters during the first phase reduce the electrical conductivity and consequently, increase the contact resistance. Then, in the second phase, the distribution of finely dispersed smaller clusters gives higher electrical conductivity and thus, reduces the contact resistance.

Cadmium oxide clusters play an important role in the surface dynamics of AgCdO. Whenever they rise to the contact surface, they create cavities full of granules (see Figure 2.2-11).



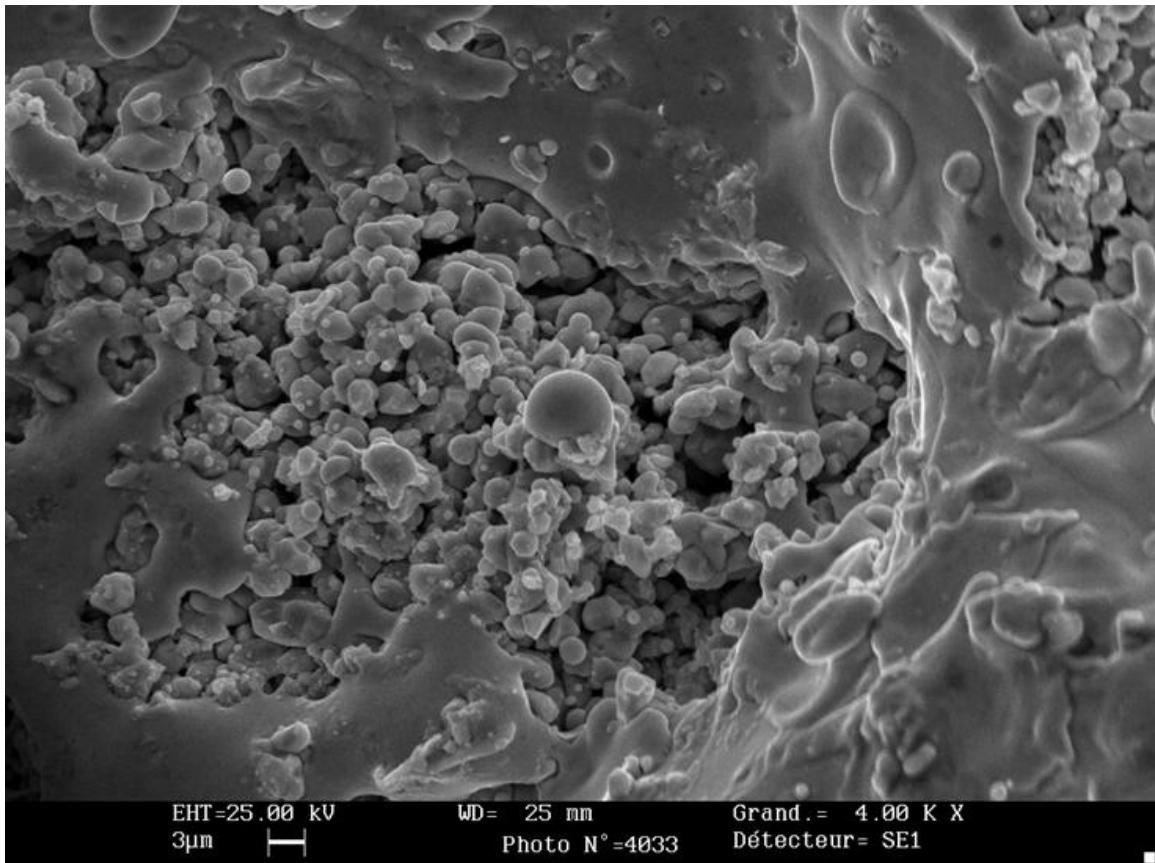


**Figure 2.2-11: SEM picture of a cavity full of granules - Anode**

Why? During the arcing process, there is formation of a molten bath of silver with cadmium oxide particles in it. Under the agitation induced by the electrical arc, cadmium oxide particles agglomerate to form bigger clusters. Within the molten bath, these clusters, under gravity effects, go up to the contact surface, since silver density is about  $10.49 \text{ g/cm}^3$  and cadmium oxide density is about  $7.28 \text{ g/cm}^3$ . Then, upon solidification, because the temperature of the melting bath corresponds to the melting temperature of silver ( $\sim 962^\circ\text{C}$ ) and the decomposition temperature of the cadmium oxide is about  $1000^\circ\text{C}$ , we can observe formation of oxygen bubbles within the molten bath that contributes to this granular shape.

This expulsion of oxygen during solidification of the molten bath with breakdown of cadmium oxide particles [6], and the combined effects of the vaporization of some of the cadmium oxide particles ( $\sim 1385^{\circ}\text{C}$ ) and some of the cadmium particles ( $\sim 765^{\circ}\text{C}$ ), are the reason why we observe these cavities with granules of cadmium oxide. Indeed, these clusters at the free surface, under the gaseous expulsion phenomena we mentioned, act like smokestacks during the cooling down process of the silver bath, thus preventing the surrounding molten silver that has not been resolidified yet from covering and filling up these cavities.

This formation of cavities is enhanced by the fact that molten Ag dissolves approximately 40 times more  $\text{O}_2$  than does Ag in solid state [14]. Upon solidification, this creates an excess of  $\text{O}_2$  which is rapidly expelled and contributes to the formation of cavities full of granules at the contact surface.

### **2.3. AgCdO Layer Dynamics**

This section is devoted to the study of the contact material layer dynamics of the same samples above analyzed. The following pictures also correspond to the anode behavior on the moving electrode after a certain number of electrical arcs.

#### **2.3.1. Experimental results**

In order to study the contact material layer behavior with arcing, all the samples have been cut after experiments according to a vertical plan located at 1 mm from their periphery. In Figure 2.3-1, we can see the initial configuration of cadmium oxide

particles within the contact material layer before arcing. It comprises some clusters of cadmium oxide particles surrounded by some cadmium oxide particles.

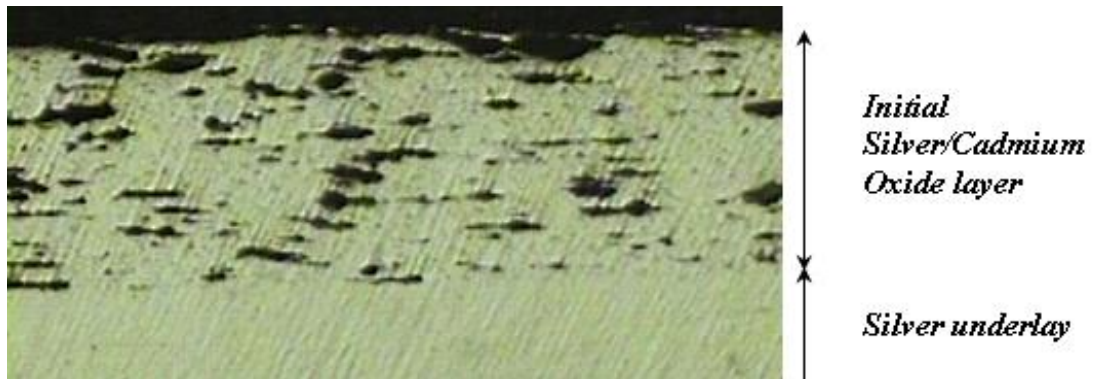


Figure 2.3-1: Binocular view of a section of the moving electrode before arcing (25x)

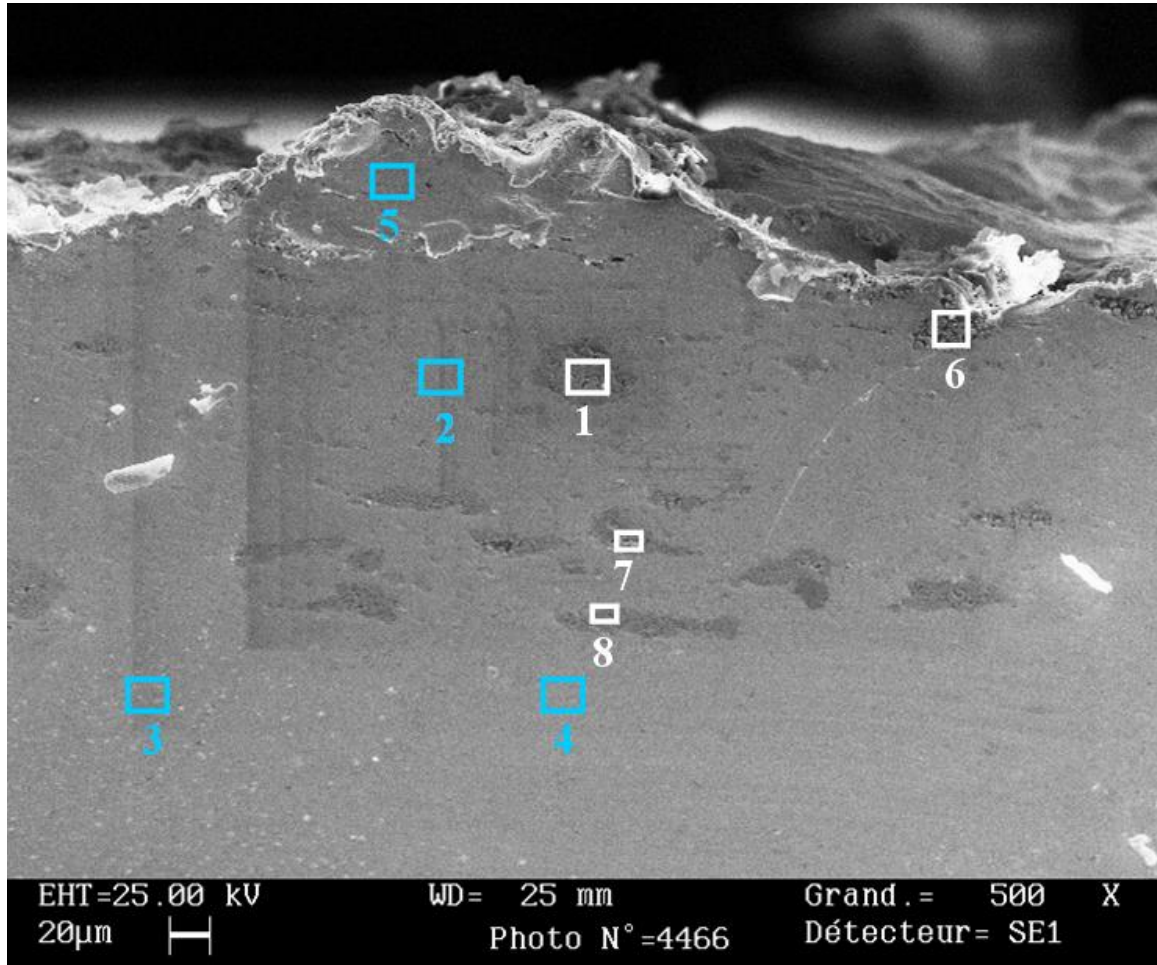
Some zinc particles were randomly deposited at the contact surface before the experiments began. Since the vaporization temperature of zinc is about 910°C and the temperature of the molten bath is about the melting temperature of silver which is about 962°C, only Zinc as an oxide ZnO will be considered within the impacted layer since its decomposition temperature is about 1975°C. The purpose is to use Zinc as a tag in order to know more about layer dynamics and the thickness of the impacted layer after arcing.



Figure 2.3-2: Section of the anode after one electrical arc (25x)

The impacted contact surface layer after one electrical arc (Figure 2.3-2) looks completely different with respect to Figure 2.3-1. Indeed, it seems that everything moved

within the contact material layer. This is confirmed by the presence of zinc oxides in Zones 1, 6, 7 & 8 in Figure 2.3-3 and Table 2.3-1. Fewer cadmium oxide clusters can be observed. In addition, they are much bigger and randomly distributed within the layer.



**Figure 2.3-3: SEM picture of the section of the anode after one electrical arc**

A chemical analysis has been performed on a part of the section of the sample having been subjected to one electrical arc (see Figure 2.3-3). The rectangles correspond to zones that have been scanned to get their chemical compositions. For each zone, we get as results of the scan the following spectrum (Figure 2.3-4) giving us the composition in elements.

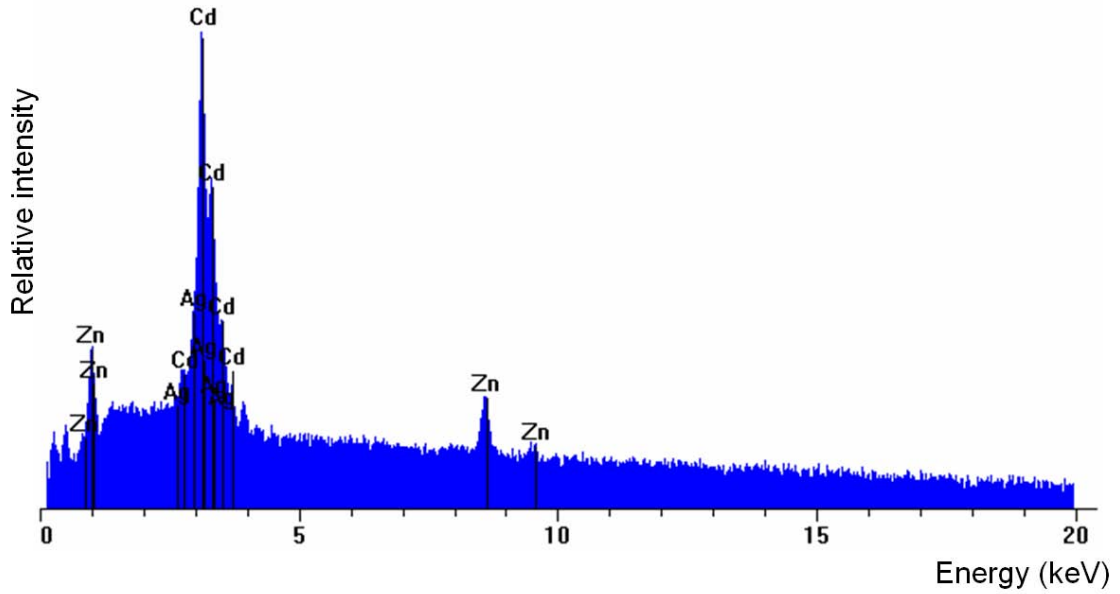


Figure 2.3-4: Chemical composition spectrum relative to zone 7 (Figure 2.3-3)

All the results describing the element compositions of the different zones have been summarized in the following table.

Table 2.3-1: Chemical composition of the different zones relative to Figure 2.3-3

Zone	Composition (% weight)		
	Ag	Cd	Zn
1	10	86	4
2	97	3	0
3	98	2	0
4	98	2	0
5	98	2	0
6	6	79	15
7	9	87	4
8	2	95	3

From Figure 2.3-3 and Table 2.3-1, results concerning a part of the impacted contact material layer subjected to one electrical arc, we can group zones by similarities in their morphology and in their chemical composition. They can be sorted into 2 groups:

- Group I: Zones 1, 6, 7, 8, corresponding to parts of the layer that have a high cadmium ratio in composition and some zinc. These are included within cavities full of granules (see Figure 2.3-5), the same as the ones noticed at the contact surface in the former section.

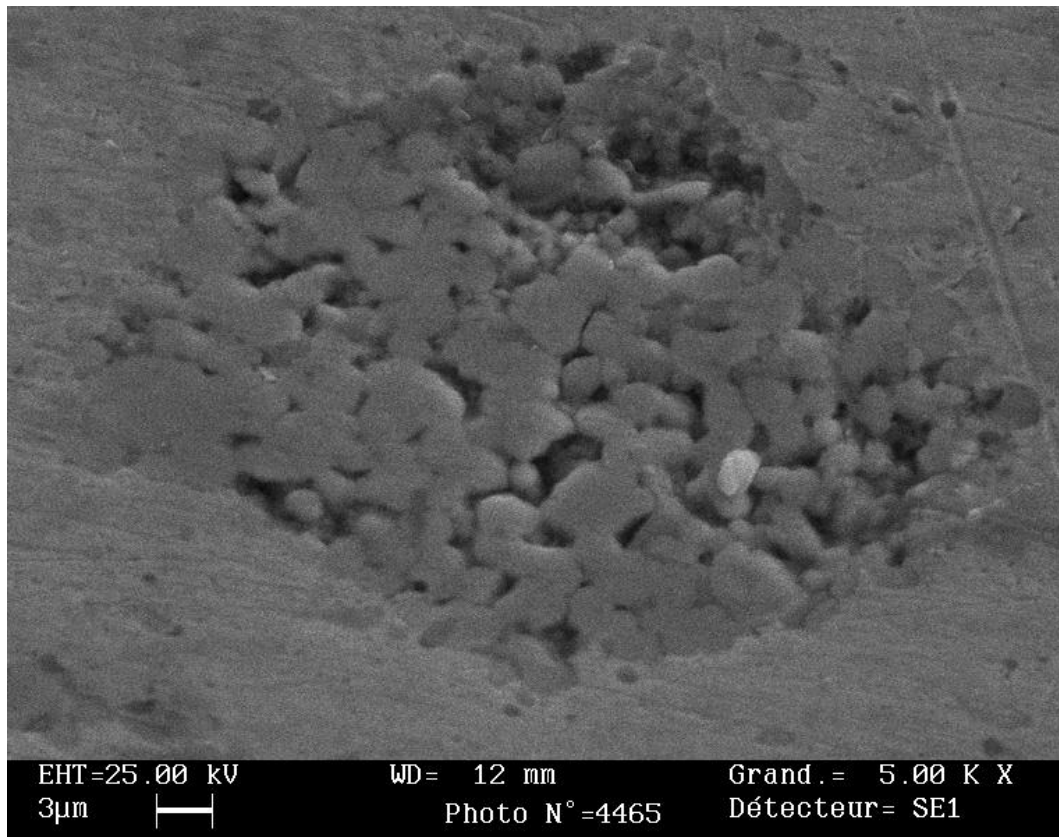


Figure 2.3-5: Close-up of the cavity enclosing zone 1 (Figure 2.3-3)

- Group II: Zones 2, 3, 4, 5, corresponding to parts of the layer that have a high silver ratio in composition (above 97%). These are surrounding cavities full of granules.

While performing the chemical analysis, no zinc was found in zones belonging to group II with high silver ratio. Furthermore, the presence of zinc oxide as deep as the



location of zone 8 allows us to deduce that at least all the initial contact material layer has been melted after the first electrical arc. The growth in size of cadmium oxide clusters could then be explained by the agglomeration of oxides, zinc and cadmium oxides, under moves or flows induced by electromagnetic forces arising from the electrical arc.

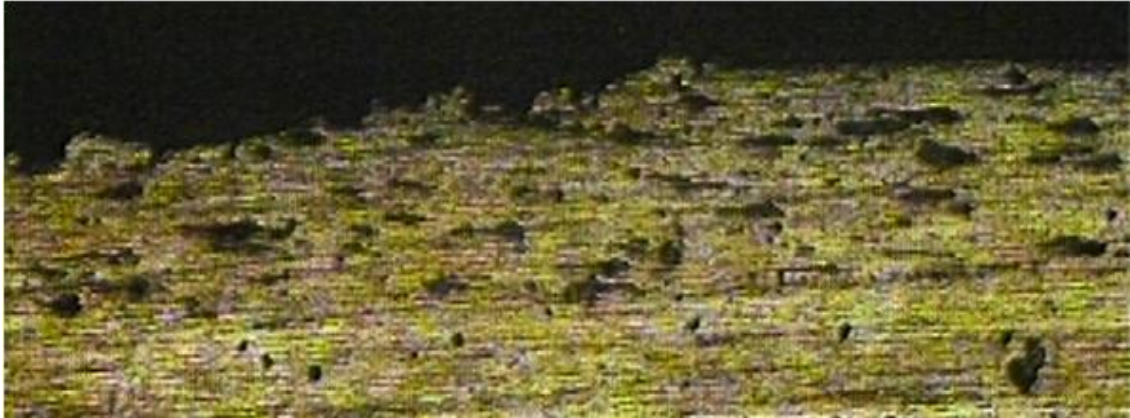


**Figure 2.3-6: Impacted surface layer after two electrical arcs (25x)**

From Figure 2.3-6 & Figure 2.3-7 showing the cuts of the moving contact at the anode behaviour after two and three electrical arcs, we can still observe cadmium oxide clusters of important size in comparison to their initial one, and we can see that the silver underneath layer thickness has been reduced.

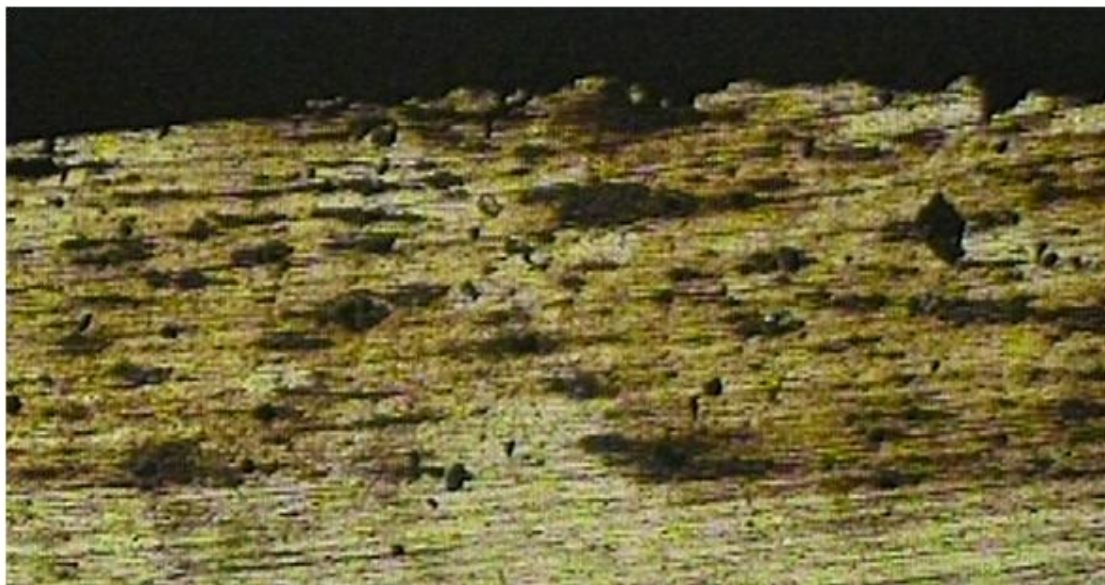


**Figure 2.3-7: Impacted surface layer after three electrical arcs (25x)**

After ten and one hundred electrical arcs, the sections look completely different (see Figure 2.3-8 & Figure 2.3-9).

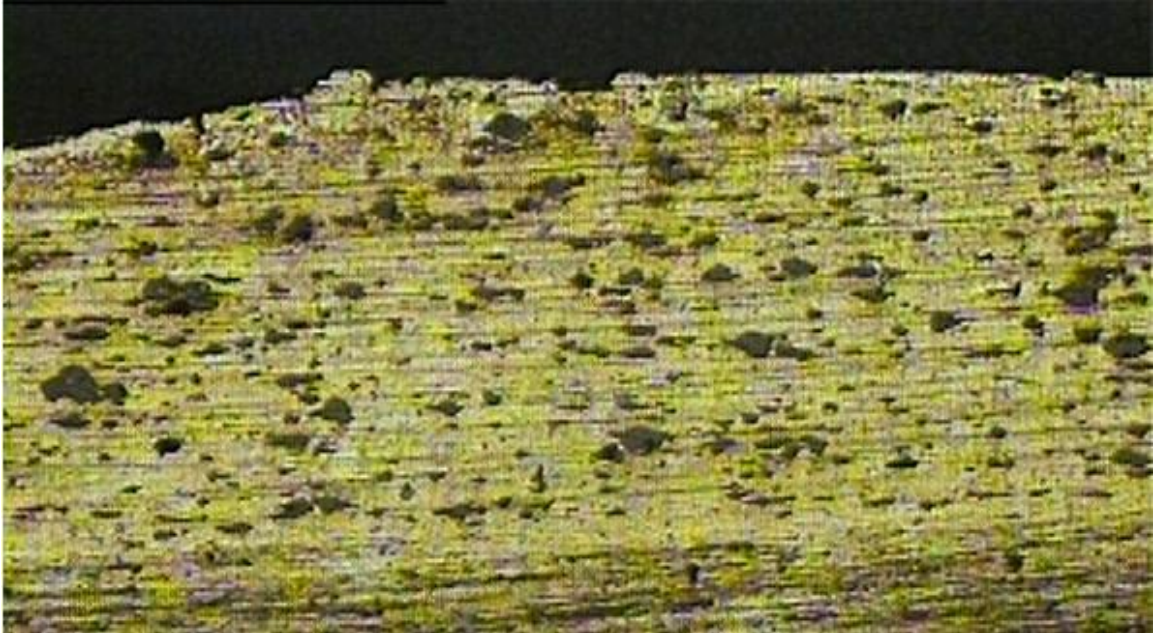


**Figure 2.3-8: Impacted surface layer after ten electrical arcs (25x)**

Actually, what we observe after ten electrical arcs is many more cadmium oxide clusters of smaller size well and finely distributed within the layer. Besides, it is of interest that the thickness of this impacted layer has increased.

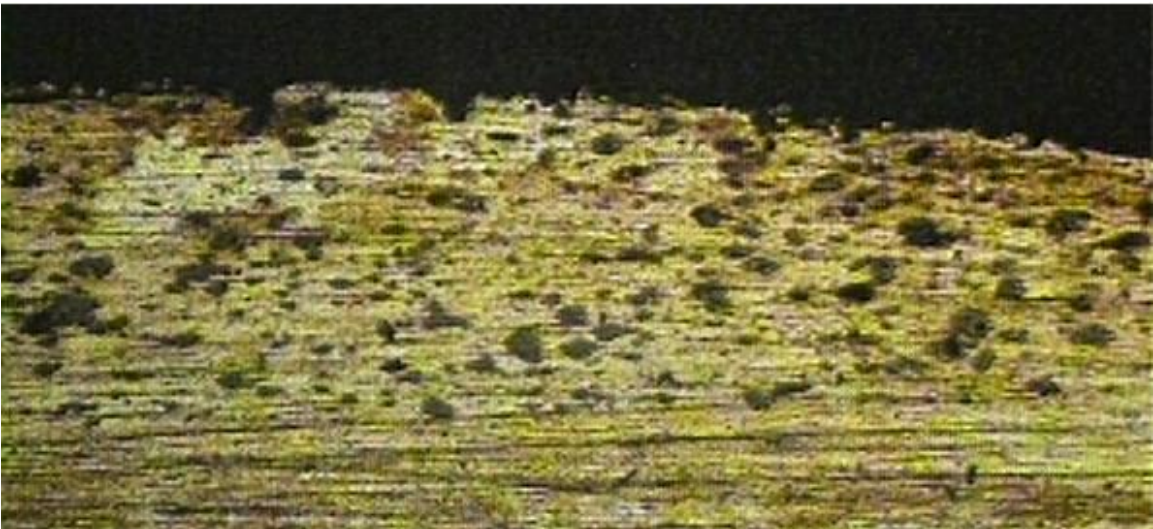


**Figure 2.3-9: Impacted surface layer after one hundred electrical arcs (25x)**



The section after one hundred electrical arcs confirms the trend of having, within the impacted layer, finely distributed smaller cadmium oxide clusters in comparison to their size after a few electrical arcs. Moreover, the thickness of the impacted layer stabilized.

### **2.3.2. Discussion**

Layer dynamics directly impact surface dynamics and vice versa. The layer is the source from which the contact material will get its new “skin”, its new contact surface. In other words, given that after each electrical arc we have a new contact surface, a good understanding of how things change within the impacted layer enables us to better understand how things will change at the contact surface and thus, how contact properties will evolve with the number of arcs.

With the increasing number of electrical arcs, we have noticed some changes in terms of size and distribution of the cadmium oxide clusters within the impacted layer. These can be thought of as manifestations of the two regimes we defined to describe surface dynamics in the former section.

During the transient state corresponding to the first few electrical arcs, cadmium oxide clusters and particles, under electromagnetic forces induced by the arc, agglomerate to form bigger clusters and particles. Within the molten bath, these clusters, under gravity effects, go up to the contact surface; since silver density is about  $10.49 \text{ g/cm}^3$  and cadmium oxide density is about  $7.28 \text{ g/cm}^3$ . This last move of oxides contributes to the renewal of the contact surface. At the same time, the volume of the contact material impacted by the electrical arcs increases since the border between the silver underlay and the contact material layer keeps moving down with the number of

arcs up to reach a steady position corresponding to the end of the transient state. This configuration with big oxide clusters scales down electrical and thermal conductivities through the contact material. Furthermore, that creates prominent areas of oxide-depleted metal at the new contact surface, which will reduce the viscosity of the molten bath and the anti-welding resistance of the contact.

This steady volume of impacted contact material reached signals the beginning of the quasi-steady state regime. It consists in damped oscillations of arc erosion properties around steady values directly resulting from changes in microstructure configurations. Indeed, after a certain number of electrical arcs, the size of the cadmium oxide clusters decreases and they get finely distributed. This change in size is mainly due to multiple collisions in between them, eased by their important size. This microstructure configuration gives a higher viscosity, which protects the contact material from splash erosion, and higher thermal and electrical conductivities. During this phase, the microstructure configuration of the layer will change back and forth around a steady configuration, by agglomeration and then collision of oxide clusters, inducing damped oscillation to arc erosion properties of the contact material.

These two regimes are perfectly illustrated by Figure 2.2-10 where we can see this fluctuation in the contact resistance value depending on the number of arcs.

## CHAPTER 3

### AgSnO<sub>2</sub> ARC EROSION BEHAVIOR

The same kind of arc erosion experiments as that realized and described in the former chapter have been conducted on the best potential candidate to the AgCdO substitution: AgSnO<sub>2</sub>, first in order to better understand its arc erosion behavior in service and second in order to make a comparison with AgCdO. As a consequence, in cooperation with our industrial partner Esterline Power Systems, five AgSnO<sub>2</sub> electrical contacts have been tested under exposure to different numbers of arcs in conditions similar to operating conditions in airplanes.

From a composition point of view, the five test contacts utilized are made of 88%Ag-12%SnO<sub>2</sub> (by weight) and were all prepared by powder metallurgical techniques. The process used was sintering. The five contacts have all been tested under the same operating conditions: Supply current of 400 A, Circuit voltage of 28 V DC, Ambient: air, room temperature. The first sample has undergone one “half-cycle” (only one break operation); the second one, two; the third one, three; the fourth one, ten and finally the fifth one, a hundred half-cycles. For every arc discharge, the contact resistance was measured.

The same analysis scheme has been used in order to first study AgSnO<sub>2</sub> surface dynamics, and then AgSnO<sub>2</sub> layer dynamics. Therefore, the main objective will still be to relate these changes of local surface and layer compositions and morphologies of the contact material induced by arcing to the evolution of its properties, such as the contact resistance, with an increasing number of electrical arcs. To this end, AgSnO<sub>2</sub> arc erosion behavior will be described through the same two stage model as the one defined in the previous chapter, with new definitions of the adjustment and of the quasi-steady states. In addition, a comparison between AgCdO and AgSnO<sub>2</sub> arc erosion behaviors will be made.

### **3.1. AgSnO<sub>2</sub> Surface Dynamics**

This section is focused on the study of the evolution of the contact surface with the number of electrical arcs under the operating conditions above mentioned. The following pictures correspond to the anode behavior on the moving electrode after a certain number of electrical arcs.

#### **3.1.1. Experimental results**

The same methodology that was used for AgCdO surface dynamics analysis has been applied for AgSnO<sub>2</sub> samples analysis. Therefore, for each of the five samples, EDS has first been used on the whole arc impacted area of the anode behavior of the moving electrode in order to identify representative and characteristic microstructures and chemical compositions. The results of this scan on the first sample, i.e. after one electrical arc, can be seen in Figure 3.1-1.

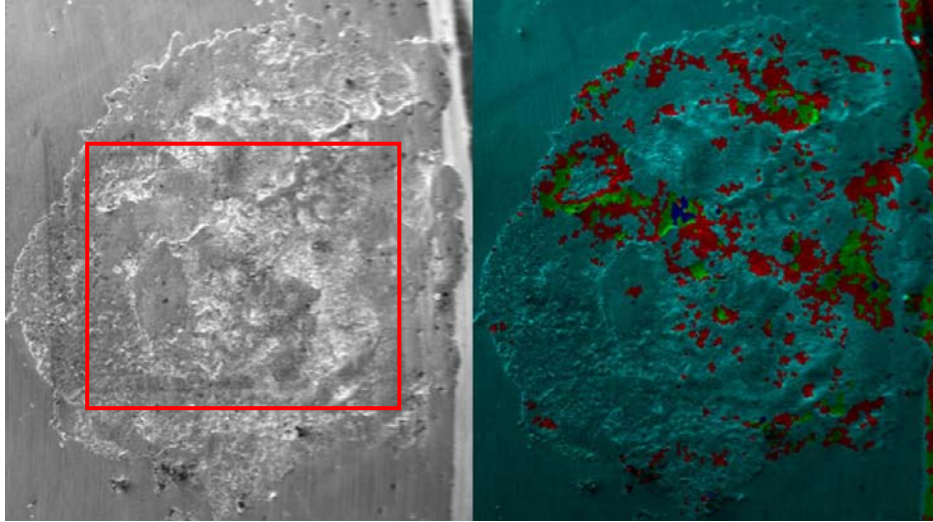


**Figure 3.1-1: EDS mapping of the crater after one electrical arc (x80) – Anode**

Based on this EDS mapping of the crater, where each color corresponds to a certain material composition, a representative part of this impacted surface (Red frame on Figure 3.1-2) gathering all the different compositions has been selected for zones analysis.

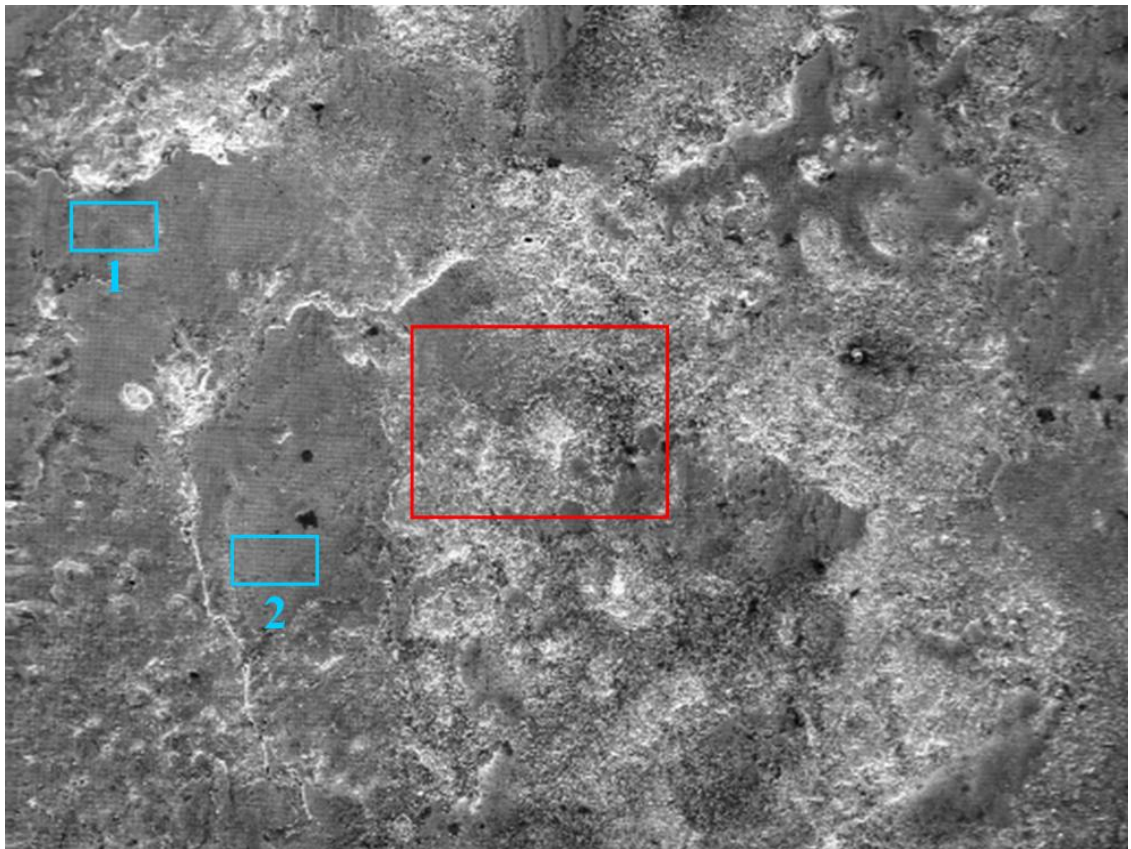


**Figure 3.1-2: Close-up of the red frame (Figure 3.1-1) (x200) – Anode**

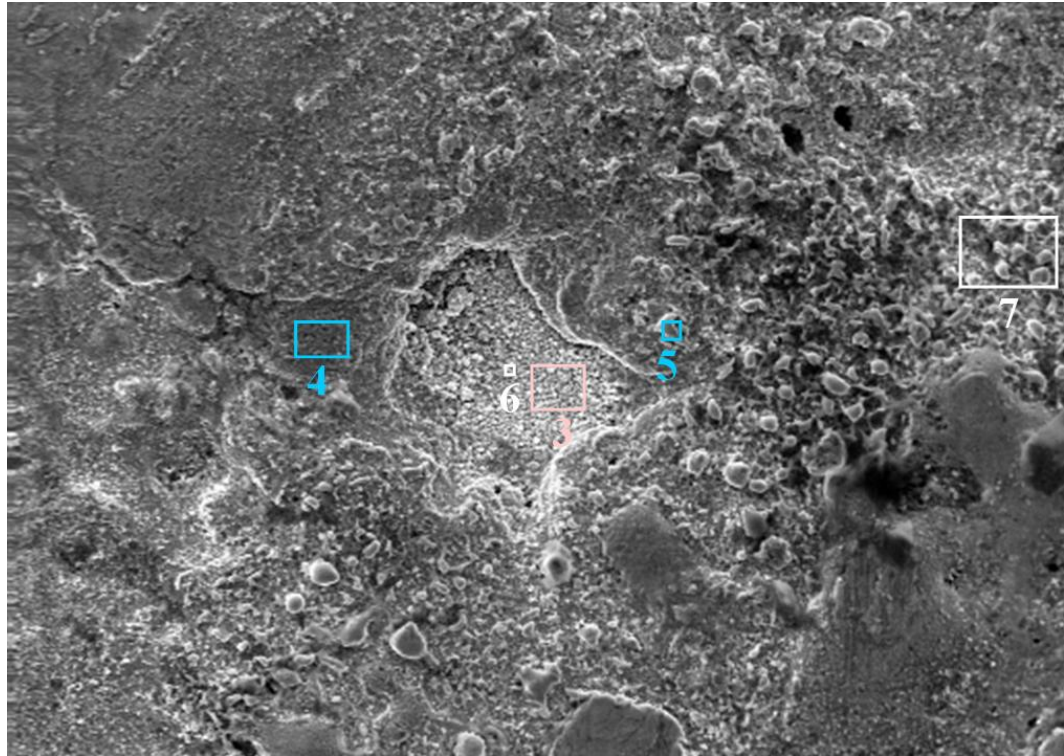


Figure 3.1-3: Close-up of the red frame (Figure 3.1-2) (x1000) – Anode

The chemical compositions of the seven zones depicted in Figure 3.1-2 & Figure 3.1-3 have been listed in Table 3.1-1 below.

Table 3.1-1: Chemical composition of the different zones relative to Figure 3.1-2 & Figure 3.1-3

Zone	Composition (% weight)	
	Ag	Sn
1	98	2
2	97	3
3	65	35
4	94	6
5	96	4
6	85	15
7	88	12

These zones can then be grouped by similarities in morphology and in chemical composition and can be sorted into 3 groups:

- Group I: Zones 1, 2, 4, 5, corresponding either to silver droplets ejected by splash erosion and redeposited on the contact surface (Zone 5) or to resolidified parts of the silver molten bath (Zones 1 & 2) or to a part of the granules cavity surrounding (Zone 4). They all have high silver ratio in composition (above 94%).

- Group II: Zone 3, corresponding to a part of the granules cavity with spherules and a high tin ratio in composition.

- Group III: Zone 6, 7, corresponding to ejected silver droplets redeposited on high tin ratio composition parts of the crater; explaining a composition close to the original one.

What will change with the number of arcs is the proportion of impacted areas belonging to each of these three groups, directly depending on surface dynamics.

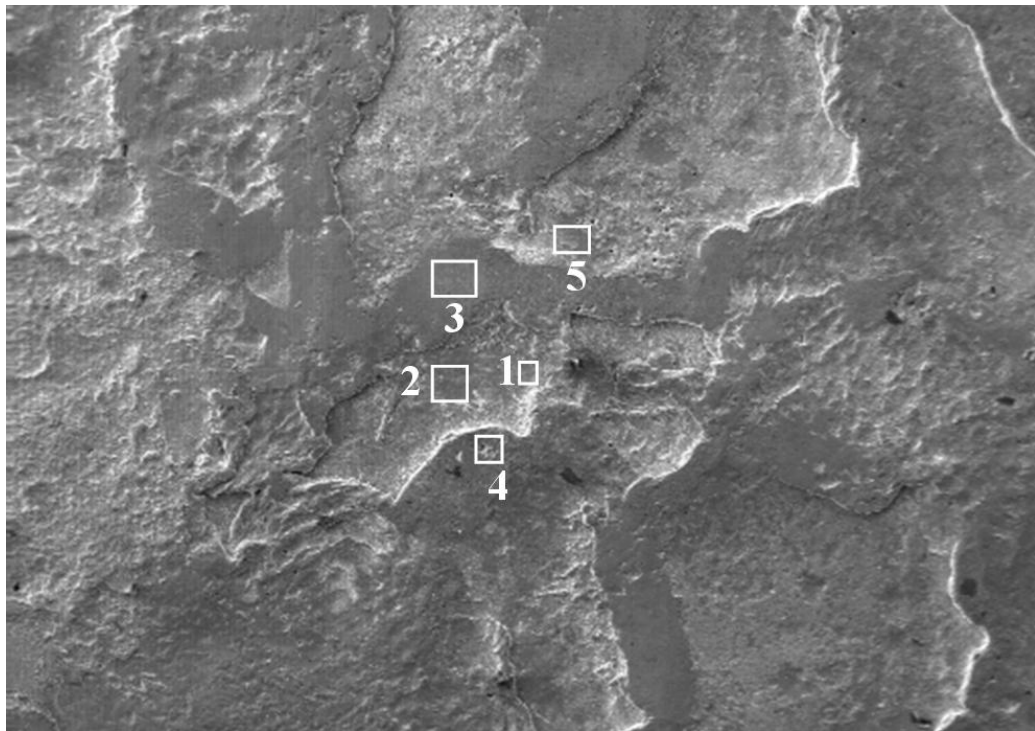


**Figure 3.1-4: SEM picture of the impacted area after two electrical arcs (x200) – Anode**



**Table 3.1-2: Chemical composition of the different zones relative to Figure 3.1-4**

	Composition (% weight)	
Zone	Ag	Sn
1	33	67
2	76	24
3	88	12
4	79	21
5	70	30

The morphology of the impacted surface after two electrical arcs (See Figure 3.1-4) looks less rough than after one and makes a larger smooth surface appear due to the solidification of the molten bath. It can clearly be observed that most of the tin oxide spherule cavities (Zones 1 & 5) have been filled up or covered by the molten bath, increasing this way the overall tin ratio at the contact surface (Zones 2 & 3). At last, Zone 4 looks like a redeposited droplet of tin oxide granules covered by molten silver.

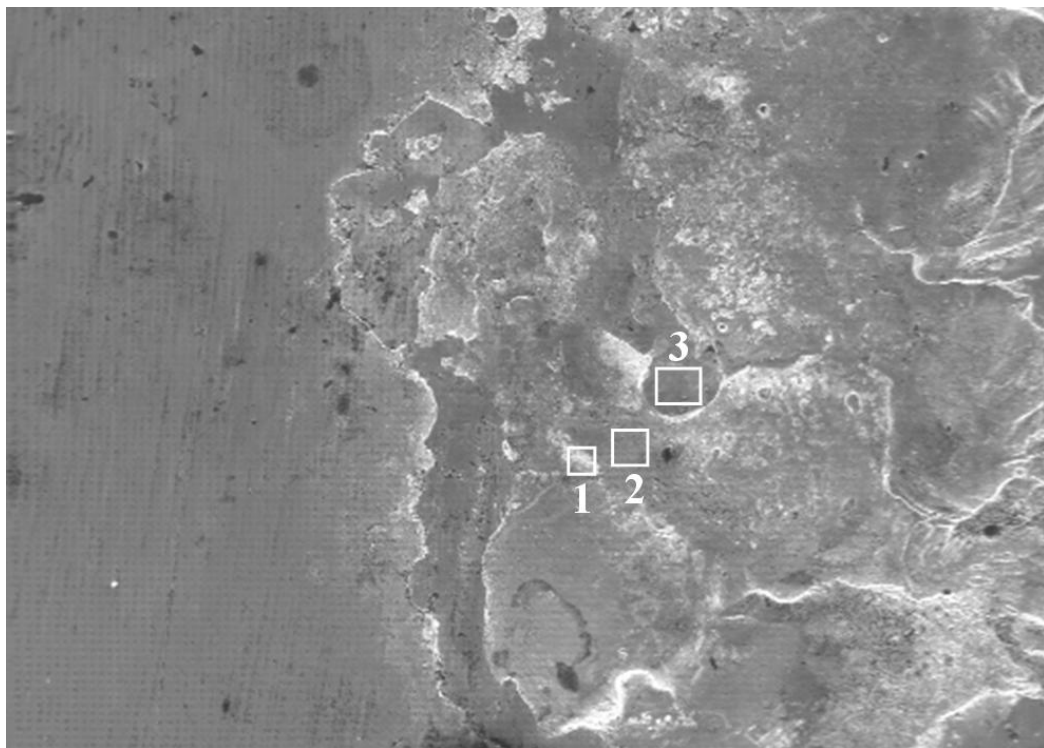


**Figure 3.1-5: SEM picture of the impacted area after three electrical arcs (x200) – Anode**



**Table 3.1-3: Chemical composition of the different zones relative to Figure 3.1-5**

	Composition (% weight)	
Zone	Ag	Sn
1	40	60
2	47	53
3	91	9

After three electrical arcs, the impacted surface (Figure 3.1-5) looks even smoother than after two. In addition, the different waves of solidification can clearly be seen. This is illustrated by Zones 1, 2, & 3 where Zone 1 corresponds to a cavity having plenty of granules whose composition is as expected mainly of tin oxide, and Zones 2 & 3, respectively depict the first and second wave of molten bath solidification.

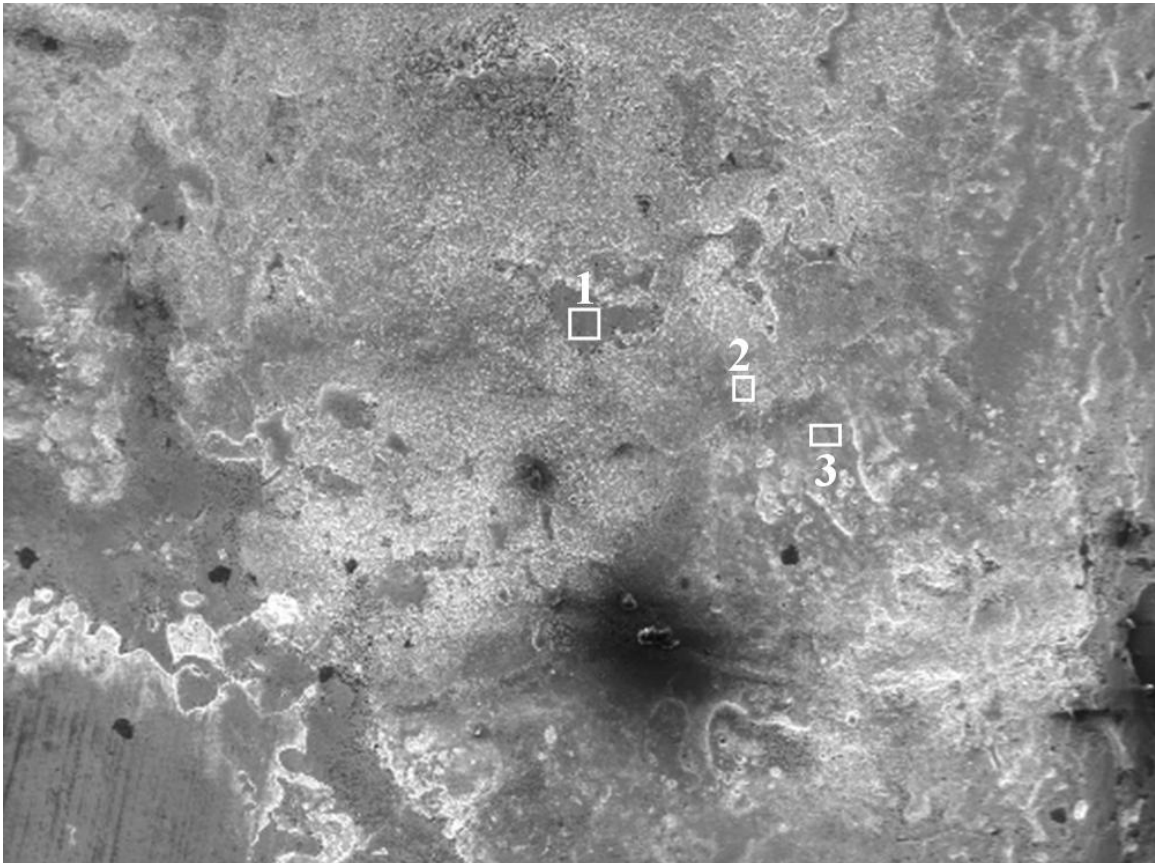


**Figure 3.1-6: SEM picture of the impacted area after ten electrical arcs (x200) – Anode**

**Table 3.1-4: Chemical composition of the different zones relative to Figure 3.1-6**

	Composition (% weight)	
Zone	Ag	Sn
1	96	4
2	52	48
3	72	28

In comparison to the former samples, an important roughness of the impacted surfaces can be observed after ten and one hundred electrical arcs (See Figure 3.1-6 & Figure 3.1-7), which means that most of these two impacted areas have a high tin oxide ratio in composition, since granules have not been fully covered. This is perfectly demonstrated by Zones 2 & 3 from Table 3.1-4 which correspond to two different levels of covering of tin oxide granules. Zone 1 is another consequence of splash erosion of silver droplets.

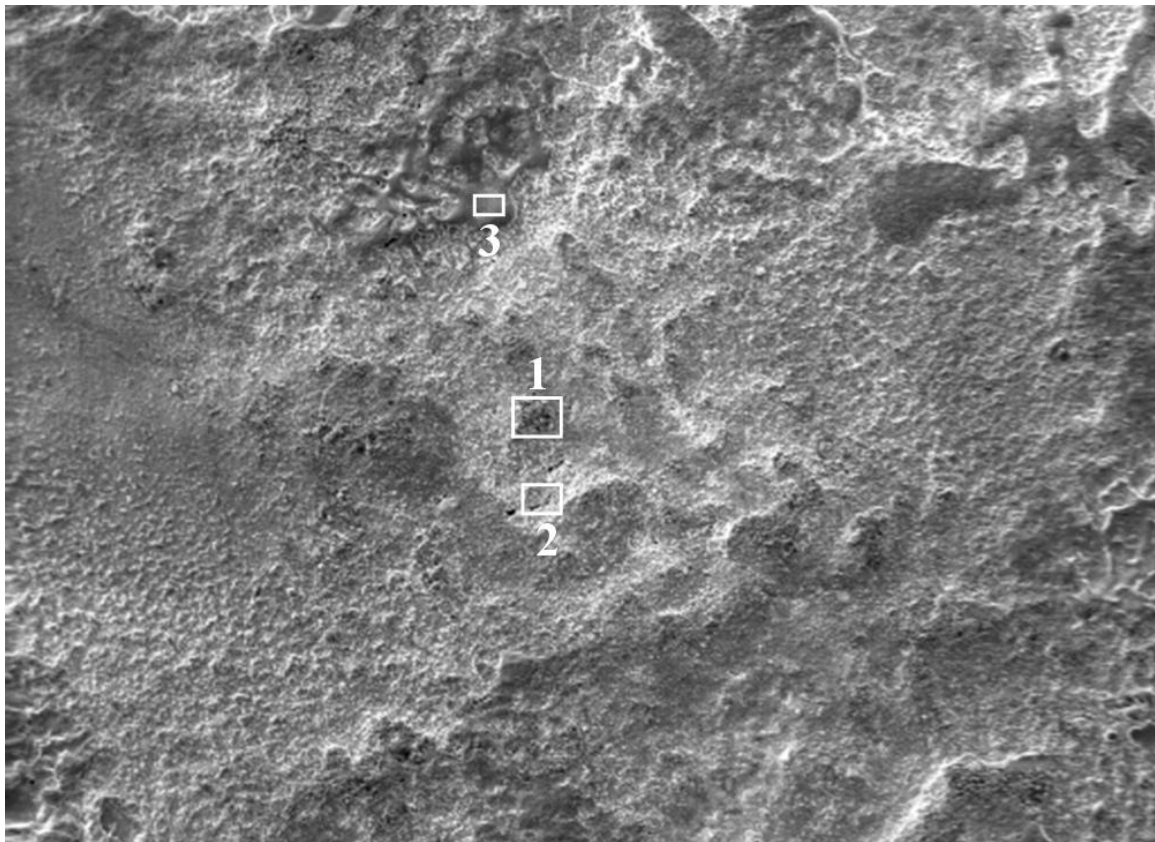


**Figure 3.1-7: SEM picture of the impacted area after one hundred electrical arcs (x400) – Anode**

**Table 3.1-5: Chemical composition of the different zones relative to Figure 3.1-7**

	Composition (% weight)	
Zone	Ag	Sn
1	76	24
2	60	40
3	98	2

This high density of tin oxide granules, noticed from a morphological point of view at the contact surface of the impacted area after one hundred electrical arcs (See Table 3.1-5), is confirmed by the chemical compositions of Zones 1 & 2. In Zone 3 silver droplets resulting from splash erosion can also be seen.

### **3.1.2. Discussion**

The same two regimes defined earlier to describe the arc erosion behaviour of AgCdO can now be applied to explain AgSnO<sub>2</sub> surface dynamics. These two states can be specified by relating the observed changes in morphology and in composition as a function of the number of electrical arcs to the contact resistance measurements taken during the arcing experiments (See Figure 3.1-8).

The first few arcs, where we can notice a slow increase of the contact resistance value, would correspond to the transient state. From the former observations on the AgSnO<sub>2</sub> samples, this increase can be explained by the fact that the contact surface roughness has grown from the beginning with the number of electrical arcs. From a chemical composition point of view, this increase in the density of granules at the contact surface means a higher tin oxide composition at the electrode surface, which results in lowering the electrical conductivity of the contact material.

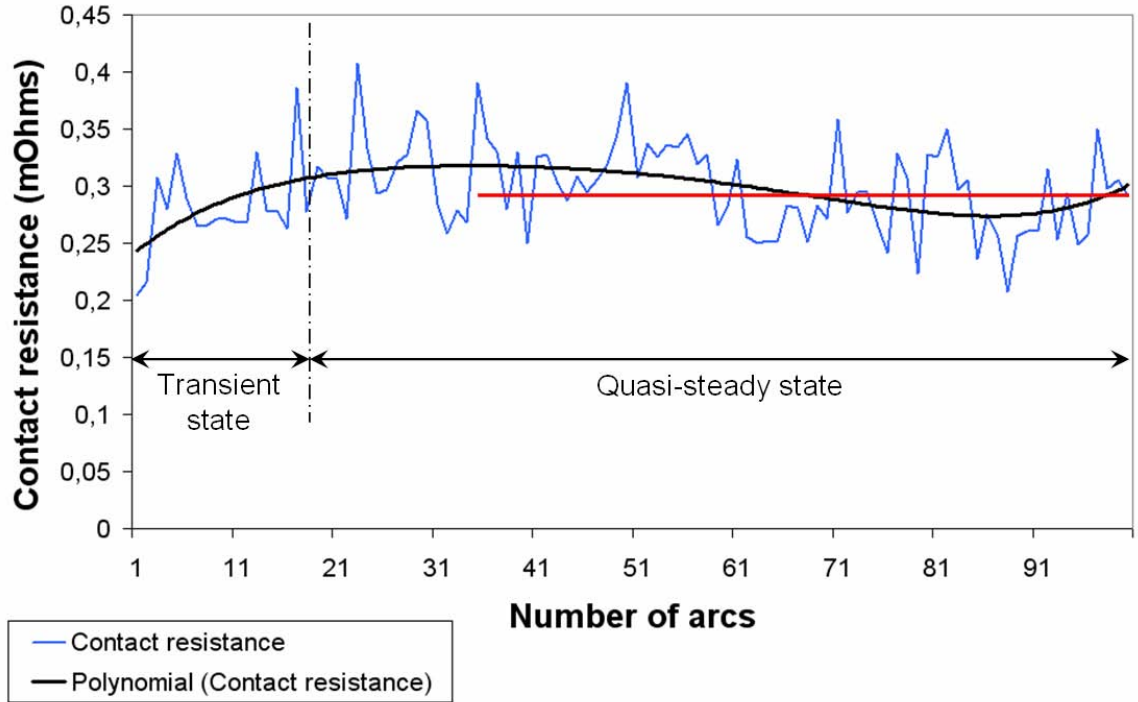


**Figure 3.1-8: Evolution of the  $\text{AgSnO}_2$  contact resistance with the number of arc (Data shown is the average of 5 sets of experiments)**

With an increasing number of arcs, a quasi-steady state is reached, where the contact resistance value follows dampened oscillations around a nominal value. This nominal value corresponds to a stable configuration from a morphological and a composition point of view of the electrode surface that the system tends to reach.

### 3.2. $\text{AgSnO}_2$ Layer Dynamics

This section is devoted to the study of the contact material layer dynamics of the same samples above analyzed. The following pictures also correspond to the anode behavior on the moving electrode after a certain number of electrical arcs.



### 3.2.1. Experimental results

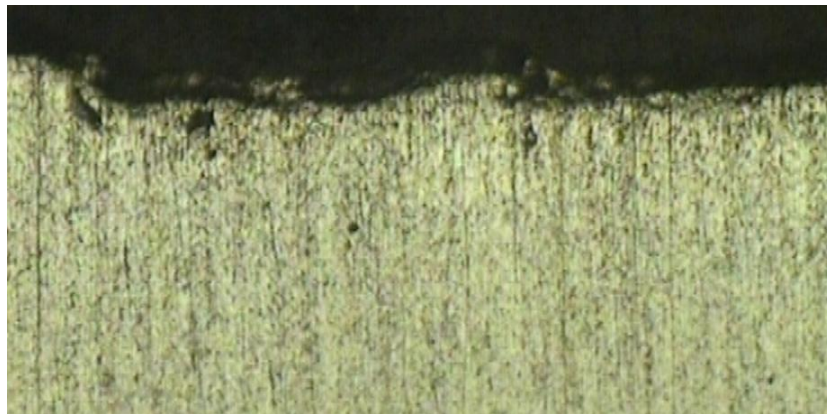
The same methodology as the one applied to study AgCdO layer dynamics has been used. Therefore, all the samples have been cut after experiments according to a vertical plan located at 1 mm from their periphery, polished and then analyzed

The initial configuration of tin oxide particles within the contact material layer before arcing can be seen in Figure 3.2-1.



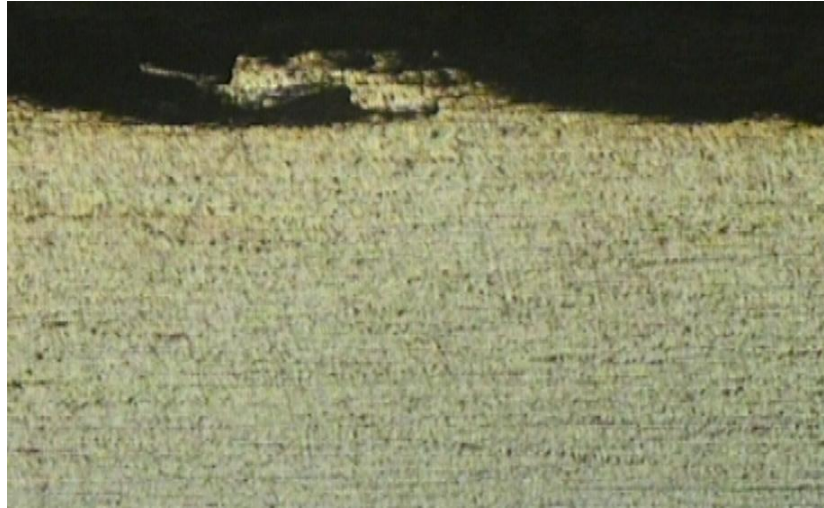
**Figure 3.2-1: Grading of AgSnO<sub>2</sub> 88/12**

The tin oxide particles are homogeneously and finely distributed within the layer. The AgSnO<sub>2</sub> sample having been subjected to one electrical arc is shown in Figure 3.2-2.



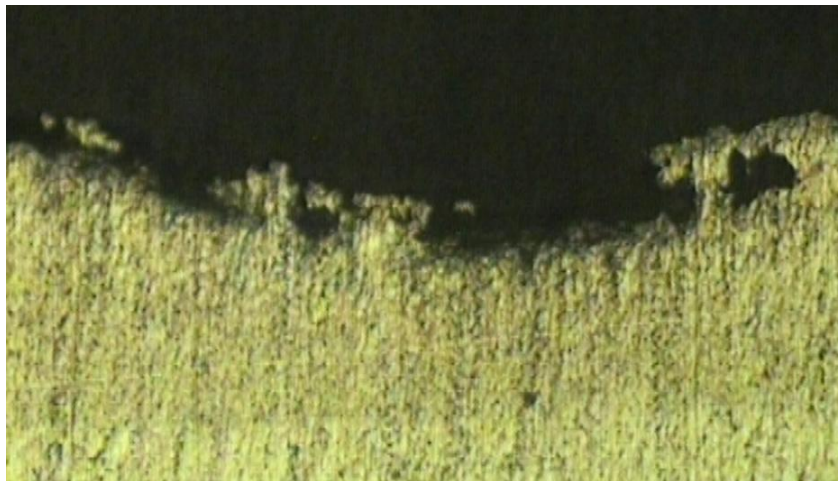
**Figure 3.2-2: Section of the anode after one electrical arc (x200)**

The formation of a few tin oxide clusters located close to the contact surface can then be observed.



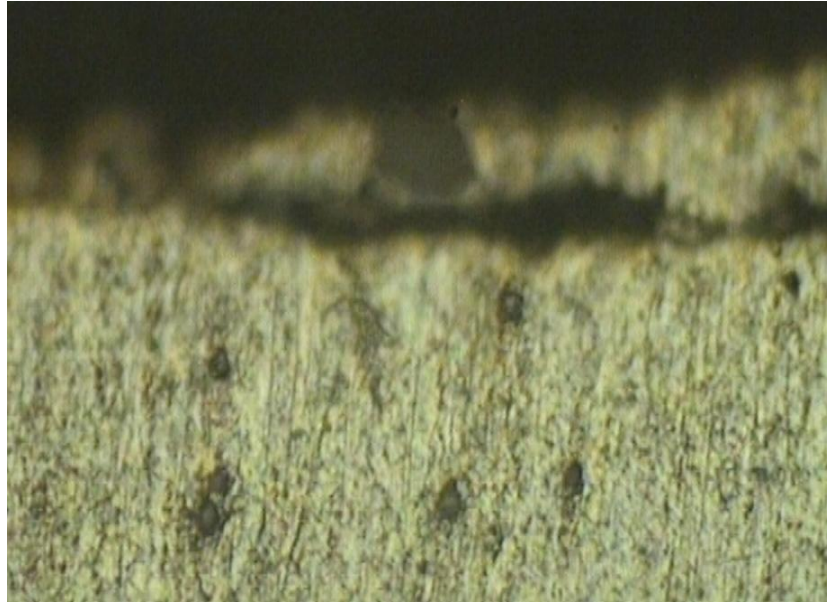
**Figure 3.2-3: Impacted surface layer after two electrical arcs (x100)**

Figure 3.2-3, depicting the impacted surface layer after two electrical arcs, shows a cavity of tin oxide granules having been covered upon solidification by the molten bath.



**Figure 3.2-4: Impacted surface layer after three electrical arcs (x200)**

Opened and enclosed cavities of tin oxide granules can be noticed in Figure 3.2-4, a picture representing the impacted surface layer after three electrical arcs.



**Figure 3.2-5: Impacted surface layer after ten electrical arcs (x500)**

Some bigger tin oxide particles and some clusters of tin oxide can be seen in the surrounding of the electrode surface having been subjected to ten arcs in Figure 3.2-5.

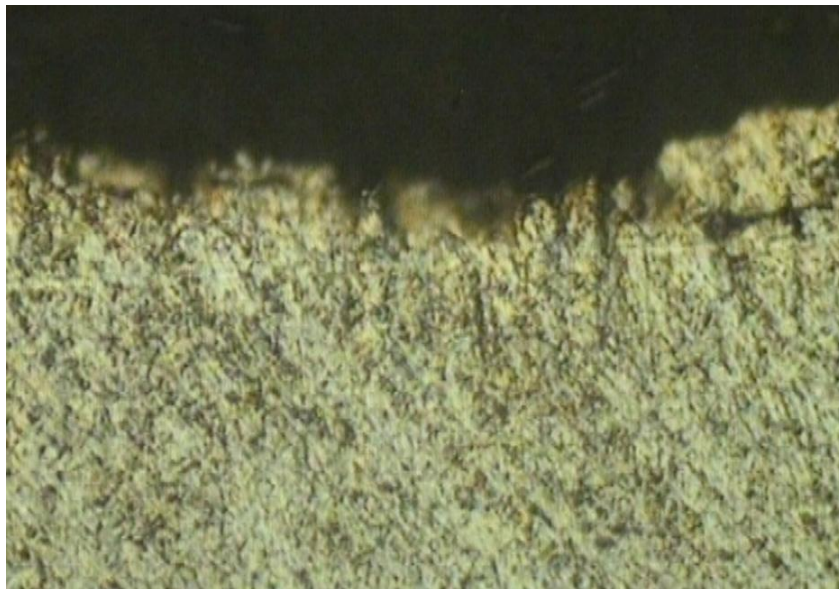


**Figure 3.2-6: Impacted surface layer after one hundred electrical arcs (x500)**

An important density of tin oxide particles in the vicinity of the contact surface can be observed in Figure 3.2-6, displaying a cut of the sample after one hundred electrical arcs. This accumulation of tin oxide particles in the surrounding of the electrode surface can be

explained by the fact that, under gravity effects, since silver density is about  $10.49 \text{ g/cm}^3$  and tin oxide density is about  $7.01 \text{ g/cm}^3$ , oxide particles move up within the molten bath to the contact surface.

### **3.2.2. Discussion**

The layer dynamics behaviour of  $\text{AgSnO}_2$  can be explained through its relation with the evolution of the contact resistance value with the number of arcs taken during these experiments (See Figure 3.1-8).

From the former observations on the cuts of  $\text{AgSnO}_2$  samples that were subjected to 1, 2, 3, 10, and 100 electrical arcs, the contact layer configuration has changed with the first few arcs. Indeed, the accumulation of tin oxide particles and the formation of tin oxide clusters in the immediate surrounding of the electrode surface have been observed, thus modifying the viscosity of the molten bath and its electrical and thermal conductivities. During this period called the transient state phase, this increase in viscosity limits material removal by splash erosion. In the same time, these decreases in thermal and electrical conductivities due to a higher density of tin oxide particles in the vicinity of the contact surface, prevent heat from well evacuating and raise the contact resistance value.

With an increasing number of arcs, due to collisions between tin oxide clusters and particles during movement induced by the electromagnetic agitation of the molten bath, the size and distribution of these tin oxide particles will oscillate around a stable configuration. As a consequence, during this period called the quasi-steady state phase,



material properties such as the viscosity and the contact resistance will follow dampened oscillations around nominal values.

### **3.3. Conclusion and comparison with AgCdO**

Both AgCdO and AgSnO<sub>2</sub> arc erosion behaviours have been described and explained by a model consisting of two regimes:

- A transient state phase corresponding to the first few electrical arcs where for both contact materials, the formation of oxide clusters at and in the immediate surrounding of the contact surface has been noticed. These clusters are bigger and higher in density, as far as AgCdO is concerned. This accumulation of oxide particles close to the electrode surface results in some changes of the contact material properties, and thus will modify the contact material response to arcing. This notably damages its electrical and thermal properties since it induces an increase of the contact resistance due to the fall in the value of the electrical conductivity, and it also causes a fall in the value of the thermal conductivity. However, the arc erosion properties are enhanced since this accumulation of oxide particles raises the viscosity of the molten bath, and therefore reduces material removal by splash erosion.
- A quasi-steady state phase corresponding for both materials to changes of the distribution and the size of oxide particles within the contact layer, of the morphology and the composition of the contact surface, back and forth around a stable configuration. These modifications in the distribution and size of oxide particles result from collisions between oxide clusters, in motion because of the electromagnetic agitation of the molten bath induced by the electrical arc, and also because of the difference between the value of

the oxides density and the value of the silver density. As a consequence of these changes, material properties will follow dampened oscillations around a nominal value, which corresponds to a stable configuration from a morphological, composition, distribution and size point of view of the contact material that the system tends to reach.

The following plot (See Figure 3.3-1), showing the evolution of the AgCdO and AgSnO<sub>2</sub> contact resistances with the number of arcs, illustrates the two regimes model.

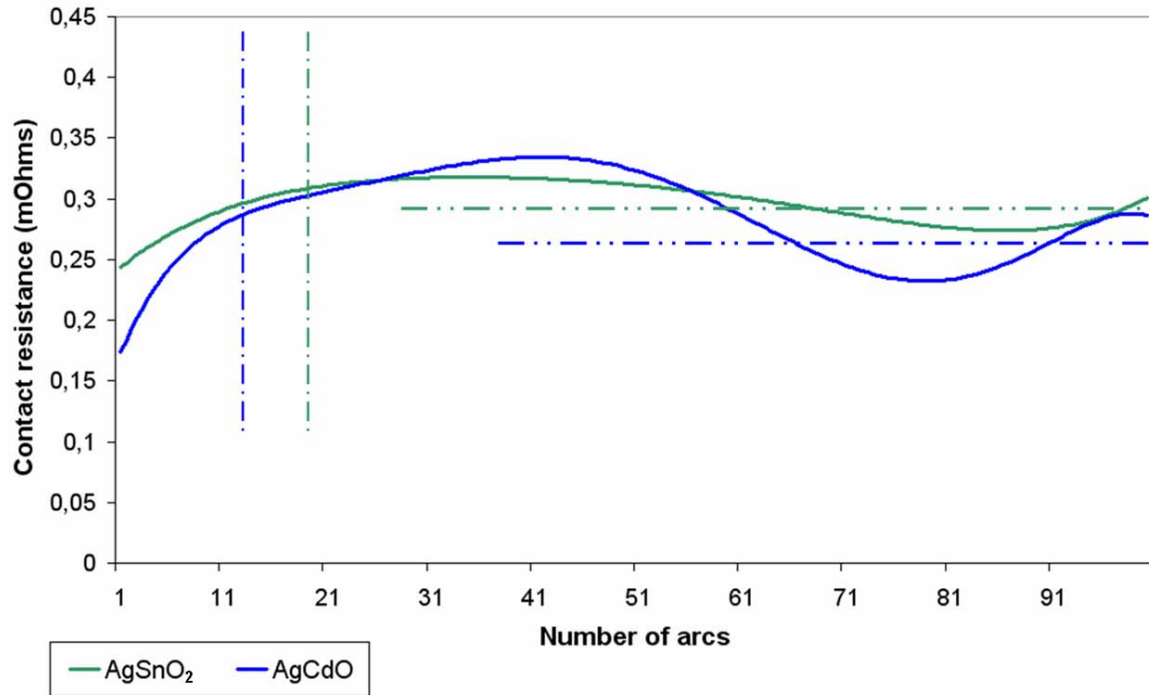


**Figure 3.3-1: Evolution of the AgCdO and AgSnO<sub>2</sub> contact resistances with the number of arc**

Some differences concerning AgCdO and AgSnO<sub>2</sub> behaviours can be noticed on Figure 3.3-1. First, the AgCdO transient state phase is shorter than the AgSnO<sub>2</sub> one. Second, AgCdO has a larger slope during this transient state phase than AgSnO<sub>2</sub>. And finally, the nominal value of the AgCdO contact resistance is lower than that of AgSnO<sub>2</sub>.

Several factors can explain these differences. First, the initial configuration of these two contact materials was not the same. Indeed, AgCdO samples were made of

AgCdO 90/10 with big cadmium oxide particles whereas AgSnO<sub>2</sub> samples were made of AgSnO<sub>2</sub> 88/12 with small tin oxide particles finely distributed within the layer. Second, the thermal properties of these two contact materials have some major differences.

**Table 3.3-1: Thermal properties of the major constituents in AgCdO and AgSnO<sub>2</sub>**

<b>Material</b>	<b>Decomposition Temperature (°C)</b>	<b>Melting Temperature (°C)</b>	<b>Boiling Temperature (°C)</b>	<b>Density (kg/m<sup>3</sup>)</b>
<b>Ag</b>	--	962	2162	10490
<b>Sn</b>	--	232	2602	7360
<b>SnO<sub>2</sub></b>	1625	--	2250	7010
<b>Cd</b>	--	321	765	8650
<b>CdO</b>	1000	--	1385	7280

As can be seen in Table 3.3-1, the decomposition temperature of CdO is close to the melting temperature of Ag whereas the decomposition temperature of SnO<sub>2</sub> is much larger. Moreover, the boiling temperature of Cd is even smaller than the melting temperature of Ag, whereas the boiling temperature of Sn is larger than the boiling temperature of Ag.

These differences in thermal properties can also explain why there are more CdO clusters than SnO<sub>2</sub> clusters within the layer and at the contact surface and why the AgSnO<sub>2</sub> contact surface is rougher than the AgCdO one.

To conclude, the surface and layer dynamics of AgSnO<sub>2</sub> and of AgCdO are based on the same model: the transient state and quasi-steady state model. However, the differences concerning their arc erosion behaviour mainly lie in the differences in their thermal properties, and more specifically in the thermal properties of their oxides. Therefore, CdO particles' behaviour within the AgCdO alloy while arcing is, as expected,

the key to understand what makes it an outstanding contact material. The next step is now to develop a macroscopic arc erosion model which describes the whole breaking operation. This will help us to simulate the arc erosion behaviour of the power switching devices used by Esterline Power Systems, and thus to get the total amount of material removed due to the electrical arc after one contact opening

## **CHAPTER 4**

### **COMPLETE MACROSCOPIC ARC EROSION MODEL AND EXPERIMENTAL VALIDATION**

Electrical arc erosion plays a crucial role in the reliability and life of power switching devices. Depending on the contact material behavior in response to an electrical arc, surface damage can induce severe changes in contact material properties that will impact the power switching device's functioning. The arc erosion process mainly results from two modes: the vaporization of contact material under heat energy coming from the electrical arc and the ejection of molten metal droplets induced by driving forces such as electromagnetic force, and the Buoyancy and Marangoni effects [30-43]. Depending on the range of current under consideration, the contribution from each mode can change. Now that we have analyzed the specific arc erosion behaviors of AgCdO and AgSnO<sub>2</sub> through a series of experiments, the main objective is to develop a general macroscopic arc erosion model that best describes the whole breaking process of the electrical contacts tested in the previous chapters.

Different arc erosion models have been developed. Swingler and McBride's arc erosion model describes the electrical contact opening with the formation and the

extinction of the electrical arc, but this study has only regard for the vaporization part [44]. Ben Jemaa compared pure silver arc erosion experimental data to calculations of the evaporated mass resulting from finite element simulations [45]. However, these two models can only be valid for low current since the splash erosion contribution, not taken into account in any of these two models, grows with current intensity [1, 44, 46-49]. Wu's model [50], based on a kinetic energy approach, was the first to describe sputter erosion of electrical contact material and therefore, to simulate arc erosion at high currents. Nevertheless, this model completely disregarded the arc formation and extinction, and the vaporization part.

The purpose of this section is to present a complete macroscopic arc erosion model, taking into account the two arc erosion modes: vaporization and splash erosion, and consequently describing the arc erosion process during a breaking operation under DC conditions over a wider current range from the arc formation to its extinction. This model is based on the coupling of three different models. The first one corresponds to the arc energy transport model developed by McBride [44], and it is used to describe the electrical arc created during the contact opening. It notably allows us to get the energy brought by the electrical arc from one electrode to the other one at any time  $t$  of the breaking operation, and it drives the simulation time since the simulation stops whenever the arc extinguishes. The second one is a thermal model based on Fourier's law of conduction, and its main purpose is to give the temperature distribution within the electrode and at the contact surface in the vicinity of the electrical arc impact at any time  $t$  of the breaking process. Therefore, it provides the size of the molten pool (molten contact material) and the amount of material vaporized at any time  $t$  of the contacts

opening operation. Finally, the last one is a magneto-hydrodynamic model based on the mechanics of liquid jets and the theory developed by J. N. Anno in [51] to describe the case of a free, viscous inertial jet, and we have adapted it to the case of the formation of a molten metal jet subjected to forces induced by the electrical arc. Under certain critical conditions, this molten metal jet breaks up and forms molten metal droplets. The total amount of contact material removed by this ejection of droplets (Splash erosion) is then considered to be part of the material removed by arc erosion. These three models depend on each other since for each time step, outputs from one serve as inputs to another one. The main output of this complete macroscopic arc erosion model is to give the total amount of material removed from the impacted electrode after one breaking operation.

Furthermore, experiments on AgCdO power switching devices have been carried out under DC current and resistive load for five different current intensities: 200, 400, 600, 800 and 1000 A in order to test the arc erosion model at high current. In this objective, white light interferometry has been used to measure the total amount of material removed after each breaking operation. Finally, low current model results have been compared to McBride's AgCdO experimental data [44].

#### **4.1. Arc erosion model architecture**

This arc erosion model is based on the coupling of an arc energy transport model, a thermal model and a magneto-hydrodynamic model. It calculates the amount of contact material removed after one electrical arc corresponding to one breaking operation under DC conditions, assuming that all vaporized and ejected molten materials have been removed. Indeed, it does not take into account deposition mechanisms.

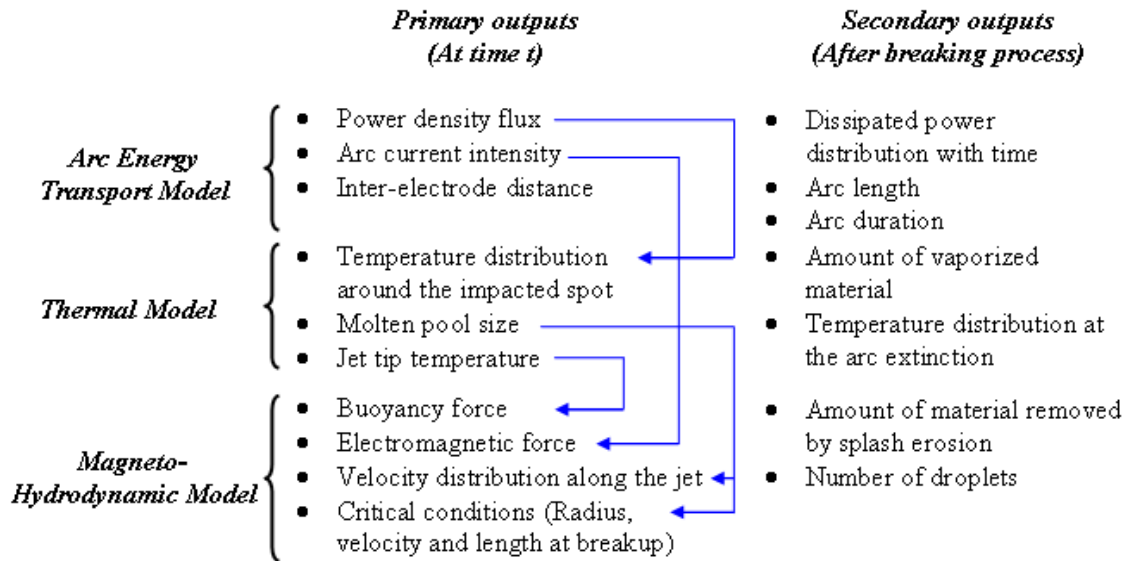


**Figure 4.1-1: Diagram of the models outputs and their coupling**

Figure 4.1-1 gathers the main interactions between the three models. It can be noticed that the evolution of the current intensity with time given by the arc energy transport model is used as input in the magneto hydrodynamic model to calculate the fluctuations with time of the electromagnetic force through the breaking process. In the same manner, the power density flux through the arc from the arc energy transport model is utilized as input in the thermal model in order to get the temperature distribution in the vicinity of the arc impacted point of the electrode at any time  $t$ . Likewise, the jet tip temperature and the molten pool size, derived at any time  $t$  from the temperature distribution given by the thermal model, are respectively used as inputs of the magneto-hydrodynamic model to calculate the buoyancy force and to get the velocity distribution along the jet and the critical conditions for this jet to break up at any time  $t$ . Those interactions and the coupling between the three models are explained in the forthcoming sections where the complete arc erosion model is detailed.



#### 4.1.1. Arc Energy Transport Model

The purpose of this model initially developed by Swingler and McBride [44] is to provide the amount of energy brought by the electrical arc to the electrode surface under study for each time  $t$  of the breaking process under DC conditions. It mainly depends on input parameters related to experimental conditions such as the current intensity, circuit voltage and opening velocity. The power flux density through the arc, the main output of this model, will be then used as input of the thermal model that is further detailed.

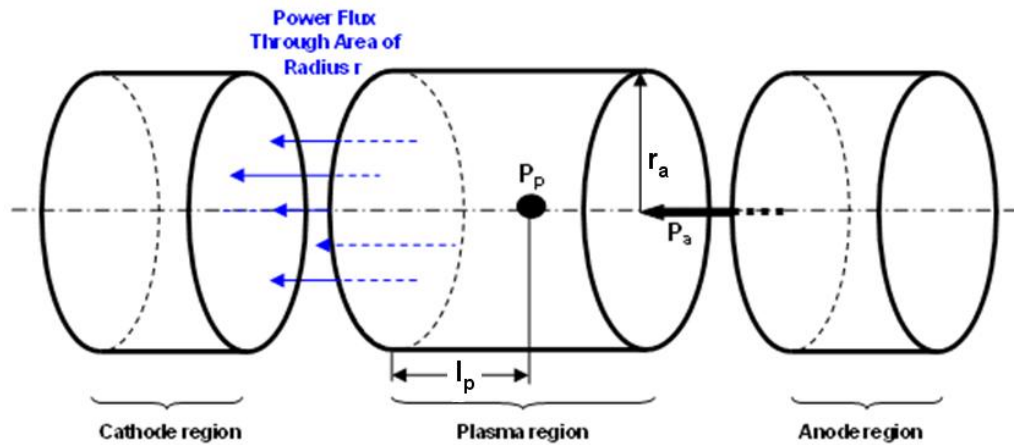


Figure 4.1-2: Power dissipation through plasma region

The arc energy transport model considers that the arc is divided into three regions (See Figure 4.1-2): the anode region, the plasma region and the cathode region. The power dissipation within each of these three regions is computed from the current through the region and the potential drop across it. Then, power dissipation through the arc, from region to region up to the contact surface, is calculated considering two ways of energy transport processes that encompass all the mechanisms involved at a microscopic scale in the energy transport process: radial and channel transport processes. Radial transport processes gather mechanisms which radiate energy equally in all directions such as

thermal energy from random bombardment of particles, radiation from de-excitation of particles, etc. Besides, channel transport processes account for mechanisms which transport energy (channel energy) toward the cathode or anode. In any one arc region, energy is channeled to neighboring regions by, for instance, positive ion or electron bombardment as they are accelerated through the electric field.

Consequently, the amount of energy available from any particular arc region in a given time  $\Delta t$  is equal to the energy generated in the region plus any energy transported from any neighboring regions by the two transport processes. The power flux density out of the plasma region transporting energy towards the cathode is then given by:

$$q_c = \frac{P_p + P_a}{\pi r_a^2} \left( \frac{k_1 r_a}{2\sqrt{r_a^2 + l_p^2}} + k_2 \right) \quad (4.1)$$

Where  $k_1$  is the proportion of energy radially dissipated

$k_2 = 50\%$  related to the channel transport process

$l_p$  is the distance between the point source and the plasma boundaries

$r_a$  is the arc radius to axis

$P_a$  is the power input from the anode region

$P_p$  is the power dissipated from the point source in the plasma region

Using another control term  $k_3$  instead of  $k_2$  in equation 4.1, the power flux density out of the plasma region transporting energy towards the anode can be found.

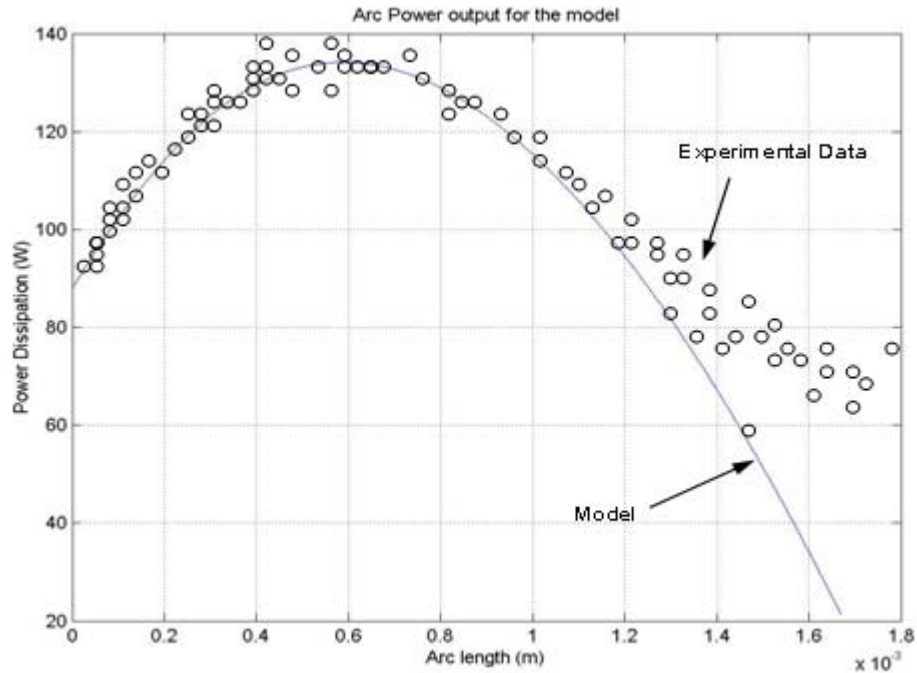


**Figure 4.1-3: Arc power output for I=9A**

Therefore, by assuming that only energy dissipated through the arc root is transported to the electrode surface and that all other energy generated by the arc is lost to the environment, the total power dissipated in the arc is used as an energy input for the thermal model. Model results of the total power dissipated in the arc for I=9A shown on Figure 4.1-3 show good agreement with experimental data [44].

#### **4.1.2. Thermal Model**

The purpose of this model is to describe the energy dissipation coming from the electrical arc through the electrode and to give at any time  $t$  of the breaking process the temperature distribution near the arc impact location. It consists of a transient axisymmetric thermal conduction model within the electrode, based on Fourier's law, whose

heat energy input is the power flux density output from the arc energy transport model acting at the center of the electrode. It can be seen on Figure 4.1-4.

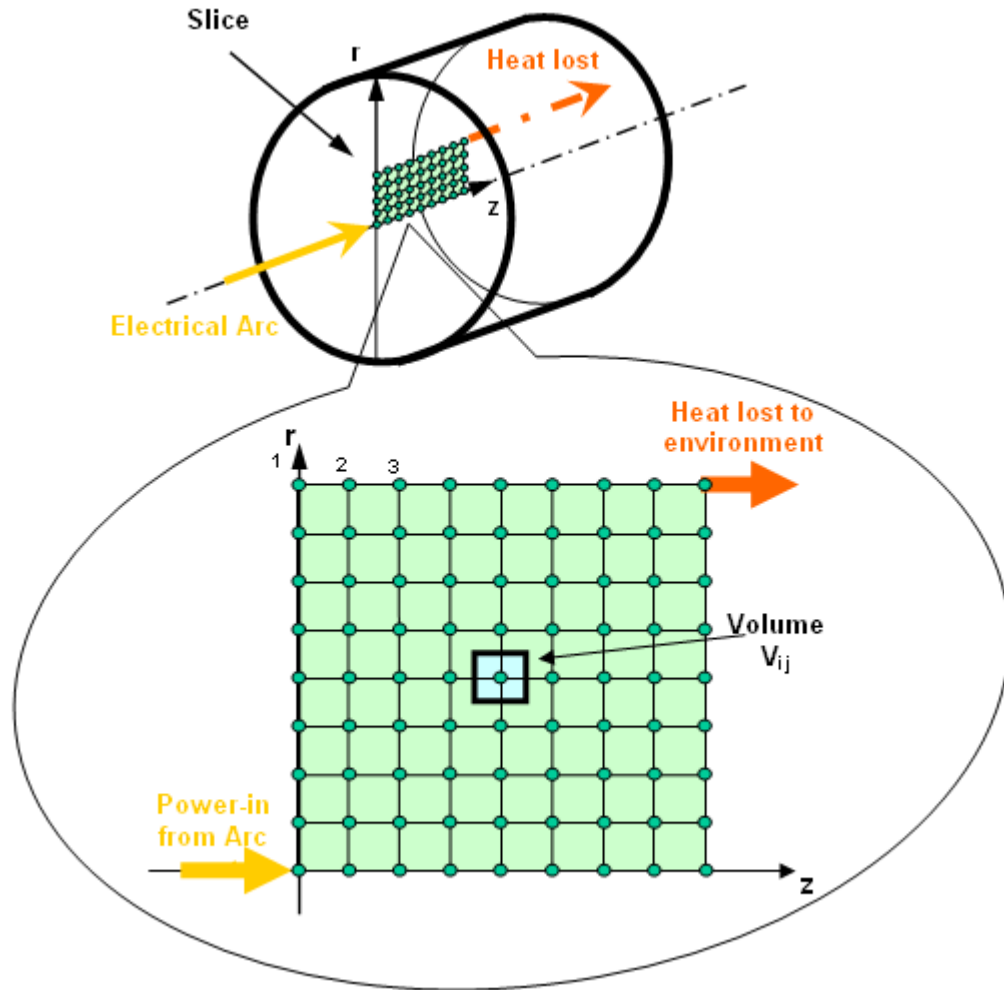


Figure 4.1-4: Meshing scheme

The finite differences method has been used to solve the heat equation in cylindrical coordinates on the meshing scheme presented on Figure 4.1-4. Taking into account phase changes, heat and temperature gradients can be computed by writing the thermal equilibrium equations for each control volume. These equations are derived from:

$$\frac{dE}{dt} = \nabla \cdot \vec{q} \quad (4.2)$$

Where  $\frac{dE}{dt}$  is the rate of change of the heat density at a given position

$\nabla \cdot \vec{q}$  is the heat flow divergence across that position

And Fourier's law of conduction:

$$\vec{q} = -k\nabla T \quad (4.3)$$

Where  $\nabla T$  is the temperature gradient

$k$  is the thermal conductivity

The energy density equations for each node of the meshing presented in Figure 4.1-4 are then derived. However, depending on the location of the node under consideration in the meshing, boundary conditions are different. Therefore, several cases have to be discussed.

#### 4.1.2.1. Case of interior nodes

This is the most general case where an interior nodal point  $i$  is located in the middle of the meshing (See Figure 4.1-5), i.e. this node does not belong to the outside square on Figure 4.1-4.

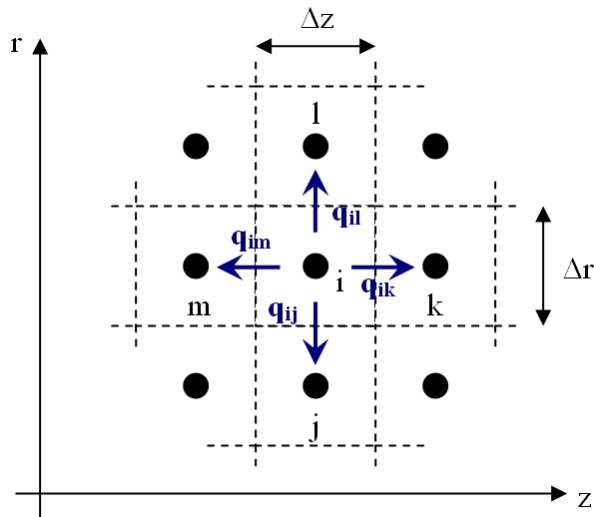


Figure 4.1-5: Heat transfer scheme for interior nodes

Node i is surrounded by nodal points j, k, l and m. The dashed boundary around node i is the cross-section of a ring around the z-axis. The radial position of node i is  $r_i$ , the thickness of the ring in the r-direction is  $\Delta r$  and the height of the ring in the z-direction is  $\Delta z$ . The areas of the side surfaces of the ring are given by:

$$A_{ik} = A_{im} = \pi \left[ r_i + \frac{\Delta r}{2} \right]^2 - \pi \left[ r_i - \frac{\Delta r}{2} \right]^2 = 2\pi r_i \Delta r = 2\pi j \Delta r^2 \quad (4.4)$$

The volume  $V_i$  of the ring is the product of the area of the base times the height of the ring as given by:

$$V_i = A_{im} \Delta z = 2\pi r_i \Delta r \Delta z = 2\pi j \Delta r^2 \Delta z \quad (4.5)$$

An energy balance for system i is given by:

$$0 = V_i \frac{\Delta E_i}{\Delta t} + q_{ij} + q_{ik} + q_{il} + q_{im} \quad (4.6)$$

The axial conduction terms  $q_{im}$  and  $q_{ik}$  are given by:

$$q_{im} = \frac{kA_{im}}{\Delta z} T_i - T_m \quad \& \quad q_{ik} = \frac{kA_{ik}}{\Delta z} T_i - T_k \quad (4.7)$$

The radial conduction terms  $q_{ij}$  and  $q_{il}$  are obtained from the analysis of steady-state one-dimensional conduction in a thick-walled cylinder. The heat-transfer rate  $q_{ij}$  through a cylinder of inside radius  $r_j$ , outside radius  $r_i$ , inside temperature  $T_j$ , outside temperature  $T_i$  and length  $\Delta z$  is given by

$$q_{ij} = \frac{T_i - T_j}{\frac{1}{2\pi k \Delta z} \ln \left( \frac{r_i}{r_j} \right)} = - \frac{2\pi k \Delta z}{\ln \left( 1 - \frac{1}{j} \right)} T_i - T_j \quad (4.8)$$

Similarly,

$$q_{il} = \frac{T_i - T_l}{\frac{1}{2\pi k \Delta z} \ln\left(\frac{r_i}{r_l}\right)} = \frac{2\pi k \Delta z}{\ln\left(1 + \frac{1}{j}\right)} T_i - T_l \quad (4.9)$$

Substituting the four rate equations into the energy balance gives

$$0 = V_i \frac{\Delta E_i}{\Delta t} + \frac{2\pi k \Delta z}{\ln\left(1 + \frac{1}{j}\right)} T_i - T_l - \frac{2\pi k \Delta z}{\ln\left(1 - \frac{1}{j}\right)} T_i - T_j + \frac{k A_{ik}}{\Delta z} T_i - T_k + \frac{k A_{im}}{\Delta z} T_i - T_m \quad (4.10)$$

Consequently, the change in the amount of energy density on system i in a time step  $\Delta t$  is given by

$$\Delta E_i = \frac{k \Delta t}{\Delta z^2 \Delta r^2} \left[ \left( \frac{\Delta z^2}{j} \left( \frac{1}{\ln\left(1 - \frac{1}{j}\right)} - \frac{1}{\ln\left(1 + \frac{1}{j}\right)} \right) - 2 \Delta r^2 \right) T_i + \frac{\Delta z^2}{j \ln\left(1 + \frac{1}{j}\right)} T_l - \frac{\Delta z^2}{j \ln\left(1 - \frac{1}{j}\right)} T_j + \Delta r^2 T_k + \Delta r^2 T_m \right] \quad (4.11)$$

#### 4.1.2.2. Case of the impacted element

This node i corresponds to the arc-impacted point of the electrode located at  $r=0$  and  $z=0$  in the meshing presented in Figure 4.1-4.

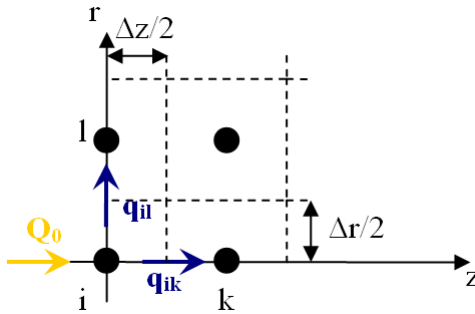


Figure 4.1-6: Heat transfer scheme for the impacted element

Then, using the same methodology, the change in the amount of energy density on system i in a time step  $\Delta t$  relative to this case shown on Figure 4.1-6 is given by

$$\Delta E_i = \Delta t \left[ \frac{8}{\pi \Delta r^2 \Delta z} Q_0 + \frac{k}{\Delta r^2 \Delta z^2} \left( 2 \Delta r^2 T_k + 4 \Delta z^2 T_l - 2 \Delta r^2 + 4 \Delta z^2 T_i \right) \right] \quad (4.12)$$

#### 4.1.2.3. Case of bottom layer nodes

In this case, node i belongs to the bottom side ( $r=0$ ) of the outside square of the meshing presented in Figure 4.1-4 minus its extremities.

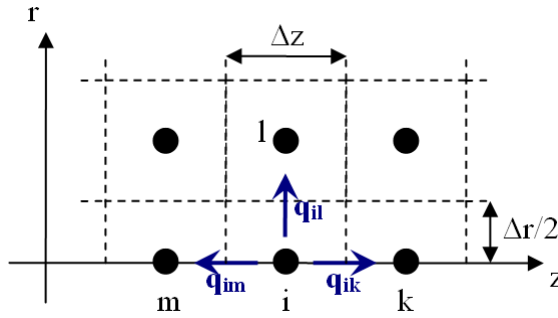


Figure 4.1-7: Heat transfer scheme for bottom layer nodes

The change in the amount of energy density on system i in a time step  $\Delta t$  relative to this case shown on Figure 4.1-7 is given by

$$\Delta E_i = \frac{k \Delta t}{\Delta r^2 \Delta z^2} \left[ \Delta r^2 T_k + \Delta r^2 T_m + 4 \Delta z^2 T_l - 2 \Delta r^2 + 4 \Delta z^2 T_i \right] \quad (4.13)$$

#### 4.1.2.4. Case of top layer nodes

The node i in this case belongs to the upper side of the outside square of the meshing presented in Figure 4.1-4 minus its extremities.



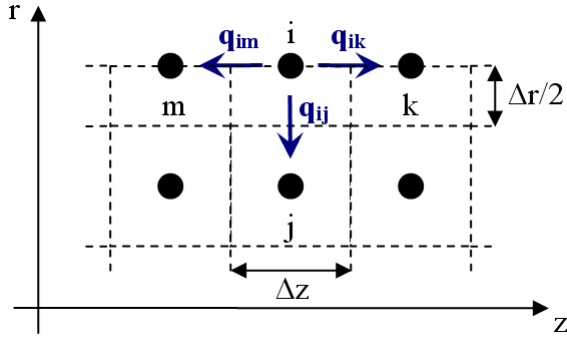


Figure 4.1-8: Heat transfer scheme for top layer nodes

The change in the amount of energy density on system  $i$  in a time step  $\Delta t$  relative to this case shown on Figure 4.1-8 is given by

$$\Delta E_i = \frac{k \Delta t}{\Delta z^2 \Delta r^2} \left[ \left( \frac{2 \Delta z^2}{\left(j - \frac{1}{4}\right) \ln\left(1 - \frac{1}{j}\right)} - 2 \Delta r^2 \right) T_i - \frac{2 \Delta z^2}{\left(j - \frac{1}{4}\right) \ln\left(1 - \frac{1}{j}\right)} T_j \right. \\ \left. + \Delta r^2 T_k + \Delta r^2 T_m \right] \quad (4.14)$$

#### 4.1.2.5. Case of left side nodes

The node  $i$  here belongs to the left side ( $z=0$ ) of the outside square of the meshing presented in Figure 4.1-4 minus its extremities.

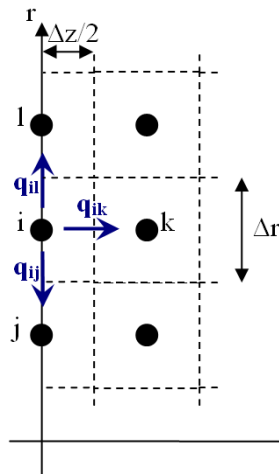


Figure 4.1-9: Heat transfer scheme for left side nodes

The change in the amount of energy density on system i in a time step  $\Delta t$  relative to this case shown on Figure 4.1-9 is given by

$$\Delta E_i = \frac{k \Delta t}{\Delta z^2 \Delta r^2} \left[ \left( \frac{\Delta z^2}{j \ln \left( 1 - \frac{1}{j} \right)} - \frac{\Delta z^2}{j \ln \left( 1 + \frac{1}{j} \right)} - 2 \Delta r^2 \right) T_i - \frac{\Delta z^2}{j \ln \left( 1 - \frac{1}{j} \right)} T_j \right. \\ \left. + 2 \Delta r^2 T_k + \frac{\Delta z^2}{j \ln \left( 1 + \frac{1}{j} \right)} T_l \right] \quad (4.15)$$

#### 4.1.2.6. Case of right side nodes

In this case, node i belongs to the right side of the outside square of the meshing presented in Figure 4.1-4 minus its extremities.

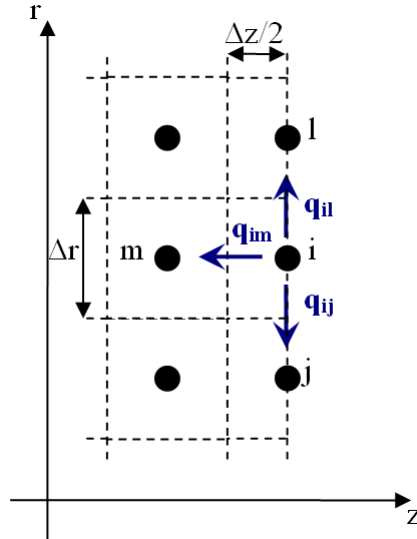


Figure 4.1-10: Heat transfer scheme for right side nodes

The change in the amount of energy density on system i in a time step  $\Delta t$  relative to this case shown on Figure 4.1-10 is given by

$$\Delta E_i = \frac{k\Delta t}{\Delta z^2 \Delta r^2} \left[ \left( \frac{\Delta z^2}{j \ln\left(1 - \frac{1}{j}\right)} - \frac{\Delta z^2}{j \ln\left(1 + \frac{1}{j}\right)} - 2 \Delta r^2 \right) T_i - \frac{\Delta z^2}{j \ln\left(1 - \frac{1}{j}\right)} T_j + 2 \Delta r^2 T_m \right. \\ \left. + \frac{\Delta z^2}{j \ln\left(1 + \frac{1}{j}\right)} T_i \right] \quad (4.16)$$

#### 4.1.2.7. Case of the first element

This node corresponds to the node in the upper left corner of the outside square of the meshing presented in Figure 4.1-4.

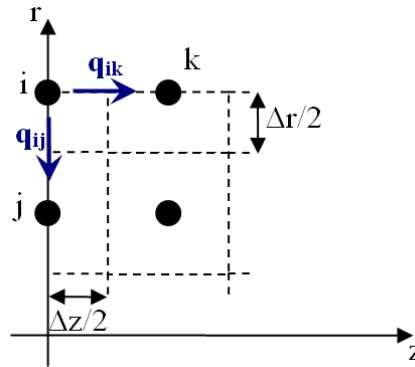


Figure 4.1-11: Heat transfer scheme for the first element

The change in the amount of energy density on system i in a time step  $\Delta t$  relative to this case shown on Figure 4.1-11 is given by

$$\Delta E_i = \frac{k \Delta t}{\Delta z^2 \Delta r^2} \left[ \left( \frac{2 \Delta z^2}{\left( j - \frac{1}{4} \right) \ln \left( 1 - \frac{1}{j} \right)} - 2 \Delta r^2 \right) T_i - \frac{2 \Delta z^2}{\left( j - \frac{1}{4} \right) \ln \left( 1 - \frac{1}{j} \right)} T_j + 2 \Delta r^2 T_k \right] \quad (4.17)$$

#### 4.1.2.8. Case of the last element

This node corresponds to the node in the bottom right corner of the outside square of the meshing presented in Figure 4.1-4.

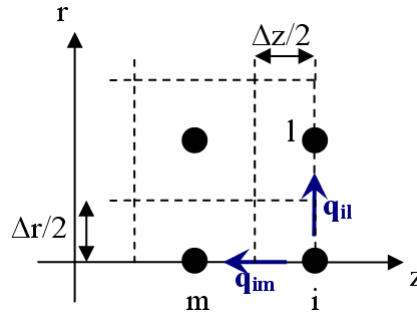


Figure 4.1-12: Heat transfer scheme for the last element

The change in the amount of energy density on system i in a time step  $\Delta t$  relative to this case shown on Figure 4.1-12 is given by

$$\Delta E_i = \frac{k \Delta t}{\Delta r^2 \Delta z^2} \left[ 2 \Delta r^2 T_m + 4 \Delta z^2 T_l - 2 \Delta r^2 + 4 \Delta z^2 T_i \right] \quad (4.18)$$

Finally, the last case corresponds to the node located in the upper right corner of the outside square of the meshing presented in Figure 4.1-4. This node is considered to act as a heat sink from which heat is lost to environment. As a consequence, its temperature is fixed to 300 K.

Knowing the changes in the amount of energy of all the elements, the temperature distribution in the vicinity of the arc impacted point of the electrode can then be obtained by following the procedure described on Figure 4.1-13 for each new thermal state  $E(i)$ .

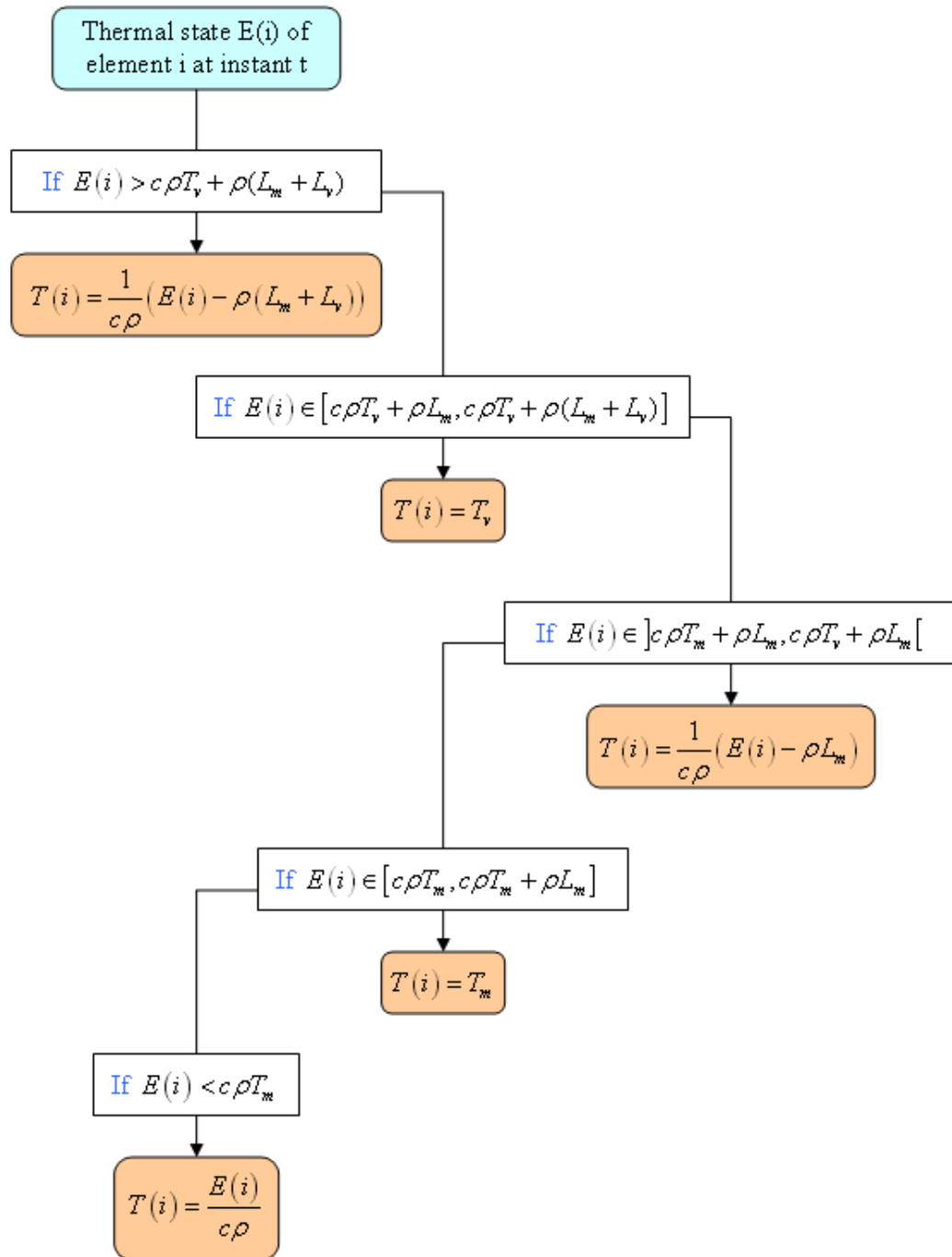
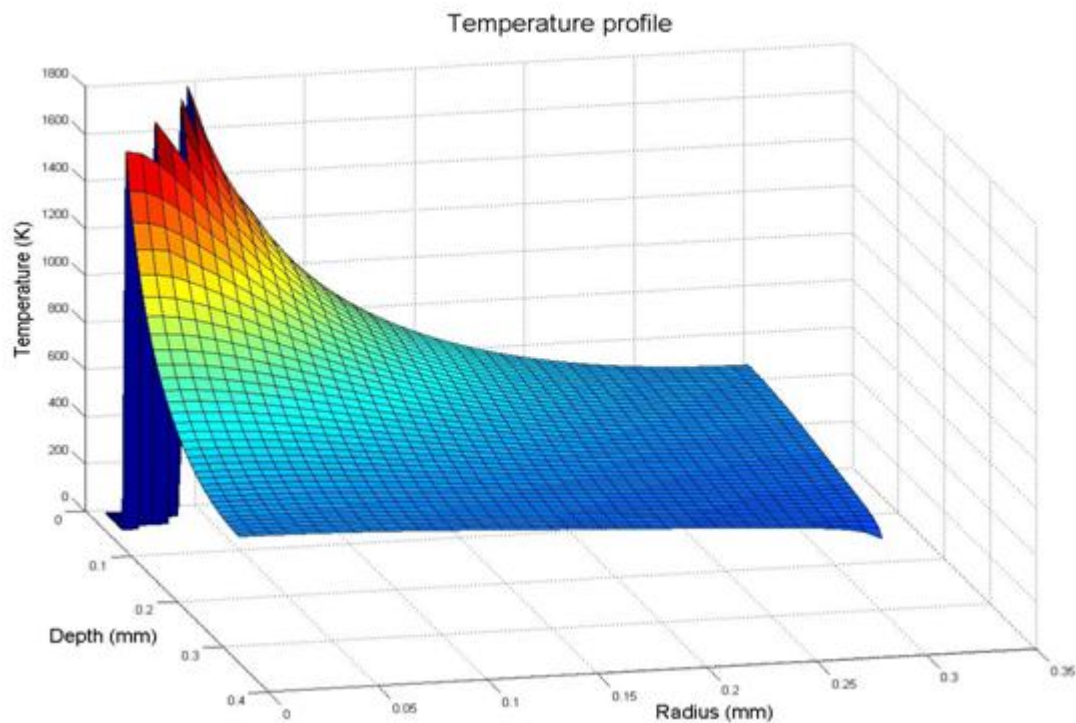


Figure 4.1-13: Flowchart describing the procedure to get the temperature from the thermal state where  $L_m$  &  $L_v$  are respectively the latent heat of fusion and vaporization and  $c$  the specific heat.

The thermal model then gives temperature profiles, such as the one shown on Figure 4.1-14, at each time  $t$  of the breaking process in a slice of the contact material represented on Figure 4.1-4. The temperatures of all the elements which have been vaporized during the breaking process are set to 0 K at the end of the simulation in order to have a graphical representation of the total amount of contact material removed by vaporization after one contact opening.



**Figure 4.1-14: Temperature distribution at the arc extinction ( $I = 9$  A,  $V = 64$  VDC,  $S = 1$  m/s)**

This model output is used to deduce the molten pool size at each time step and the total amount of material vaporized after one breaking operation. Since deposition mechanisms are disregarded in this model, all vaporized material is considered to be part of the arc erosion.

### 4.1.3. Magneto-hydrodynamic Model

The interaction of the material and the heat source leads to rapid heating, melting and vigorous circulation of the molten metal driven by buoyancy, surface tension and electromagnetic forces [30]. The purpose of this model is to obtain the amount of contact material ejected through the splash erosion process. Indeed, whenever the contact material starts melting, this model considers the formation of a molten metal jet at the contact surface center of the molten pool and along the z-axis. Assuming that this molten metal jet behaves as a free viscous jet, it keeps growing under the influence of driving forces induced by the electrical arc during the breaking operation. In Figure 4.1-15, where the liquid jet can be seen at time t, the molten pool surface (at  $z = 0$ ) is assumed to correspond to the contact surface of the electrode under study.

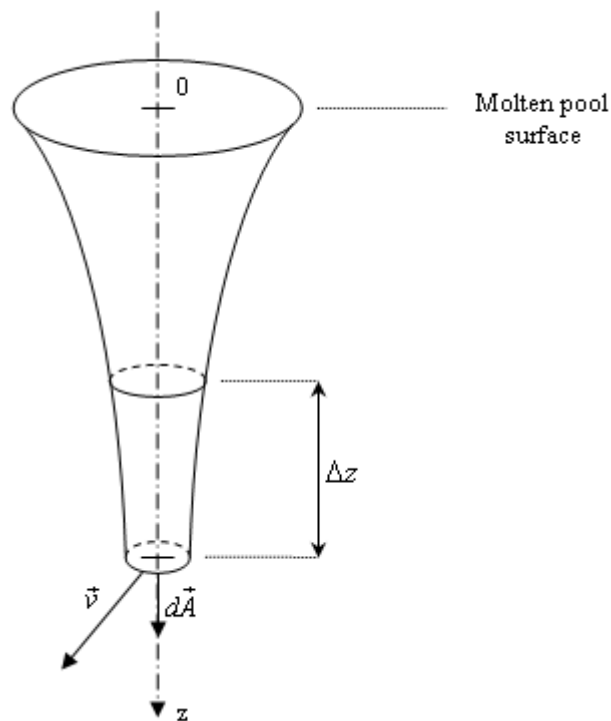


Figure 4.1-15: Scheme of the molten metal jet

Whenever this liquid jet reaches critical conditions of stability, a droplet comes off the molten metal jet tip and is ejected. All the ejected droplets after one breaking operation are assumed to constitute the splash erosion part of the arc erosion, since deposition mechanisms are disregarded in this study.

#### 4.1.3.1. Molten pool driving forces

During the breaking process, molten metal is driven by gravity, buoyancy, surface tension and electromagnetic forces [30-43]. In this model, only surface tension is assumed to prevent the molten metal jet from growing and therefore, the three other driving forces are considered to be working together to make it grow.

The buoyancy force, induced by the density change with the spatial temperature distribution, is given by:

$$F_{Buoy} = \rho g \alpha (T - T_m) \quad (4.19)$$

Where  $g$  is the standard gravity

$\rho$  is the density

$\alpha$  is the thermal expansion coefficient

$T_m$  is the melting temperature

$T$  is the molten metal jet tip temperature

Therefore, the buoyancy force at time  $t$  depends on the value of the molten metal jet tip temperature at time  $t$ , which is an output of the thermal model developed in the previous section. This molten jet tip temperature is assumed to be the temperature at the center of the electrode where the molten metal jet is formed and also where the arc strikes.



The electromagnetic force resulting from the interaction between the current flow and its self-induced magnetic field, is given by:

$$\vec{F}_{Elec} = \vec{J} \times \vec{B} \quad (4.20)$$

Where  $\vec{J}$  is the current density

$\vec{B}$  is the self-induced magnetic flux

Then, in order to derive the expression of the electromagnetic force, we used the study of Kumar and DebRoy [52] where they calculated the three-dimensional electromagnetic force field during arc welding. Thus, under the same assumptions, the z-component in the cylindrical coordinate system of the electromagnetic force is:

$$F_z = J_r B_\theta = \frac{\mu_m i^2}{4\pi^2 r^2 l} \left[ 1 - \exp\left(-\frac{r^2 d}{r_a^2}\right)^2 \right] \left(1 - \frac{z}{l}\right) \quad (4.21)$$

Where  $\mu_m$  is the magnetic permeability of the material

$i$  is the current intensity

$l$  is the thickness

$d$  is the current density distribution factor

$r_a$  is the arc radius

However, in our model, we need the value of the electromagnetic force at the center of the electrode. Therefore, the force at the center of the electrode is obtained through a Taylor series development:

$$F_z \Big|_{r \rightarrow 0} = \frac{\mu_m i^2}{4\pi^2 r^2 l} \left[ 1 - \left( 1 + 2 \left( -\frac{r^2 d}{r_a^2} \right) + \frac{\left( -\frac{r^2 d}{r_a^2} \right)^2}{2!} + \dots + \dots \right) \right] \left(1 - \frac{z}{l}\right) \quad (4.22)$$

Consequently, the axial electromagnetic force at the center of the contact surface is:

$$F_{Elec} \underset{r \rightarrow 0}{=} \frac{\mu_m i^2 d}{2\pi^2 r_a^2 l} \quad (4.23)$$

It can clearly be seen that the electromagnetic force at time  $t$  depends on the value of the intensity at time  $t$ , which is an output of the energy transport model developed in the previous section.

#### 4.1.3.2. Axial velocity distribution

In order to describe the formation and the evolution of the molten metal jet during the breaking process, the axial velocity of the jet tip at each time step needs to be derived. To this end, we used the theory about free viscous inertial jets developed by J. N. Anno in [51] and adapted it to the case of a molten metal jet subjected to forces induced by the electrical arc.

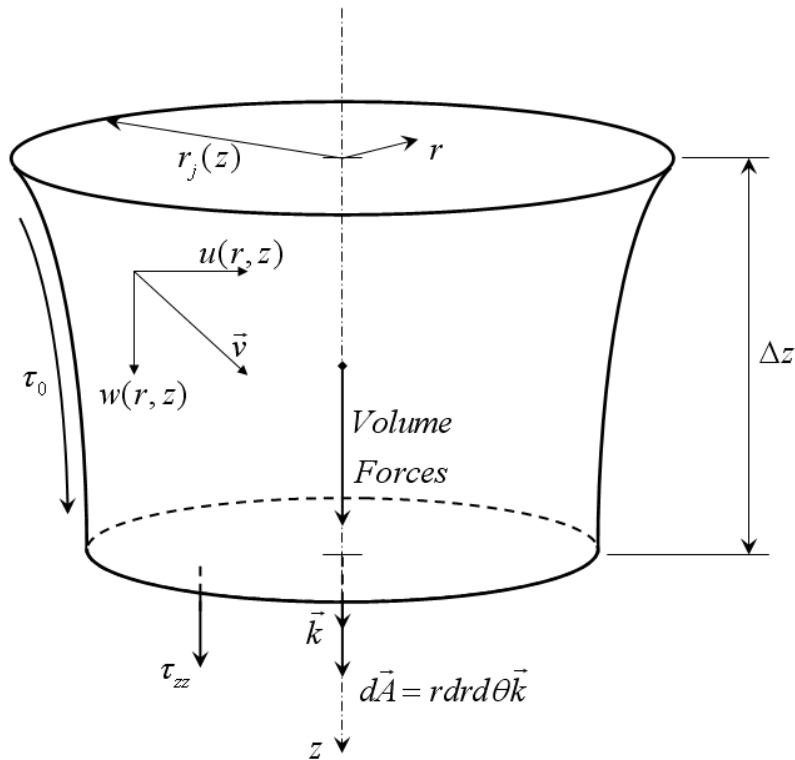


Figure 4.1-16: Differential element of the molten metal jet

First, the momentum equation for the molten metal cylindrical jet can be developed by evaluating the forces acting on a differential element of the jet (See Figure 4.1-16). Considering this element as a control volume and the case of steady flow, Newton's second law projected on the z-axis gives:

$$\sum F_z = \Delta \int_{\text{Control Surface}} \rho w \vec{v} \cdot d\vec{A} \quad (4.24)$$

The different forces acting on this differential element are:

- The volume forces (gravity, buoyancy, electromagnetic)

$$\begin{aligned} F_1 &= m_{\text{control volume}} \left( g \left[ 1 + \alpha(T - T_m) \right] + \frac{\mu_m i^2 d}{2\rho\pi^2 r_a^2 l} \right) \\ &= \rho\pi r_j^2 \Delta z \left( g \left[ 1 + \alpha(T - T_m) \right] + \frac{\mu_m i^2 d}{2\rho\pi^2 r_a^2 l} \right) \end{aligned} \quad (4.25)$$

- The force due to the shear stress on the surface of the differential element

$$F_2 = \tau_0 (\text{Lateral Surface Area})_{\text{control volume}} = 2\pi r_j \Delta z \tau_0 \quad (4.26)$$

- The force due to the normal stress in the z-direction

$$F_3 = \Delta \left( \int_0^{2\pi} \int_0^{r_j} \tau_{zz} \vec{k} \cdot d\vec{A} \right) = \Delta \int_0^{r_j} 2\pi r \tau_{zz} dr \quad (4.27)$$

The right hand side of Newton's second law can be rewritten:

$$\Delta \int_{\text{control surface}} \rho w \vec{v} \cdot d\vec{A} = \Delta \int_0^{2\pi} \int_0^{r_j} \rho w^2 r dr d\theta = \Delta \int_0^{r_j} 2\pi \rho r w^2 dr \quad (4.28)$$

Consequently, the Newton's second law gives:

$$\Delta \int_0^{r_j} 2\pi \rho r w^2 dr = \Delta \int_0^{r_j} 2\pi r \tau_{zz} dr + \tau_0 2\pi r_j \Delta z + \rho\pi r_j^2 \Delta z \left( g \left[ 1 + \alpha(T - T_m) \right] + \frac{\mu_m i^2 d}{2\rho\pi^2 r_a^2 l} \right) \quad (4.29)$$

Then, dividing by  $\Delta z$  and taking limits, we get the momentum equation for the liquid jet:

$$\frac{\partial}{\partial z} \int_0^{r_j} 2\pi\rho r w^2 dr = \frac{\partial}{\partial z} \int_0^{r_j} 2\pi r \tau_{zz} dr + \tau_0 2\pi r_j + \rho\pi r_j^2 \left( g \left[ 1 + \alpha(T - T_m) \right] + \frac{\mu_m i^2 d}{2\rho\pi^2 r_a^2 l} \right) \quad (4.30)$$

However, the conservation of flow rate equation is:

$$\rho\pi r_j^2 w = \rho\pi r_{j0}^2 w_0 \quad (4.31)$$

Therefore, considering the molten metal jet as a free jet,  $\tau_0 = 0$  and assuming that  $w = w(z)$  only and that  $\tau_{zz} = \tau_{zz}(z)$  only, combining Equations 4.30 & 4.31 gives the following differential equation:

$$\frac{\partial w}{\partial z} = \frac{1}{\rho} \frac{\partial}{\partial z} \left( \frac{\tau_{zz}}{w} \right) + \frac{g \left[ 1 + \alpha(T - T_m) \right] + \frac{\mu_m i^2 d}{2\rho\pi^2 r_a^2 l}}{w} \quad (4.32)$$

Now expressing stresses as a function of the axial and radial velocities and as a function of the hydrostatic pressure  $p$  and the molten metal viscosity  $\mu$  gives:

$$\begin{cases} \tau_{rr} = -p + 2\mu \frac{\partial u}{\partial r} \\ \tau_{zz} = -p + 2\mu \frac{\partial w}{\partial z} \end{cases} \quad (4.33)$$

Moreover, the continuity equation gives:

$$u = -\frac{1}{2} r \frac{\partial w}{\partial z} \quad (4.34)$$

And the stress component  $\tau_{rr}$  can also be expressed as a function of the surface tension  $\gamma$ :

$$\tau_{rr} = -\frac{\gamma}{r_j} \quad (4.35)$$

Consequently, putting together these three equations:

$$\tau_{zz} = -\frac{\gamma}{r_j} + 3\mu \frac{\partial w}{\partial z} \quad (4.36)$$

Where  $r_j(z)$  and  $w(z)$  are related by the conservation of flow rate equation (Equation 4.31). Therefore, substituting Equation 4.36 into Equation 4.32 gives the following differential equation for  $w(z)$  :

$$\frac{\partial w}{\partial z} = \frac{3\mu}{\rho} \frac{\partial}{\partial z} \left( \frac{1}{w} \frac{\partial w}{\partial z} \right) + \frac{\gamma}{2\rho r_{j0} \sqrt{w_0}} \frac{1}{w^{3/2}} \frac{\partial w}{\partial z} + \left( g \left[ 1 + \alpha(T - T_m) \right] + \frac{\mu_m i^2 d}{2\rho \pi^2 r_a^2 l} \right) \frac{1}{w} \quad (4.37)$$

Where  $w$  is the axial velocity

$\mu$  is the molten metal viscosity

$\gamma$  is the surface tension

$r_{j0}$  is the molten pool radius

$w_0$  is the velocity at the contact surface

Solving this non linear differential equation (Equation 4.37) allows us to get the axial velocity distribution of the molten metal jet.

In order to compare this result with what Anno found in the case of a free viscous inertial jet, Equation 4.37 has been put into dimensionless form, where  $W$  is related to the axial velocity of the molten metal jet and  $Z$  is related to the axial coordinate  $z$ . It gives:

$$W'' = \left( W + \frac{W'}{W} - \frac{\xi}{\sqrt{W}} \right) W'^{-1} \quad (4.38)$$

$$\text{with } w = \left( \frac{3\mu}{\rho} \left( g \left[ 1 + \alpha(T - T_m) \right] + \frac{\mu_m i^2 d}{2\rho \pi^2 r_a^2 l} \right) \right)^{1/3} W$$

$$z = \left( \frac{3\mu}{\rho} \right)^{2/3} \left( g \left[ 1 + \alpha(T - T_m) \right] + \frac{\mu_m i^2 d}{2\rho \pi^2 r_a^2 l} \right)^{-1/3} Z$$

$$\zeta = \frac{1}{2} \left( \frac{\gamma}{\rho r_{j0}} \right) \left( \frac{\rho}{3\mu} \right)^{2/3} \left( g + 1 + \alpha(T - T_m) + \frac{\mu_m i^2 d}{2\rho\pi^2 r_a^2 l} \right)^{-2/3} \frac{1}{\sqrt{w_0}}$$

Where it can be noticed that parameter  $\zeta$  depends on the current intensity  $i$  at time  $t$ , which is an output of the arc energy transport model, and on the jet tip temperature and the molten pool radius at time  $t$ , which are outputs of the thermal model.

And J. N. Anno found:

$$W'' = \left( W + \frac{W'}{W} - \frac{\zeta}{W} \right) W'^{-1} \quad (4.39)$$

Therefore, only a square root difference with Anno's result can be observed.

#### 4.1.3.3. Jet stability conditions

During the arcing process, the molten metal jet keeps growing until it reaches a critical length after which a droplet will form. Now that we know the axial velocity distribution, it is important to define the critical conditions under which there will be formation of a droplet, and thus ejection of contact material. To this end, we used the theory about an analysis of the conditions for instability of a viscous cylindrical jet developed by J. N. Anno in [51], where he got a result identical to that obtained by Weber [53].

Therefore, critical conditions of formation of a droplet in the arcing case are derived as an extension of this theory based on an integral form of the conservation of mechanical energy (See Equation 4.40).

$$\int_V \rho X_i u_i dV + \int_S \tau_{ij} n_j u_i dS - \int_S \rho u_j n_j \left( \frac{1}{2} q^2 \right) dS - \int_V \frac{\partial}{\partial t} \left( \frac{1}{2} \rho q^2 \right) dV - \int_V R dV = 0 \quad (4.40)$$

Where  $X_i$  is the generalized body force

$\tau_{ij}$  is the stress tensor

$u_i$  is the velocity component in the  $i^{\text{th}}$  direction

$n_j$  is the projection of the outward unit normal to the surface in the  $j^{\text{th}}$  direction

$$q = u_i u_i$$

$R$  is the viscous energy dissipation, given by  $R = \frac{\mu}{2} (u_{i,j} + u_{j,i})^2$

Let's consider the following particular form of axial disturbance on the cylindrical molten metal jet, frequently termed a “sausage” perturbation:

$$r_s = r_u + \delta(t) \cos k_\lambda z \quad (4.41)$$

Where  $r_u$  is the radius of the unperturbed cylinder

$\delta(t)$  is a small time-dependent disturbance amplitude

$k_\lambda = 2\pi/\lambda$  is the wave number,  $\lambda$  being the wavelength of the perturbation

This perturbation from the equilibrium cylindrical jet is sketched in Figure 4.1-17. It has been demonstrated in [51] that for such conditions and perturbation, the velocity field is:

$$\begin{cases} u_r = \frac{r}{r_u} \dot{\delta} \cos k_\lambda z \\ u_z = w_0 - \frac{2\dot{\delta}}{k_\lambda r_u} \sin k_\lambda z \end{cases} \quad (4.42)$$

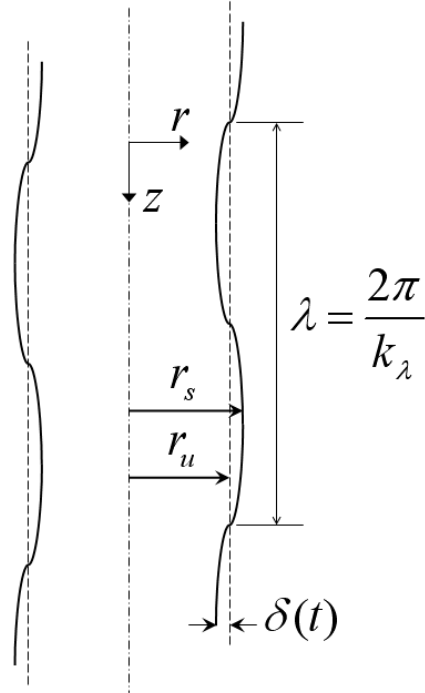


Figure 4.1-17: Cylindrical molten metal jet with axial disturbance

Then, performing the integrations on a stationary control volume such as the unperturbed jet, a cylinder of radius  $r_u$  and length  $n\lambda$  where  $n$  is an integer, the different terms of the mechanical energy balance can be obtained:

$$\left\{ \begin{array}{l}
 \int_V \rho X_i u_i dV = \left( \rho g + 1 + \alpha(T - T_m) + \frac{\mu_m i^2 d}{2\pi^2 r_a^2 l} \right) \frac{w_0 2n\pi^2 r_u^2}{k_\lambda} \\
 \int_S \tau_{ij} n_j u_i dS = \frac{2n\pi^2 \gamma \delta \dot{\delta}}{k_\lambda r_u} (1 - k_\lambda^2 r_u^2) \\
 \int_S \frac{1}{2} \rho u_j n_j u_i u_i dS = 0 \\
 \int_V \frac{\partial}{\partial t} \left( \frac{1}{2} \rho u_i u_i \right) dV = \frac{n\pi^2 \rho \delta \ddot{\delta}}{2k_\lambda^3} (8 + k_\lambda^2 r_u^2) \\
 \int_V R dV = \int_V 2\mu \left[ \left( \frac{\partial u_r}{\partial r} \right)^2 + \left( \frac{\partial u_z}{\partial z} \right)^2 + \left( \frac{u_r}{r} \right)^2 + \frac{1}{2} \left( \frac{\partial u_r}{\partial z} + \frac{\partial u_z}{\partial r} \right)^2 \right] dV \\
 = \frac{n\pi^2 \mu \dot{\delta}^2}{2k_\lambda} (4 + k_\lambda^2 r_u^2)
 \end{array} \right. \quad (4.43)$$



Thus, the integral equation energy leads, after cancellation, to the following non-linear differential equation (where  $\eta = k_\lambda r_u$ ):

$$\begin{aligned} \delta\ddot{\delta} + \frac{\mu k_\lambda^2}{\rho} \left( \frac{24 + \eta^2}{8 + \eta^2} \right) \delta\dot{\delta} - \frac{4\gamma\eta^2}{\rho r_u^3} \left( \frac{1 - \eta^2}{8 + \eta^2} \right) \delta\dot{\delta} \\ + \left( g + 1 + \alpha(T - T_m) + \frac{\mu_m \dot{t} d}{2\rho\pi^2 r_a^2 l} \right) \frac{4w_0\eta^2}{8 + \eta^2} = 0 \end{aligned} \quad (4.44)$$

It can be shown that the former differential equation (Equation 4.44) has the same pseudo-period as the following second order linear differential equation:

$$\ddot{\delta} + \frac{\mu k_\lambda^2}{\rho} \left( \frac{24 + \eta^2}{8 + \eta^2} \right) \delta\dot{\delta} - \frac{4\gamma\eta^2}{\rho r_u^3} \left( \frac{1 - \eta^2}{8 + \eta^2} \right) \delta = 0 \quad (4.45)$$

Then, for exponentially growing solutions  $e^{\omega t}$ , we have from equation 4.45:

$$\omega^2 + \frac{3\mu k_\lambda^2}{\rho} \omega - \frac{\gamma}{2\rho r_u^3} (1 - \eta^2) \eta^2 = 0 \quad (4.46)$$

Now assuming the case of a very viscous jet such that  $3\mu k_\lambda^2/2\rho^2 \ll \gamma/2\rho r_u^3$ , we have from equation 4.46:

$$\omega = \frac{\gamma}{6\mu r_u} (1 - \eta^2) \quad (4.47)$$

However, from [51, 54], the jet breakup time may be taken as:

$$t_c = \frac{z_c}{u_z} \cong \frac{1}{\omega} \ln e^{12} = \frac{12}{\omega} \quad (4.48)$$

Consequently, considering the highest value for  $\omega$  corresponding to  $\eta = 0$  in order to work with the shortest breakup time possible, and thus to be in the worst arc erosion conditions, we come up with this new stability condition result corresponding to the critical jet breakup time:

$$t_c = \frac{72\mu r_{j0}}{\gamma} \quad (4.49)$$

Where  $r_{j0}$  is the molten pool radius

$\mu$  is the molten metal viscosity

$\gamma$  is the surface tension

The molten pool radius can be deduced at each time step of the simulation from the temperature distribution within the electrode, and is then an output of the thermal model.

Whenever this critical time is reached in the simulation, it is considered that a spherical molten metal droplet is formed, whose radius is given from [51] by:

$$R_0 = 2r_{jc} \quad (4.50)$$

Where  $r_{jc}$  is the jet radius at breakup

Therefore, the amount of material removed by splash erosion during one breaking process consists in the sum of all the ejected molten metal droplets during one simulation as given by:

$$m_{spl} = \sum_{Droplets} \frac{4}{3} \pi \rho R_0^3 \quad (4.51)$$

Finally, the sum of all contact material removed by vaporization and removed by splash erosion corresponds to the total amount of contact material removed by arc erosion during one breaking operation.

## 4.2. Arc erosion experiments

In cooperation with our industrial partner Esterline Power Systems, high current arc erosion experiments have been conducted on AgCdO power switching devices in

conditions similar to operating conditions in airplanes. The main purpose of these experiments is to obtain the total amount of material removed by arc erosion for different current intensities. Therefore, five AgCdO electrical contacts have been subjected to one breaking operation under DC current at 200, 400, 600, 800, & 1000 A. White light interferometry has then been used to measure the total amount of material removed by arc erosion.

#### **4.2.1. Sample Definition**

The five power switching devices are the same as the ones described in Chapter 2. They are all composed of a moving contact and a static one (See Figure 4.2-1)



**Figure 4.2-1: Pictures of the static and the moving contacts used in this experiment**

From a composition point of view, test contacts of 90%Ag-10%CdO (by weight) that were prepared by powder metallurgical techniques have been used. The process used is sintering. These contacts with silver backings were brazed to copper cylindrical pieces so that they could be positioned in the power switching device.

#### **4.2.2. Test Condition and Testing Procedure**

The five contacts have all been tested under the same operating conditions: circuit voltage of 28 V DC, ambient air, room temperature, resistive load. The only difference between them lies in the current intensity they have been subjected to. The purpose being to compare experimental to model results, we have made our samples undergo one “half-

cycle” (only one break operation) at five different intensities: 200, 400, 600, 800, and 1000A. This procedure allows us to analyze the impact resulting only from one single electrical arc.

### 4.2.3. White Light Interferometry

The morphology of each of the arc impacted surfaces has been measured using a white light interferometer. Figure 4.2-2 and Figure 4.2-3 show respectively a top view and a 3-D view of the electrode surface, resulting from white light interferometry measurements, after one breaking operation at 600 A and 28 VDC.

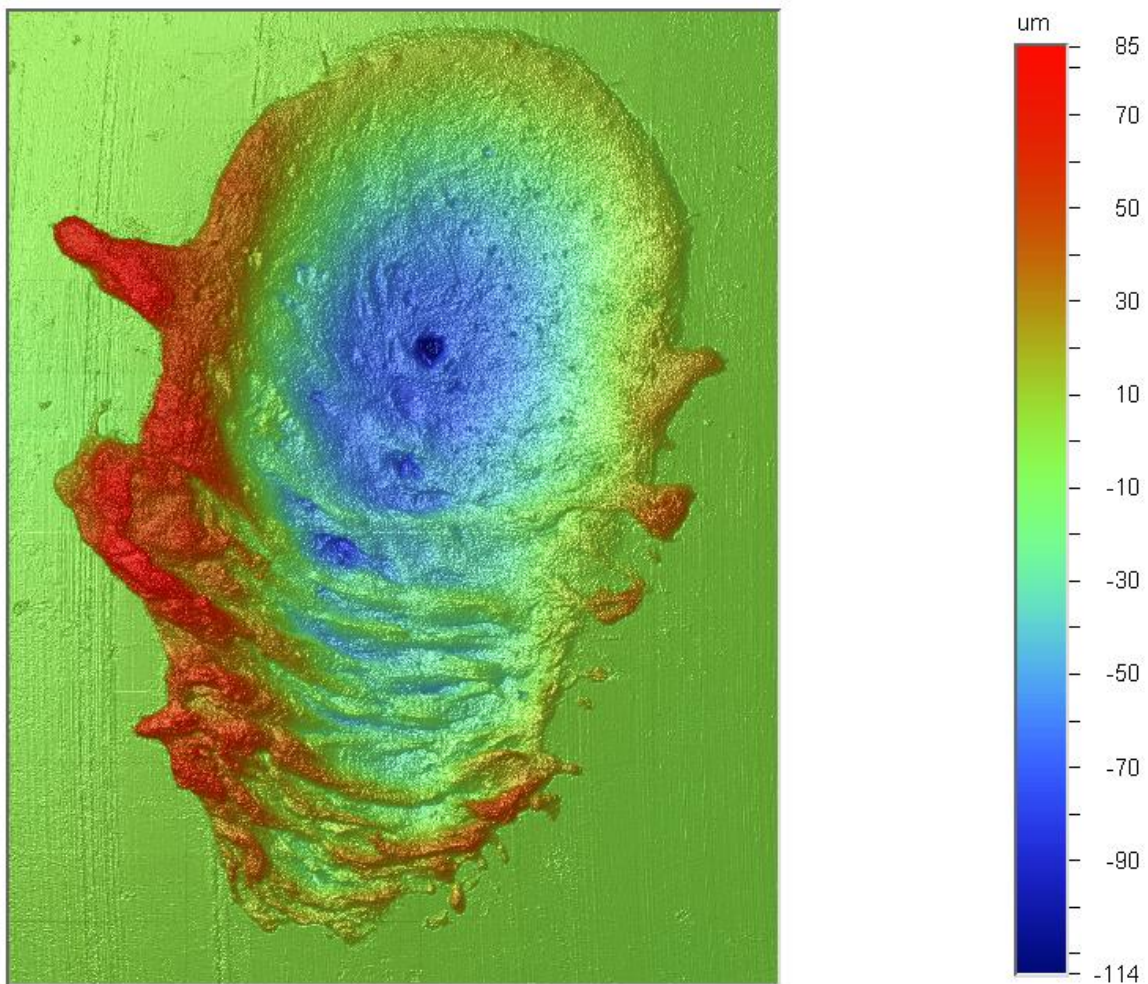


Figure 4.2-2: WLI picture of an arc impact after one breaking operation (600 A, 28 VDC)

It can clearly be seen on these two figures that the electrical arc has moved during contact opening, from the bottom to the top of Figure 4.2-2 and from the left to the right of Figure 4.2-3. This is another proof of the arc root mobility.

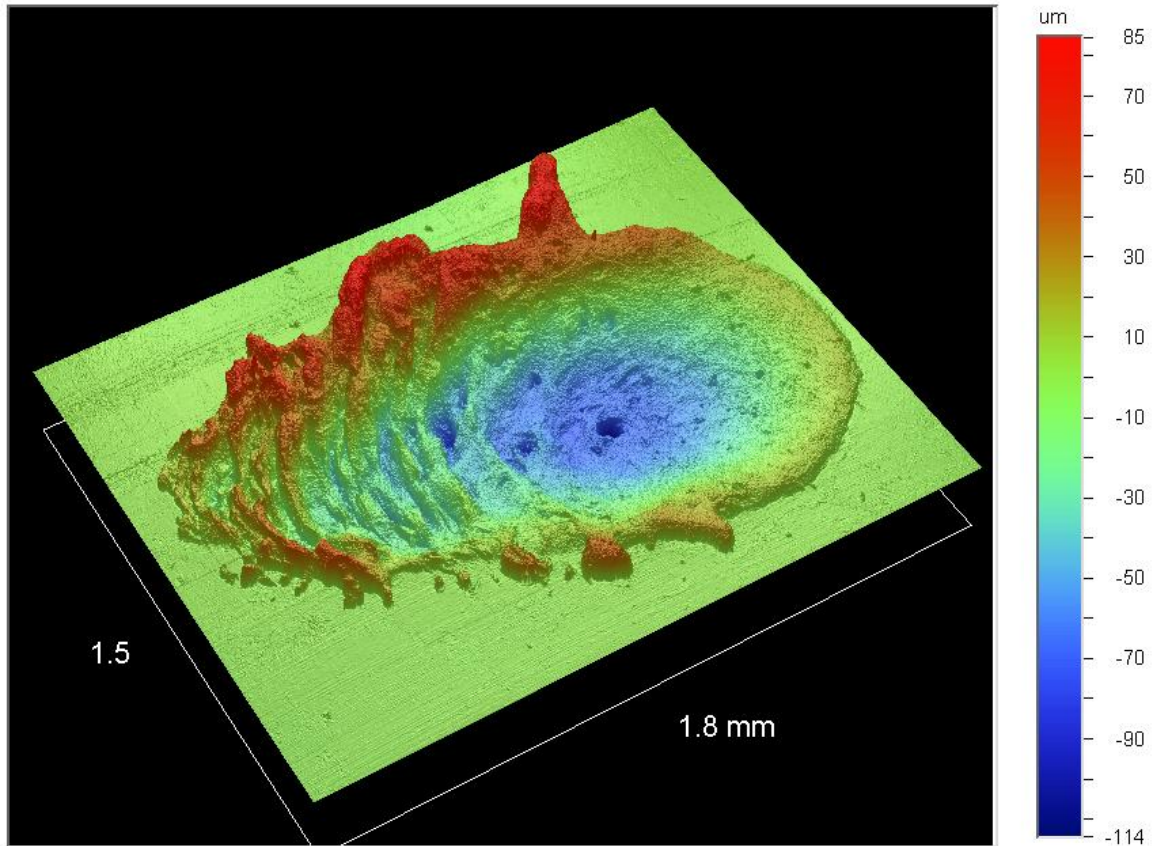


Figure 4.2-3: 3D view of Figure 4.2-2

Then, based on these morphology measurements and using Vision (Veeco software), the total volume of contact material removed has been computed. Finally, the total mass of contact material removed by arc erosion for each sample is obtained by multiplication by the contact material density.

#### 4.2.4. Comparison between model and experimental results

Arc erosion simulations have been performed on AgCdO contact material at different current intensities in order to make a comparison between model results and our high current experimental data. For the sake of the arc erosion simulations on AgCdO, we assumed homogeneous material properties (Surface tension, viscosity, etc.) reflecting the global behaviour of the contact material under study. Total masses of AgCdO material removed by arc erosion during the breaking process for different intensities from the model are plotted on Figure 4.2-4 and compared with experimental data at high currents.

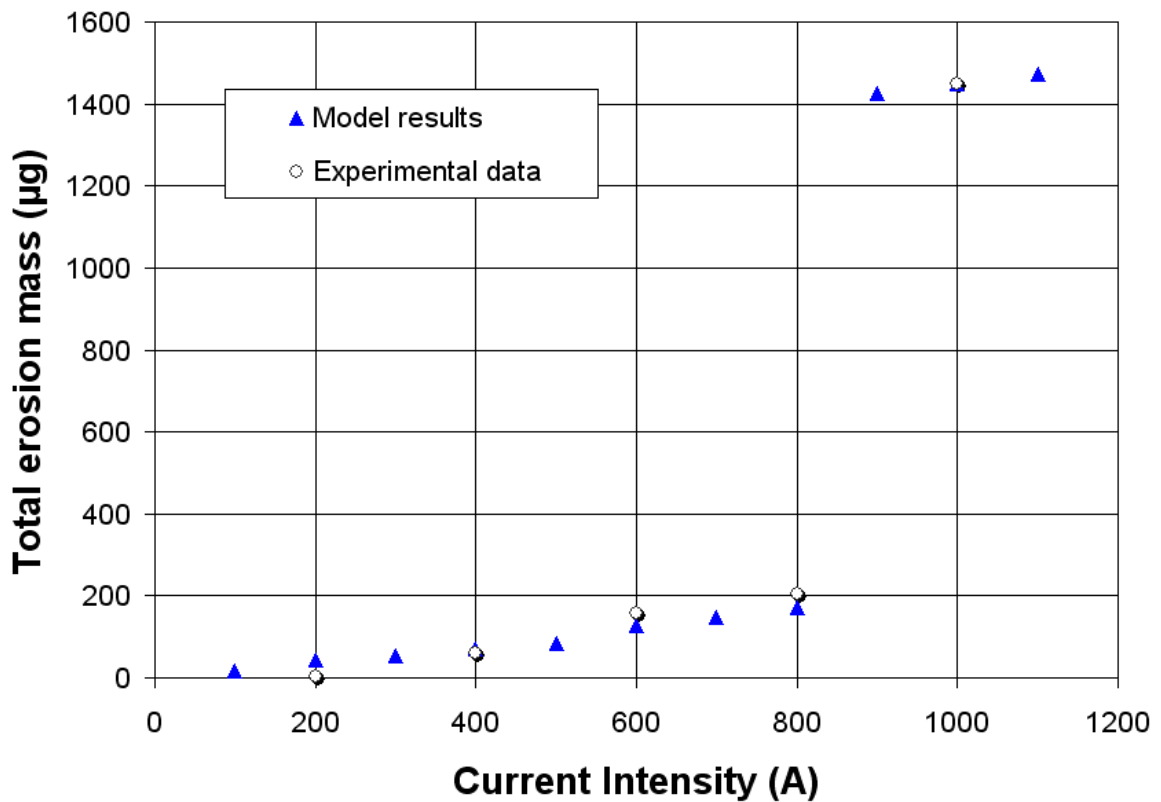


Figure 4.2-4: High current experimental data and model results of AgCdO arc erosion

First, a good fit in between model results and experimental data at high current can be observed on Figure 4.2-4. This therefore validates the arc erosion model at high current. Second, a sudden increase of the arc erosion slope can be noticed from 800 to 1000 A.

This phenomenon is not new and has already been observed and explained by Wu [50]. Indeed, it mainly comes from the fact that splash erosion does not linearly change with the variation of arc current, but exhibits abrupt increases due to sudden ejections of molten metal droplets of bigger size.

Experimental data from the McBride paper [44] relative to some arc erosion experiments on AgCdO electrical contacts at low current have also been compared to model results (See Figure 4.2-5).

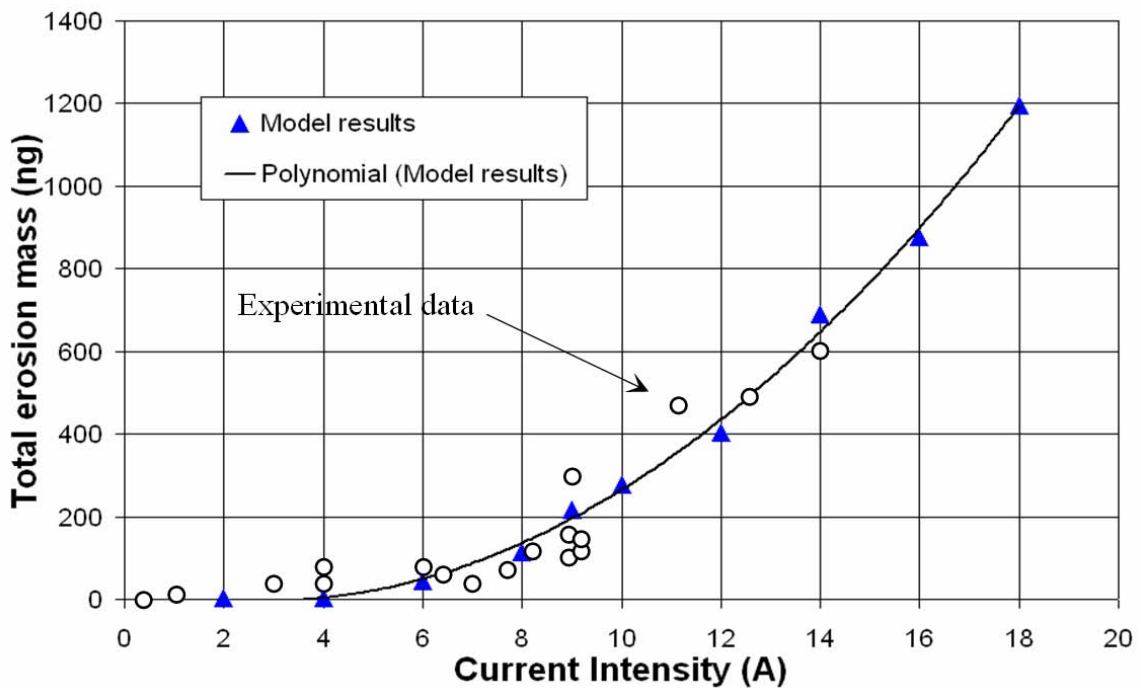


Figure 4.2-5: Low current experimental data [44] and model results of AgCdO arc erosion

A good agreement between model results and experimental data can be seen on Figure 4.2-5. This consequently validates the arc erosion model at low current.

### 4.3. Conclusion

A complete macroscopic arc erosion model describing one breaking operation under DC current has been developed and validated at low and high current on AgCdO. This arc erosion model, which describes the whole breaking operation, results from the combination and coupling of three different models: an arc energy transport model, a thermal model, and a magneto-hydrodynamic model. Since it takes into account the two arc erosion modes, vaporization and splash erosion, it can simulate breaking processes for a wider range of current than former existing models.

Furthermore, this arc erosion model can be used to simulate the arc erosion process of any kind of contact material since it is based on general arc erosion phenomena, vaporization and splash erosion, describing the arc erosion process during contact opening for any kind of contact material. Consequently, it could be used to compare the arc erosion ability of different contact materials with the objective to find the best substitute to AgCdO.

In the next Chapter, this model will be used in order to evaluate the contact material properties and composition influences on the electrical arc erosion phenomenon. In other words, what will be the effects of a change in oxide composition of the contact material on the total amount of material removed after one breaking operation? How important is the density of the contact material in the arc erosion process?



**CHAPTER 5**

**MODELING OF THE CONTACT MATERIAL PROPERTIES &  
COMPOSITION INFLUENCES ON THE ELECTRICAL ARC  
EROSION PHENOMENON**

The general electrical arc erosion model developed in Chapter 4 has been used in a certain way to get closer to the objective of designing a good AgCdO substitute. The methodology has two stages. The first step of this study consists in determining a classification of the contact material properties' influence in the arc erosion process. To this end, *ab initio* calculations are used to determine characteristic ranges of variations of contact material properties over a significant interval of temperatures. Then, based on these *ab initio* results, the complete arc erosion model is used to establish a ranking, which is a key factor in the design of a good AgCdO substitute. The second step consists, based on this new ranking, in determining the consequences for one of these ranked properties of a change in tin oxide composition of the contact material. To reach this goal, *ab initio* calculations are run on two AgSnO<sub>2</sub> compositions.

## 5.1. Contact material properties influence

In contrast to low current, high current arc erosion is mainly driven by splash erosion. In the previously described arc erosion model (Chapter 4), splash erosion is governed by three forces: Buoyancy  $F_{\text{Buoy}}(\rho, \alpha)$ , Electromagnetic  $F_{\text{Elec}}(\mu_m)$ , and Surface tension  $F_{\text{Surf}}(\gamma)$ . This is why the following study will be focused on the four contact material properties related to the forces that act on the molten metal pool to induce the formation of the molten metal liquid jet during the splash erosion process: density  $\rho$ , surface tension  $\gamma$ , thermal expansion  $\alpha$  and magnetic permeability  $\mu_m$ . Furthermore, this study has been conducted on Ag, because we know the evolution of its surface tension coefficient as a function of the temperature [55].

$$\gamma_{\text{Ag}} (mN.m^{-1}) = 1207 - 0.228 \times T(K) \quad (5.1)$$

### 5.1.1. Force contributions

Arc erosion simulations have been run on the single phase material Ag in order to identify the different contributions of forces (See Figure 5.1-1).

The total contact material erosion after one breaking operation has been plotted as a function of the current intensity for four different cases: the complete arc erosion model (to be used as a Reference state) and experimental cases without the electromagnetic force contribution, without the surface tension contribution and without the Buoyancy force contribution.

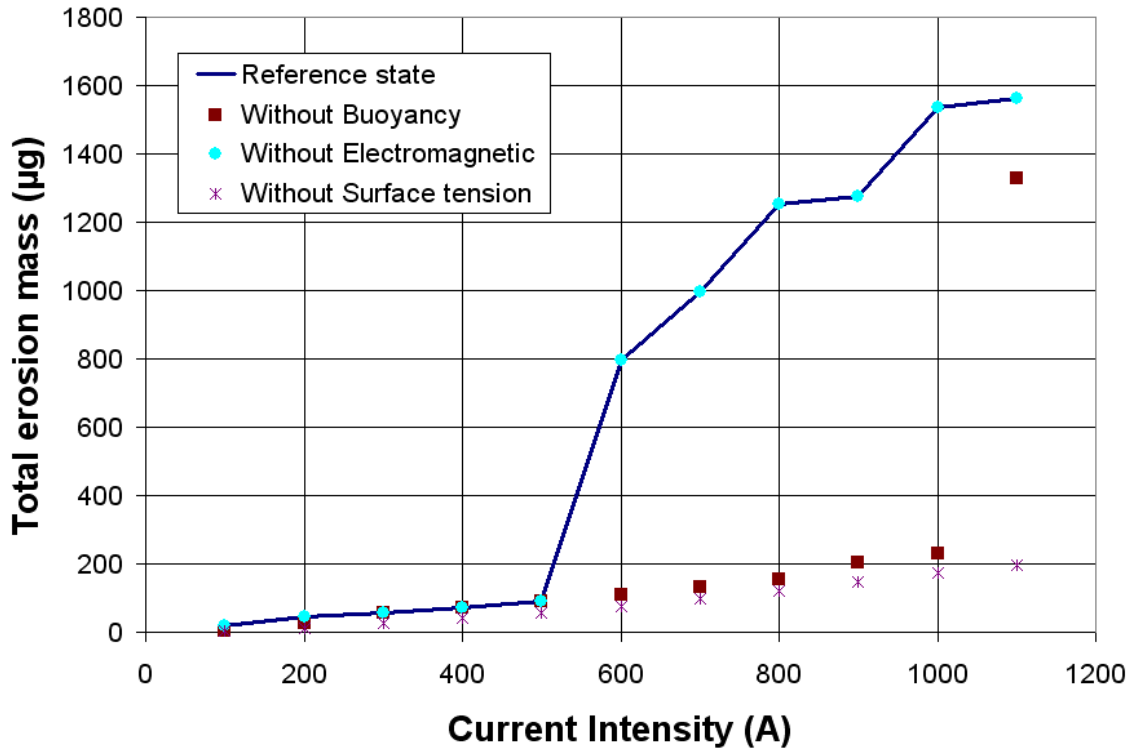
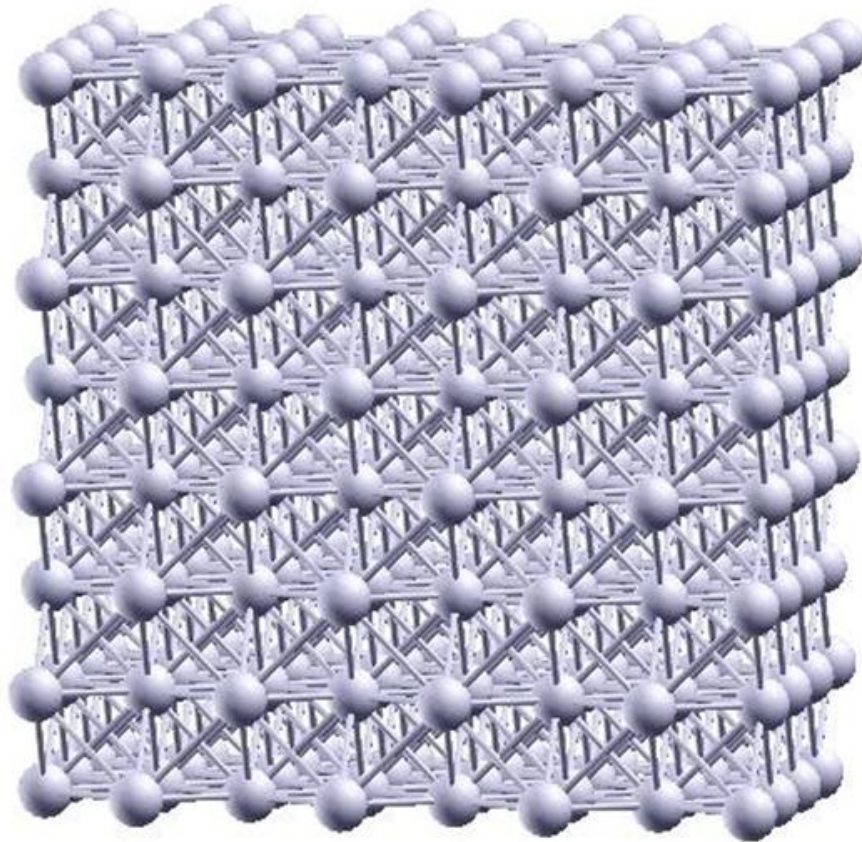


Figure 5.1-1: Forces contribution on Ag arc erosion process

Two main conclusions can be drawn from this graph. First, for this range of intensities (0, 1100A), the electromagnetic force has no impact on the contact material erosion. This can be explained by the low magnetic permeability value of Ag with respect to the considered range of intensities. Consequently, the arc erosion effects due to a change in magnetic permeability of the contact material can be neglected in comparison to the other contributions. Indeed, the material under study has no magnetic properties, and the effect of this contribution on the arc erosion process is very small. Second, as expected, the surface tension and the Buoyancy forces play important roles in the splash erosion process. So, contact material properties such as density, thermal expansion and surface tension coefficients become first order parameters in the arc erosion process.

### 5.1.2. Ab initio

*Ab initio* simulations have been run on a single phase contact material Ag matrix (See Figure 5.1-2 below) in order to determine intervals of variations of its density and its thermal expansion coefficient over the same characteristic temperature range.



**Figure 5.1-2: Supercell of FCC Ag pure compound**

#### 5.1.2.1. Description

In this work, density functional theory (DFT) [56, 57] calculations have been used to determine the evolution with temperature of the density and the thermal expansion coefficient. The Kohn-Sham equations are solved in a plane-wave basis set, using Vanderbilt ultrasoft pseudopotentials [58, 59] to describe the electron-ion interaction, as implemented in the Vienna *Ab initio* Simulation Package (VASP) [60-62]. Exchange and

correlation are described by the Local Density Approximation (LDA). We use the exchange correlation functional determined by Ceperley and Alder [63], and parameterized by Perdew and Zunger [64]. The electronic configuration of the silver atom is  $[\text{Kr}]3d^{10}4s^1$ . The kinetic energy cutoff for the plane-wave basis set is 200 eV. The convergence for energy has been chosen as  $10^{-4}$  eV between two ionic steps. In the first step, the Face Centered Cubic structure of Ag is optimized. In the calculation of the bulk properties of Ag, a (18x18x18) k-points mesh is used, which corresponds to 195 irreducible k points in the first Brillouin zone [65]. When the external pressure is zero, the lattice parameter is  $a_0=4.0227\text{\AA}$  (experimentally 4.09 Å) [66]. The error of -1.6% is correct with this approach. As a second step, a supercell is built by a (3x3x3) duplication of the conventional cell. The supercell contains 108 atoms of silver. We fix the temperature and the lattice parameter (volume is fixed). We choose 5 femtoseconds as the time step for an *ab initio* molecular dynamics and we simulate 500 steps of dynamic. The energy minimization method is the Residual Minimization Method Direct Inversion in the Iterative Subspace (RMS-DIIS). Finally, we have reduced the criterion of the energetic convergence to 0.001 eV and these calculations only use one k point (Gamma point).

#### **5.1.2.2. Methodology**

The average of external pressure on the cell is calculated. The external pressure varies around an average value. If the average of pressure is negative, the volume of the cell is too large. On the contrary, if the average of pressure is positive, the volume of the cell is too small (See Figure 5.1-3).

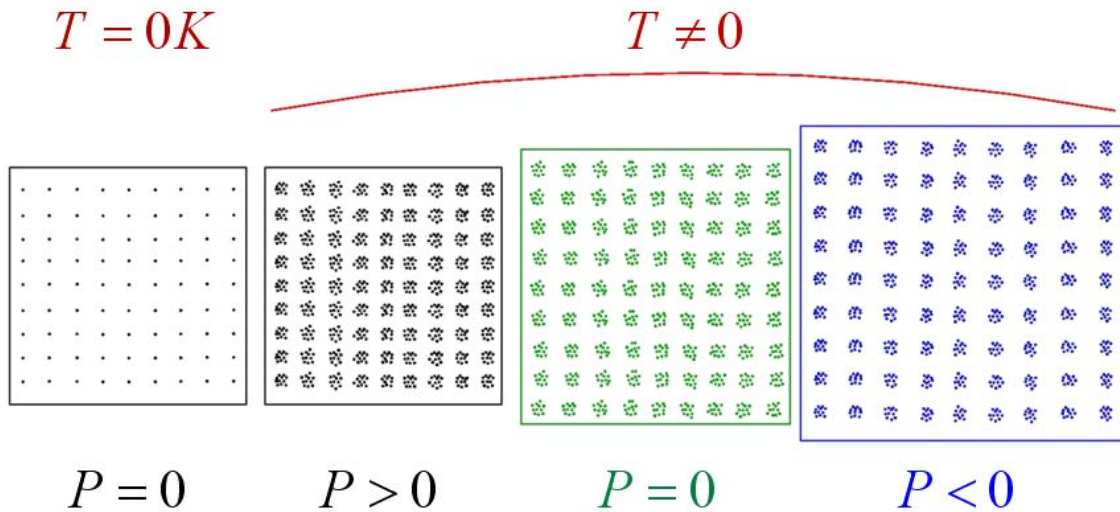


Figure 5.1-3: Pressure evolution with the lattice parameter and the temperature. The points represent the atomic positions during a few steps of the simulation

The 300 first steps are only thermalization steps, where the system goes towards the equilibrium state. The average is based on the 200 last steps.

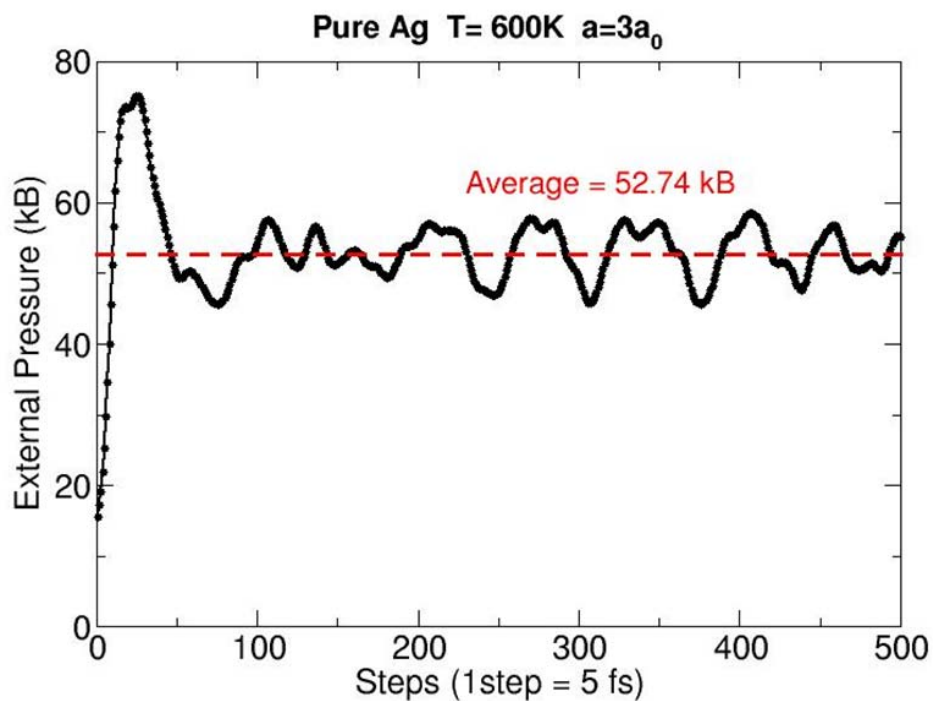


Figure 5.1-4: Variation of the external pressure with the number of dynamic steps (black line) and the average calculated with the last 200 steps (red dashed line) where the temperature is fixed and the lattice parameter is fixed

Figure 5.1-4 displays the evolution of the external pressure at 600K with the number of steps when the lattice parameter of the supercell is  $3a_0$ . We can reproduce the same calculations with different values of the lattice parameter (Figure 5.1-5).

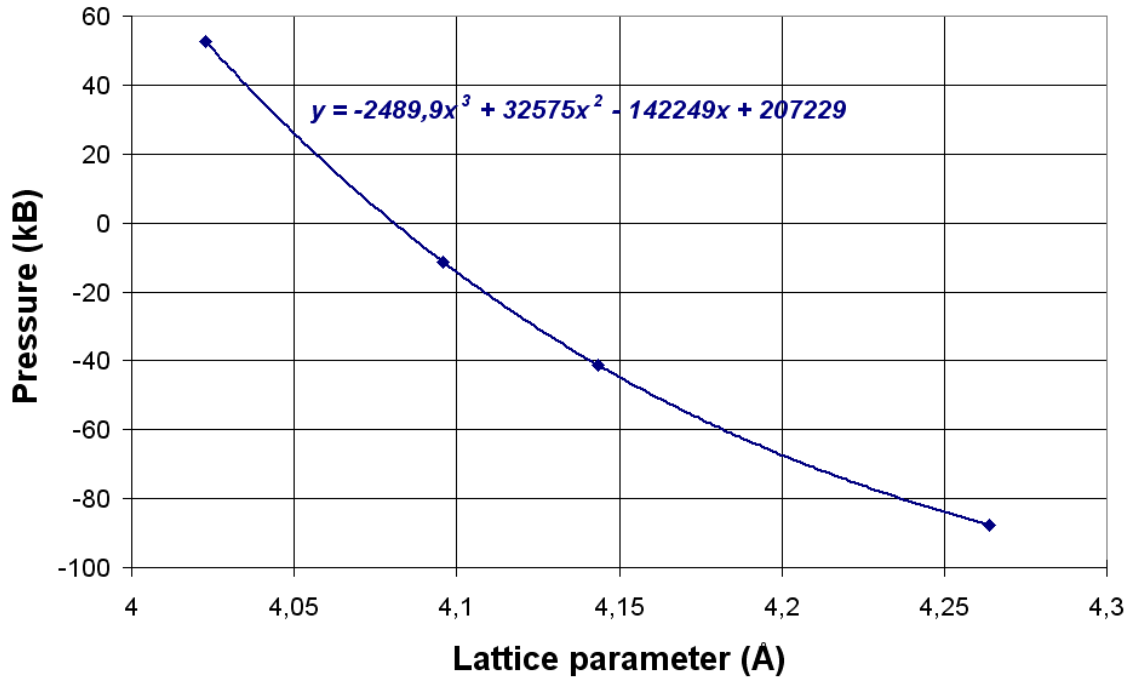


Figure 5.1-5: Variation of the pressure with the lattice parameter when the temperature is equal to 600K (points) and data fitting with a polynomial form

The lattice parameter at this considered temperature is obtained when the average of external pressure is equal to zero. When the average of external pressure is small ( $-20\text{kB} < P < 20\text{kB}$ ), a linear interpolation of these values can be performed (Figure 5.1-5). The last calculation is performed using this interpolated value in order to verify if this lattice parameter value corresponds to the equilibrium lattice parameter at the considered temperature.

### 5.1.2.3. Results

The results of these simulations are presented in Table 5.1-1. We have done a rescale of the lattice parameter because the values of the lattice parameter obtained at 0K

by the static approach and the dynamic approach are slightly different. However, the rescaled density is 1.3% lower than the not rescaled density.

**Table 5.1-1: Evolution of the lattice parameter (no rescale and rescale with the static data), the density and the thermal expansion coefficient of silver with temperature**

Temperature (K)	a (no rescale) (Å)	a (rescale / 0K static) (Å)	Thermal Expansion Coef. $\times 10^5$ (1/K)	Density (Kg/m <sup>3</sup> )
0 (static)	4.0227	-	-	-
0	4.0436	4.0227	-	11006.91
200	4.0586	4.0377	1.869	10884.42
400	4.0711	4.0502	1.709	10784.22
600	4.0832	4.0623	1.642	10687.88
800	4.0946	4.0737	1.587	10598.14
1000	4.1099	4.0890	1.650	10479.62
1200	4.1086	4.0877	1.347	10490.13

We can observe, on Figure 5.1-6 & Figure 5.1-7, the variations of the density and the thermal expansion coefficient of pure silver with temperature.

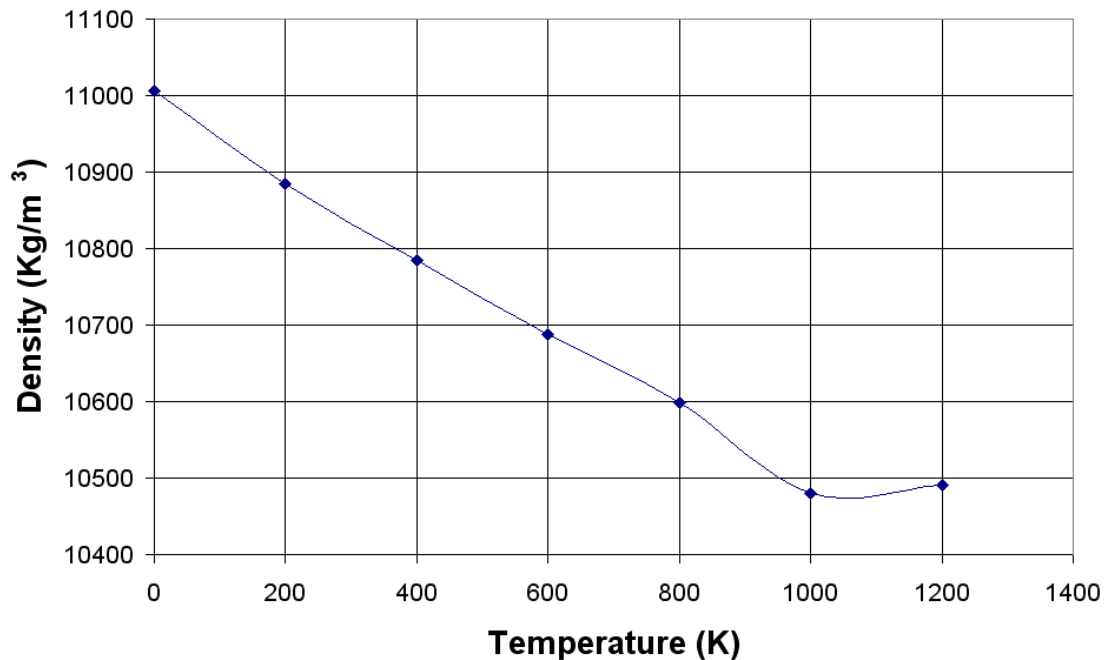


**Figure 5.1-6: Variation of the Ag density with temperature**



The Ag density keeps decreasing up to 1000 K, after which it remains constant. The minimum and maximum values are respectively  $10480$  and  $11000 \text{ kg.m}^{-3}$ .

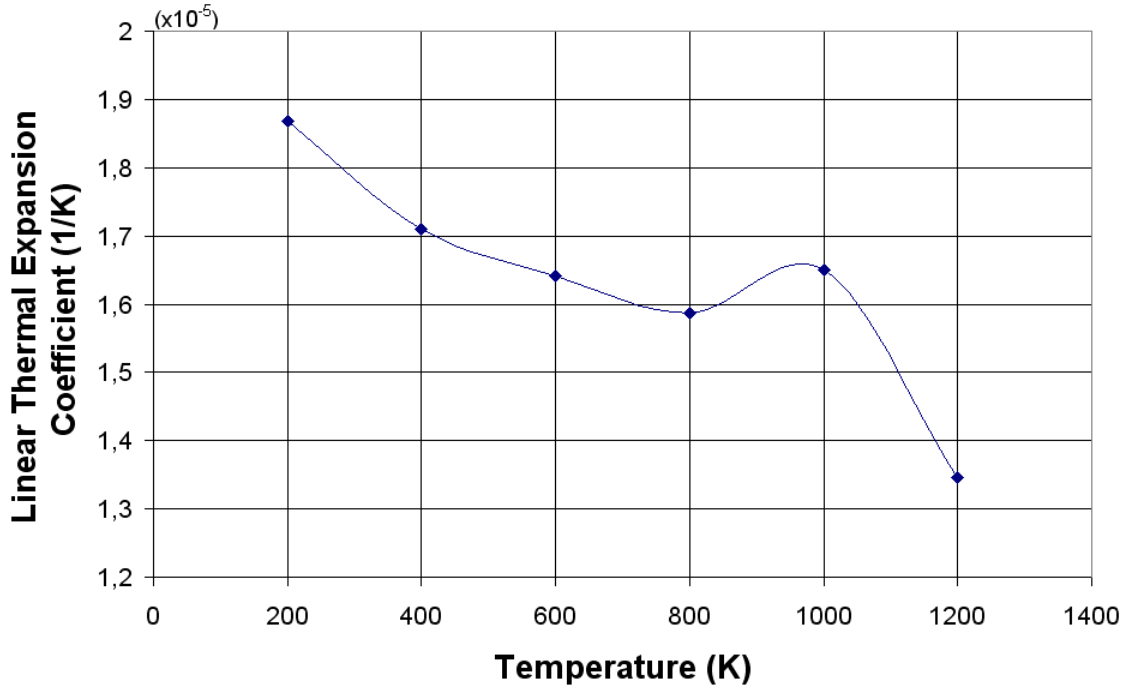


Figure 5.1-7: Variation of the Ag linear thermal expansion coefficient with temperature

The linear thermal expansion coefficient of pure silver varies between  $1.35 \cdot 10^{-5}$  to  $1.87 \cdot 10^{-5} \text{ K}^{-1}$ . It keeps decreasing with temperature up to 800 K, after which it slowly increases up to 1000 K. Then, it finally strongly decreases up to 1200 K. Experimental data are in agreement with calculated values ( $1.89 \cdot 10^{-5} \text{ K}^{-1}$  and  $10490 \text{ kg m}^{-3}$ ) [67].

We would have been able to calculate the variations of the lattice parameter with temperature by using the frozen phonon method. However, our final objective is to determine the evolution of the lattice parameter with temperature in the case of non pure compounds or non simple alloys, such as silver doped with 9% and 22% of tin oxide. And in this kind of case, calculation of the phonon curves is impossible.

### 5.1.3. Contact material properties study

Based on the former *ab initio* results, we determined the variations amplitudes over a significant interval of temperatures for Ag density and thermal expansion. We obtained the variations amplitude for Ag surface tension by using equation 5.1. Then, taking into account these different amplitudes for each of the contact material properties, arc erosion simulations have been run by using extreme values of contact material properties in order to classify them by order of importance.

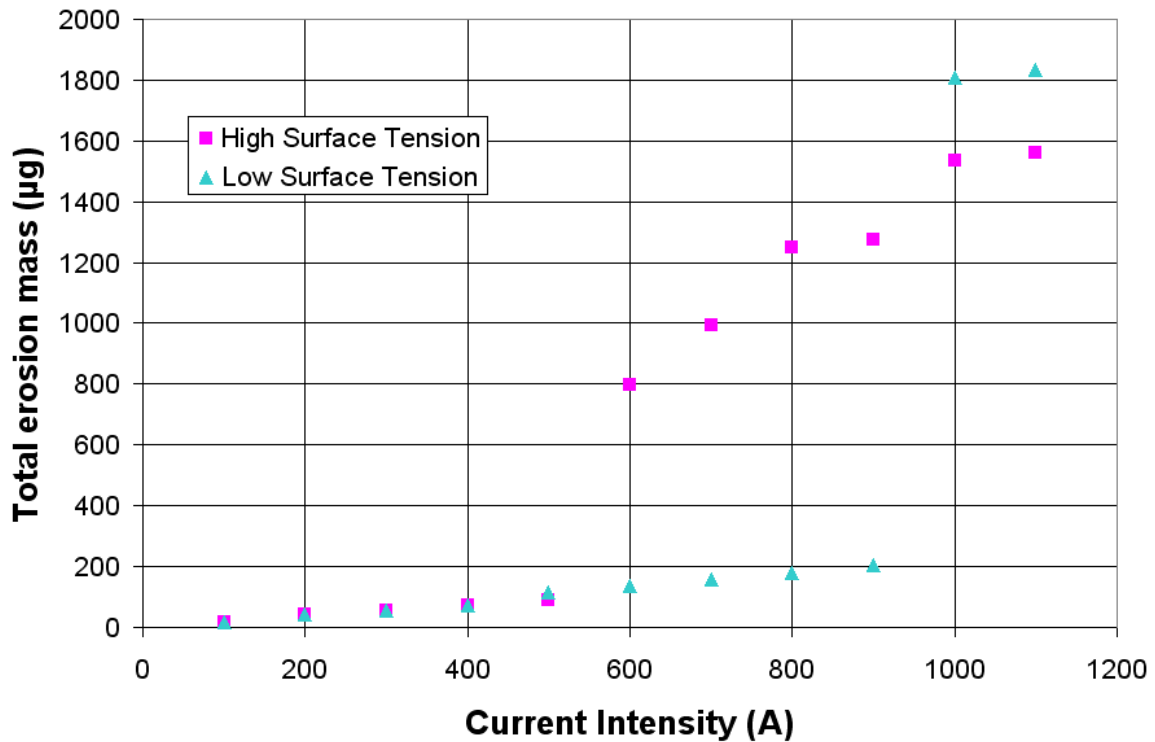


Figure 5.1-8: Arc erosion model results for a low and a high surface tension coefficient of Ag

Figure 5.1-8 shows the influence of the surface tension coefficient on arc erosion since a difference going up to 1.1 mg in the total amount of Ag material removed after one breaking operation at high current can be observed between the two cases: low & high surface tension coefficient cases.

Moreover, the jump of the low surface tension curve at 1000 A can be explained by the ejection of a molten droplet of big size through the splash erosion process.

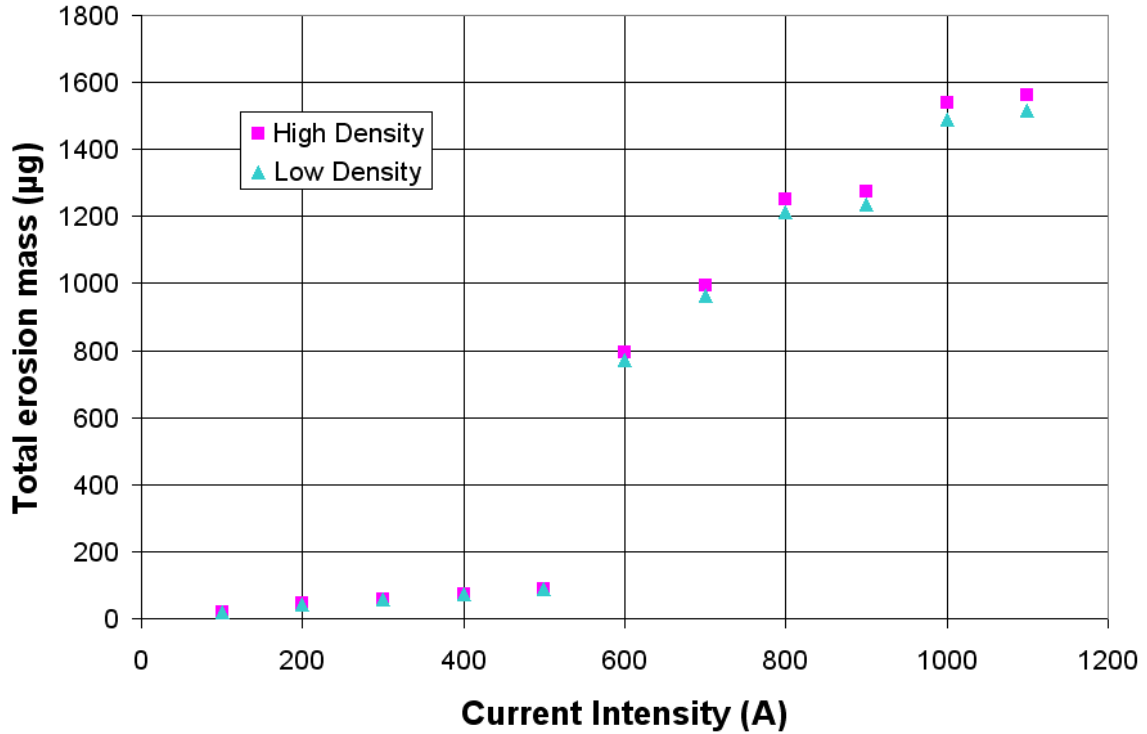
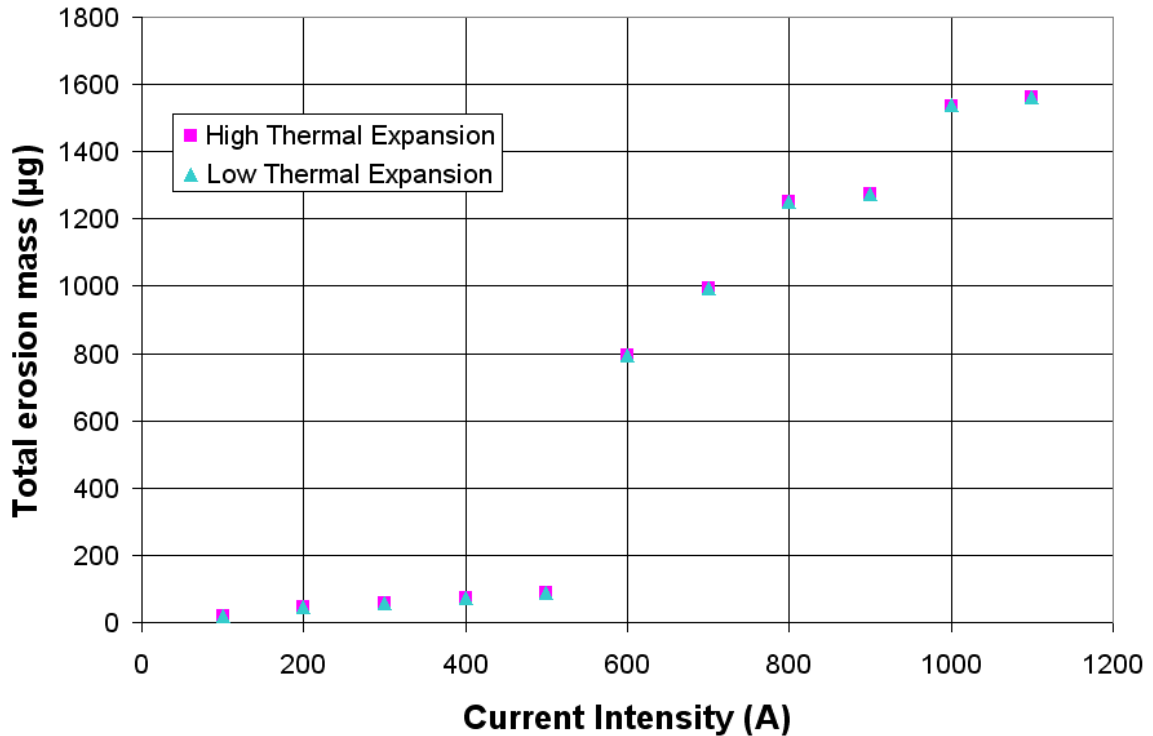


Figure 5.1-9: Arc erosion model results for a low and a high density of Ag

From the arc erosion simulations where only the silver density has been changed, only a difference going up to 50 µg at high current can be observed (See Figure 5.1-9). This value is 22 times less than the maximum difference reported in the case of a change of the surface tension coefficient.

Finally, arc erosion simulations have been conducted in which only the thermal expansion coefficient has been changed, and the results are plotted in Figure 5.1-10. Almost no differences can be noticed from these two series of points corresponding to a low and a high value of the thermal expansion coefficient.



**Figure 5.1-10: Arc erosion model results for a low and a high thermal expansion coefficient of Ag**

Differences in contact material erosion mass in between results from simulations using the maximum value of the contact material property and the results from simulations using its minimum value have been plotted on Figure 5.1-11 for the three contact material properties under study: density, thermal expansion and surface tension. The most important arc erosion mass differences can be observed, as expected, in the case of a surface tension coefficient change. The density and the thermal expansion are respectively following. Consequently, in the process of finding a good AgCdO substitute, particular attention should be drawn to the surface tension coefficient of the contact material.

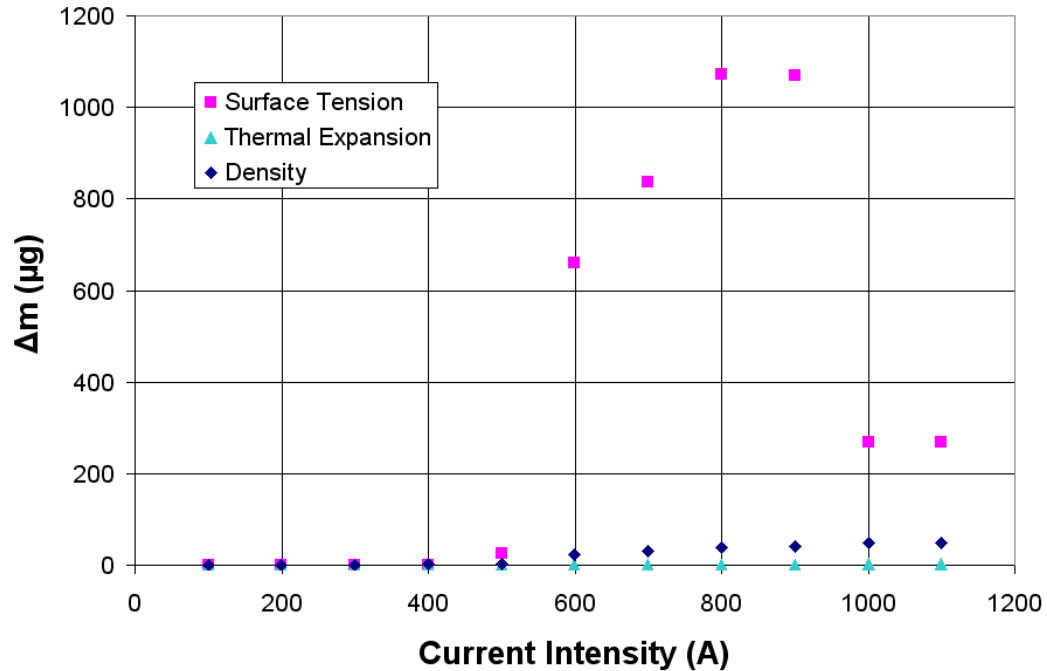


Figure 5.1-11: Contact material properties influence on Ag arc erosion process

A good choice of contact material with an appropriate surface tension coefficient can prevent some droplets from being ejected, thus reducing the amount of contact material removed by splash erosion. Density and thermal expansion do have effects and play an important role in the arc erosion process. So, they have to be considered, but subsequently.

## 5.2. Tin oxide composition influence

Chapters 2 & 3 have demonstrated the major role played by the oxides in the contact material behavior in response to arcing. From the former section, a classification has been established and gives a ranking of the contact material properties of interest as a function of their impact on the arc erosion phenomenon. Surface tension has been shown to be the most influential property. Nevertheless, *ab initio* calculations of the surface

tension coefficient as a function of the temperature for two different tin oxide compositions are beyond the scope of this study. Therefore, based on the former established classification, the second most influential property, the density, will be the object of the following work.

### 5.2.1. Methodology

*Ab initio* calculations have then been run to determine the density of  $\text{AgSnO}_2$  for two different tin oxide compositions 9 & 22 % and for three different temperatures: 800, 1000, & 1200 K. To this end, the same methodology as the one used in the former section for *ab initio* calculations on a single phase contact material silver matrix has been applied to these *ab initio* calculations on  $\text{AgSnO}_2$ .

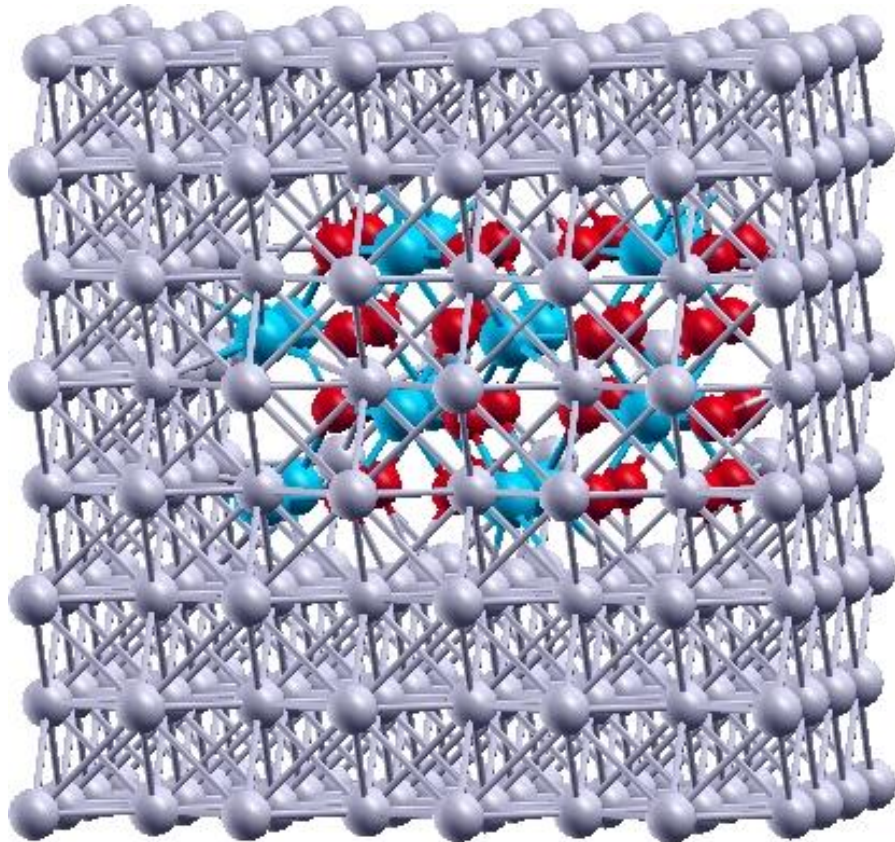
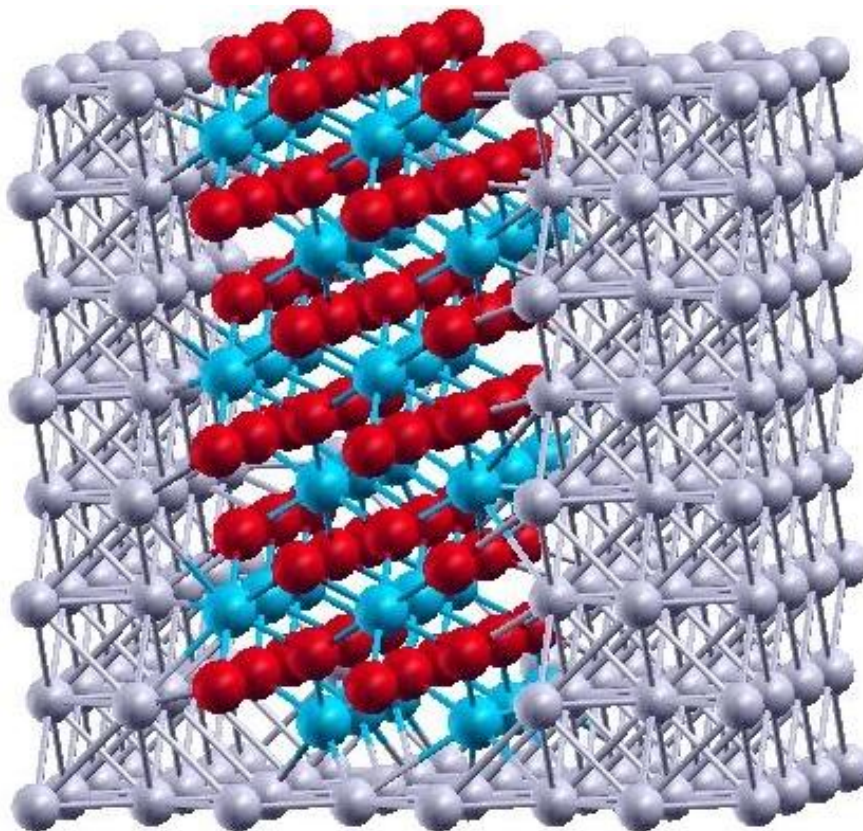


Figure 5.2-1: Schematic representation of the  $\text{AgSnO}_2$  matrix for a tin oxide composition of 9 % (267 atoms)

Figure 5.2-1 & Figure 5.2-2 respectively represent the  $\text{AgSnO}_2$  matrix of the two different tin oxide compositions tested: 9 & 22 %.



**Figure 5.2-2: Schematic representation of the  $\text{AgSnO}_2$  matrix for a tin oxide composition of 22 % (291 atoms)**

### 5.2.2. Results

Density results of the  $\text{AgSnO}_2$  *ab initio* calculations for the two different tin oxide compositions (9 & 22 %) and for three temperatures (800, 1000, & 1200 K) are plotted in Figure 5.2-3. These percentages correspond to the relative variations of the  $\text{AgSnO}_2$  density with respect to its value for pure Ag calculated in the former section.



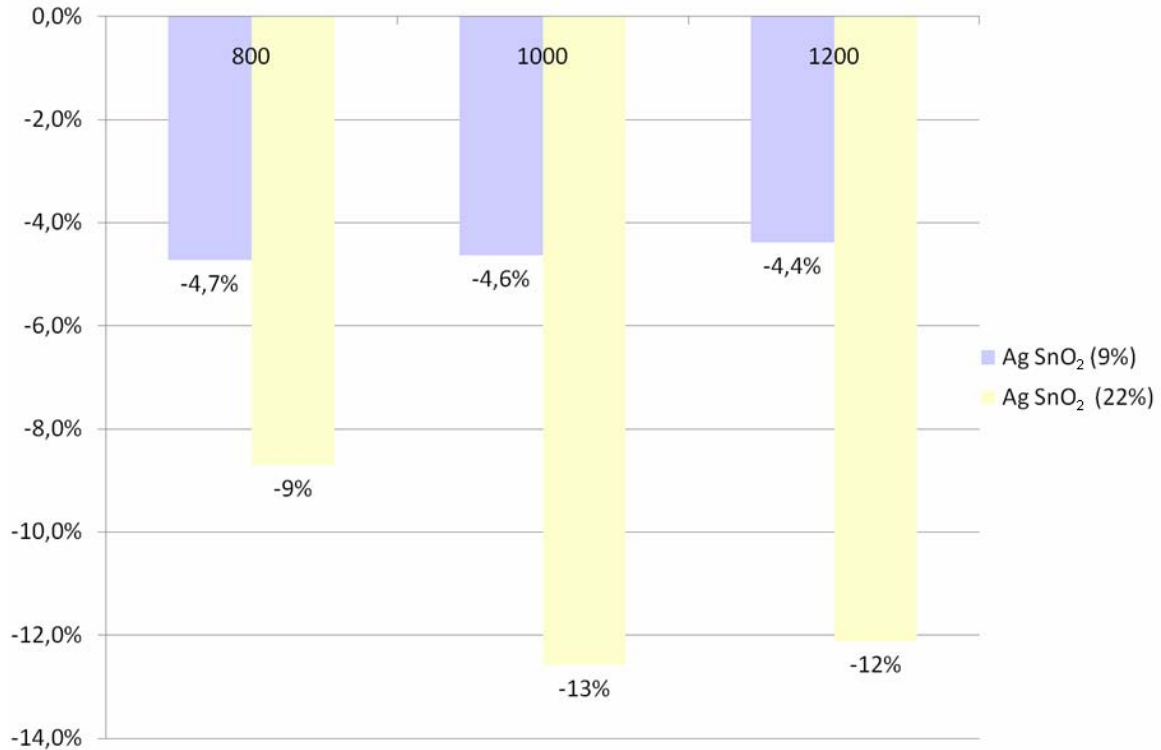


**Figure 5.2-3: Relative variations of the AgSnO<sub>2</sub> density with respect to its value for pure Ag for two different tin oxide compositions (9 & 22 %) and for three temperatures (800, 1000, & 1200 K)**

From Figure 5.2-3, it can be noticed that, as tin oxide composition of the contact material increases, the AgSnO<sub>2</sub> density decreases. However, from Figure 5.1-9 it results that, as the density of the contact material decreases, the total amount of material removed by arc erosion is reduced. Therefore, the conclusion that can be drawn is that to raise the tin oxide composition of the AgSnO<sub>2</sub> alloy reduces the amount of material removed by arcing and so enhances its arc erosion behavior.

### 5.3. Conclusion

The general validated macroscopic arc erosion model developed in Chapter 4 and *ab initio* calculations on an Ag matrix have been used to compare the influence of the contact material properties driving splash erosion on the arc erosion process. Those



simulations have resulted in the following ranking by order of their importance in the arc erosion process: Surface tension coefficient, density, thermal expansion, magnetic permeability. Thus, to select a material that will be subjected to an electrical arc, it is necessary to take into account the effects of its contact material properties on the arc erosion process, choosing therefore a material having suitable contact material property values with respect to the ranking formerly established.

Furthermore, this ranking and some  $\text{AgSnO}_2$  *ab initio* calculations for two different tin oxide compositions have allowed us to draw conclusions and to give directives for the design of a good  $\text{AgCdO}$  substitute. Indeed, to raise the tin oxide composition of the  $\text{AgSnO}_2$  alloy reduces the amount of material removed by arcing and so enhances its arc erosion behavior. However, it damages the thermal and electrical properties of the contact material since tin oxide has smaller thermal and electrical conductivities than silver. Therefore, a compromise has to be made to find out the perfect contact material composition. Moreover, it has to be kept in mind that density is only the second most influential property behind the surface tension coefficient. Thus, restraint should be taken regarding this result until future works determine the influence of the oxide composition on the surface tension coefficient and allow conclusions to be drawn.

## CHAPTER 6

### CONCLUSION

Over the past decades, a lot of scientists have been interested in the challenge lying in the substitution of AgCdO. To address this issue, a material-by-design methodology has been elaborated based on multi-scale modelling, from the atomistic scale through *ab initio* calculations to the macroscopic scale through contact material arc erosion simulations, and on arc erosions experiments on the material to substitute: AgCdO and on the best candidate material to its substitution: AgSnO<sub>2</sub>. This action plan has been defined in Chapter 1 in terms of research objectives whose achievements are detailed below.

A general electrical arc erosion model describing the complete breaking operation has been developed. This model takes into account the two arc erosion modes: vaporization of contact material under heat coming from the electrical arc and ejection of molten metal droplets due to the molten bath agitation induced by the buoyancy force, the electromagnetic force, etc. Consequently, it gives the total amount of material removed after one contact opening at low and high currents.

This model has been validated at low current through a comparison with AgCdO experimental data from literature. Moreover, arc erosion experiments at high current on five AgCdO power switching devices have been conducted in order to test the model at high current. The electrical contacts have respectively been subjected to one breaking operation under resistive load at 200, 400, 600, 800, & 1000 A. White light interferometry has been used to obtain the amount of material removed from the impacted samples. Model results have then been validated through a comparison with these experimental data. Therefore, this arc erosion model is the first one to describe the whole breaking process and to be valid at low and high current.

Other arc erosion experiments have been carried out on five AgCdO and five AgSnO<sub>2</sub> power switching devices in order to understand the arc erosion behaviours of these two contact materials. For each of these two alloys, the samples have respectively been subjected to 1, 2, 3, 10, & 100 electrical arcs under resistive load at 400 A & 28 V DC. A Scanning Electron Microscope with an Energy-Dispersive x-ray Spectrometer (EDS) and a binocular microscope with high magnification have been used to analyze the impacted samples at the contact surface and in cut.

A model based on two regimes has then been developed to describe and explain AgCdO and AgSnO<sub>2</sub> layer and surface dynamics. It consists in a transient state phase corresponding to the first few arcs where an accumulation of oxide particles can be noticed in the immediate surrounding of the contact surface, which results in an increase of the molten bath viscosity and of the contact resistance and in a decrease of the thermal and electrical conductivities. Then, with an increasing number of electrical arcs, the quasi-steady state phase occurs. It can be described as back and forth changes of the

contact material configuration around a stable configuration that causes the material properties to follow dampened oscillations around a nominal value, which corresponds to a stable configuration, from a morphological, composition, distribution and size point of view, of the contact material that the system tends to reach. Thus, this two-regimes model gives a better understanding of the specific arc erosion behaviours of AgCdO and AgSnO<sub>2</sub>.

*Ab initio* calculations and arc erosion simulations have been performed on silver in order to determine the influence of certain contact material properties on the arc erosion process. First, it has been found from arc erosion simulations, whose purpose was to study the forces contributions, that the arc erosion effects due to a change in magnetic permeability of the contact material can be neglected in comparison to the other contributions. Second, the intervals of variations of the silver density and of the thermal expansion coefficient over the same characteristic temperature range have been determined through *ab initio* calculations. Surface tension evolution as a function of temperature is known from literature. Finally, based on these results, arc erosion simulations have been run in order to determine the impact in terms of mass of removed material after arcing caused by such kind of variations. This resulted in the following classification: surface tension coefficient, density, thermal expansion, magnetic permeability. As a consequence, particular attention about this ranking will have to be taken when choosing the appropriate contact material to a power switching application

Based on this former established ranking and because the study of the surface tension variations as a function of the temperature for different tin oxide compositions is beyond the scope of this work, the influence of a change in tin oxide compositions on the

material density has been studied. To this end, *ab initio* calculations on two different tin oxide compositions of AgSnO<sub>2</sub> (91/9 & 78/22) and for three different temperatures (800, 1000, 1200 K), have been performed. The conclusion that has been drawn is that to raise the tin oxide composition of the AgSnO<sub>2</sub> alloy reduces the amount of material removed by arcing and so enhances its arc erosion behavior. However, it damages the thermal and electrical properties of the contact material since tin oxide has smaller thermal and electrical conductivities than silver. Therefore, a compromise has to be made to find out the perfect contact material composition.

To conclude, the proposed approach provides a tool to aid in the design of a good AgCdO substitute and to give directions, for instance, in terms of tin oxide composition in AgSnO<sub>2</sub>. Nevertheless, in order to go further in this process, different ways could be explored:

- One conclusion was that to raise the tin oxide composition of the AgSnO<sub>2</sub> alloy would reduce the amount of material removed by arcing and so would enhance its arc erosion behavior and, in the same time, would damage its thermal and electrical properties. Therefore, the impacts of the tin oxide composition of AgSnO<sub>2</sub> on the electrical and thermal conductivities could be examined.
- From our study, the density of the contact material is only the second most influential property behind the surface tension coefficient. Thus, in order to complete our examination, future works could determine the influence of the AgSnO<sub>2</sub> tin oxide composition on the surface tension coefficient.

- It has been demonstrated that additives, such as Indium, can play an important role in the arc erosion behaviour of the alloy. As a consequence, the influence of additives in the alloy composition on the arc erosion process could be studied.

## REFERENCES

- [1] Zhuan-Ke Chen and K. Sawa, *IEEE Transactions on components, packaging, and manufacturing technology* 21, 310-322 (1998).
- [2] P. G. Slade: 'Electrical Contacts - Principles and Applications' (Marcel Dekker, 1999)
- [3] C. Bernauer, R. Hochspannungsgeräte, V. Behrens and T. Honig, *Proceedings of the 51st IEEE Holm Conference on Electrical Contacts* (Chicago, IL: IEEE, 2005), p. 42.
- [4] O. Nilsson, F. Hauner and D. Jeannot, *Proceedings of the 50th IEEE Holm Conference on Electrical Contacts* (Seattle, WA: IEEE, 2004), p. 70.
- [5] Y. Shen, W. Cote and L. Gould, *Proceedings of the 32nd IEEE Holm Conference on Electrical Contacts*: (1986), p. 71-77.
- [6] C. Leung, E. Streicher and D. Fitzgerald, *Proceedings of the 50th IEEE Holm Conference on Electrical Contacts* (Seattle, WA: IEEE, 2004), p. 64.
- [7] J. Wang, B. Wang, M. Wen, Y. Lü, Y. Luo and Z. Li, *Proceedings of the 46th IEEE Holm Conference on Electrical Contacts* (Chicago, IL: IEEE, 2000), p. 231-234.
- [8] Volker Behrens, Thomas Honig, Andreas Kraus, Roland Michal, Karl Saeger, Rainer Schmidberger and T. Staneff., *IEEE Transactions on components, packaging, and manufacturing technology* 17, 24-31 (March 1994).
- [9] Gregory Corfar and R. Tryon.: 'Comparative study of the AgCdO, and AgSnO<sub>2</sub> contact material properties', Leach International, Buena Park, California
- [10] Philip C. Wingert and C.-H. Leung, *IEEE Transactions on components, hybrids, and manufacturing technology*, 56-62 (March 1987).
- [11] R. Michal and K. E. Saeger, *Proceedings of the 34th IEEE Holm Conference on Electrical Contacts* (San Fransisco, CA: IEEE, 1988), p. 121.
- [12] Chi H. Leung and A. Lee., *IEEE Transactions on components, hybrids, and manufacturing technology*, 146-153 (April 1992).
- [13] F. Hauner, D. Jeannot, K. McNeilly and J. Pinard, *Proceedings of the 46th IEEE Holm Conference on Electrical Contacts* (Chicago, IL: IEEE, 2000), p. 225.

- [14] J.-W. Wan, J.-G. Zhang and M.-Z. Rong, *Proceedings of the 44th IEEE Holm Conference on Electrical Contacts* (Arlington, VA: IEEE, 1998), p. 202.
- [15] D. McDonnell, *Proceedings of the 40th IEEE Holm Conference on Electrical Contacts* (Chicago, IL: IEEE, 1994), p. 253.
- [16] W. Xixiu, D. Meihua, L. Zhenbiao and L. Chengyan, *Proceedings of the 49th IEEE Holm Conference on Electrical Contacts* (Washington, DC: IEEE, 2003), p. 139.
- [17] V. Behrens, T. Honig and A. Kraus, *Proceedings of the 46th IEEE Holm Conference on Electrical Contacts* (Chicago, IL: IEEE, 2000), p. 235.
- [18] L. Xiangjun, F. Xiao and F. Hongjun, *Proceedings of the 49th IEEE Holm Conference on Electrical Contacts* (Washington, DC: IEEE, 2003), p. 145.
- [19] D. McDonnell, J. Gardener and J. Gondusky, *Proceedings of the 39th IEEE Holm Conference on Electrical Contacts* (Pittsburgh, PA: IEEE, 1993), p. 37.
- [20] Y.S. Shen and L. J. Gould, *Proceedings of the 33rd IEEE Holm Conference on Electrical Contacts* (Chicago, IL: IEEE, 1987), p. 157.
- [21] Amos Selzer, James W. Dieball and D. Litchman, *IEEE Transactions on parts, hybrids, and packaging*, 139-147 (June 1975).
- [22] E.A. Owen, J. Rodgers and J. C. Guthrie, *J. I. Met.* 65, 457 (1939).
- [23] Heloisa Cunha Furtado and V. L. A. D. Silveira, *IEEE Transactions on components, hybrids, and manufacturing technology* 11, 68-73 (March 1988).
- [24] Y. S. Shen, E. J. Zdanuk and R. H. Krock, *IEEE Transactions on parts, hybrids, and packaging*, 16-25 (1972).
- [25] Richard C. Bevington and H. J. Kim, *IEEE Transactions on components, hybrids, and manufacturing technology*, 46-51 (March 1979).
- [26] Ram Kossowsky and P. G. Slade, *IEEE Transactions on parts, hybrids, and packaging* PHP-9, 39-44 (March 1973).
- [27] P. C. Wingert and H. J. Kim, *IEEE Transactions on components, hybrids, and manufacturing technology* CHMT-8, 119-122 (March 1985).
- [28] Y.-S. Shen, *IEEE Transactions on components, hybrids, and manufacturing technology*, 81-88 (March 1983).
- [29] Philip C. Wingert and G. Horn, *IEEE Transactions on components, hybrids, and manufacturing technology*, 190-195 (March 1993).



- [30] S. A. David and T. DebRoy, *Science* 257, 497-502 (July 1992).
- [31] J. C. Vérité, T. Boucher, A. comte, C. Delalondre and O. Simonin, *IEEE Transactions on Magnetics* 31, 1843-1848 (May 1995).
- [32] T. DebRoy and S. A. David, *Reviews of Modern Physics* 67, 85-110 (January 1995).
- [33] J. Hu and H. L. Tsai, *International Journal of Heat and Mass Transfer*, 808-820 (2006).
- [34] M. Tanaka and J. J. Lowke, *Journal of Physics D: Applied Physics*, R1-R23 (2007).
- [35] H. G. Fan and R. Kovacevic, *Journal of Physics D: Applied Physics*, 2531-2544 (2004).
- [36] F. Wang, W. K. Hou, S. J. Hu, E. Kanneley-Asibu, W. W. Schultz and P. C. Wang, *Journal of Physics D: Applied Physics*, 1143-1152 (2003).
- [37] J. Hu and H. L. Tsai, *Journal of Heat Transfer* 129, 1025-1035 (August 2007).
- [38] Seungho Paik and H. D. Nguyen, *International Journal of Engineering Science* 33, 641-657 (1995).
- [39] J. Hu and H. L. Tsai, *International Journal of Heat and Mass Transfer*, 833-846 (2006).
- [40] J. Haidar and J. J. Lowke, *Journal of Physics D: Applied Physics* 29, 2951-2960 (1996).
- [41] C. J. Allum, *Journal of Physics D: Applied Physics* 18, 1431-1446 (1985).
- [42] J. Haidar, *Journal of Applied Physics* 84, 3530-3540 (1998).
- [43] Jae H. Choi, Jihye Lee and C. D. Yoo, *Journal of Physics D: Applied Physics* 34, 2658-2664 (2001).
- [44] Jonathan Swingler and J. W. McBride, *IEEE Transactions on components, packaging, and manufacturing technology* 21, 54-60 (March 1998).
- [45] M. Abbaoui, A. Lefort, D. Sallais and N. B. Jemaa, *Proceedings of the 52nd IEEE Holm Conference on Electrical Contacts*: (2006), p. 103-109.
- [46] A. Watson, A. L. Donaldson, K. Ikuta and M. Kristiansen, *IEEE Transactions on Magnetics*, 1799-1803 (November 1986).

- [47] T. G. Engel, S. L. Wester and M. Kristiansen, *IEEE Transactions on Magnetics*, 709-713 (January 1995).
- [48] A. L. Donaldson, T. G. Engel and M. Kristiansen, *IEEE Transactions on Magnetics*, 138-141 (January 1989).
- [49] Kejian Wang and Q. Wang, *IEEE Transactions on components, hybrids, and manufacturing technology*, 293-297 (June 1991).
- [50] Wu Xixiu and L. Zhenbiao, *Proceedings of the 48th IEEE Holm Conference on Electrical Contacts*: (2002), p. 29-34.
- [51] J. N. Anno: 'The Mechanics of Liquid Jets' (Lexington Books. 1977)
- [52] A. Kumar and T. DebRoy, *Journal of Applied Physics* 94, 1267-1277 (2003).
- [53] C. Weber, *Zeitschrift Für Angewandte Mathematik Und Mechanik* 11, 136 (1931).
- [54] L. Crane, S. Birch and P. D. McCormack, *British Journal of Applied Physics* 15, 743 (1964).
- [55] Joonho Lee, Wataru Shimoda and T. Tanaka, *Measurement Science and Technology* 16, 438 (2005).
- [56] P. Hohenberg and W. Kohn, *Physical Review* 136, B864 (1964).
- [57] W. Kohn and L. J. Sham, *Physical Review* 140, 1133 (1965).
- [58] D. Vanderbilt, *Physical Review B* 41, 7892 (1990).
- [59] G. Kresse and J. Hafner, *Journal of Physics: Condensed Matter* 6, 8245 (1994).
- [60] G. Kresse and J. Furthmuller, *Physical Review B* 54, 11169 (1996).
- [61] G. Kresse and J. Furthmuller, *Computational Materials Science* 6, 15 (1996).
- [62] G. Kresse and J. Hafner, *Physical Review B* 47, 558 (1993).
- [63] D. M. Ceperley and B. J. Alder, *Physical Review Letters* 45, 566 (1980).
- [64] J. P. Perdew and A. Zunger, *Physical Review B* 23, 5048 (1981).
- [65] H. J. Monkhorst and J. D. Pack, *Physical Review B* 13, 5188 (1976).
- [66] C. Kittel: 'Introduction to Solid State Physics' (Wiley. 1971)

[67] D. R. Lide: 'Chemical Rubber Company handbook of chemistry and physics' (CRC Press, 79th edn. 1998)